AD-A224 379

UMENTATION PAGE DTIC FILE COPY

Form Approved
OMB No. 0704-0188

2. REPORT DATE	3. REPORT TYPE AND DATES COVERED
April 1990	Final Report/15 Sep 88-14 Nov 89

4. TITLE AND SUBTITLE
Laser Physics and Laser Spectroscopy

5. FUNDING NUMBERS
61102F/2301/A1

(2)

6. AUTHOR(S)
Robert L. Byer

7. PERFORMING ORGANIZATION NAME(S) AND ADDRESS(ES)
Stanford University
Applied Physics Department
Stanford, CA 94305

8. PERFORMING ORGANIZATION REPORT NUMBER
AFOSR-TR- 90 0776

9. SPONSORING / MONITORING AGENCY NAME(S) AND ADDRESS(ES)
AFOSR/NP BK 410
Bolling AFB DC 20332-6448

10. SPONSORING / MONITORING AGENCY REPORT NUMBER
AFOSR-88-0354

11. SUPPLEMENTARY NOTES

12a. DISTRIBUTION / AVAILABILITY STATEMENT
Approved for public release; distribution is unlimited.

12b. DISTRIBUTION CODE

13. ABSTRACT *(Maximum 200 words)*

Two essential difficulties must be addressed in any low-power frequency conversion device; boosting the efficiency above that of simple single-pass bulk devices (which are typically less than 1%/W) and achieving phase-matching for the desired interaction. Waveguide interactions were used to increase the conversion efficiency, and explored quais-phase-matching (QPM) as a broadly applicable approach to meeting the phasematching condition. Both oxide forrelectrics like LiNbO3 and quantum-wells in III-V semiconductors have been investigated for these applications. Second harmonic generation (SHG) of near-infrared lasers to produce green and blue radiation, as well as SHG of the 9-11 micrometer output of a CO2 laser have been demonstrated in these materials. These media together constitute a significant step towards the goal of "generic" nonlinear media for the far-infrared - ultraviolet, based on readily available materials and fabricated with standard technologies, applicable to essentially any frequency conversion application.

14. SUBJECT TERMS	15. NUMBER OF PAGES
quasi-phase-matching, near-infrared lasers	84
	16. PRICE CODE

17. SECURITY CLASSIFICATION OF REPORT	18. SECURITY CLASSIFICATION OF THIS PAGE	19. SECURITY CLASSIFICATION OF ABSTRACT	20. LIMITATION OF ABSTRACT
UNCLASSIFIED	UNCLASSIFIED	UNCLASSIFIED	UL SAR

Edward L. Ginzton Laboratory
Stanford University
Stanford, California 94305

LASER PHYSICS AND LASER SPECTROSCOPY

Final Technical Report

for

Air Force Office of Scientific Research

Contract number: F49620-88-0354

for the period

September 15, 1988 to November 14, 1989

GL Report No. _____

Principal Investigator:

Robert L. Byer

Applied Physics Department
Stanford University
(415) 723-0226

April, 1990

LASER PHYSICS AND LASER SPECTROSCOPY

Final Technical Report
April 1990

TABLE OF CONTENTS

LASER PHYSICS AND LASER SPECTROSCOPY

Final Technical Report
April 1990

I. INTRODUCTION AND OBJECTIVES

The goal of this project was the demonstration of improved media for guided-wave and nonlinear optical devices. The general approach taken was to "tailor" readily available media to suit particular applications, rather than to attempt the development of entirely new material systems. This project evolved from a previous program in single-crystal optical fibers supported by the AFOSR, so the work reported here includes both completion of projects begun under this previous program, as well as results of new directions pursued after its completion.

The major effort in the present program has been the development of media suited to frequency conversion of moderate-power (<100 mW) near-infrared diode-lasers and diode-laser-pumped solid-state lasers. Such efficient solid-state sources of coherent optical radiation could be applied to a number of technologically important problems. For example, high storage density optical memories and high resolution xerographic processes would be possible if a blue light source were found to replace bulky, inefficient argon-ion and He-Cd lasers. Coherent room-temperature mid-infrared sources would be invaluable for a variety of sensors, and for the detection of industrial emissions or chemical agents. It has proven difficult to develop diode lasers in these spectral regions, so conversion of the outputs of available near-infrared diode lasers to other wavelengths is an attractive approach.

Two essential difficulties must be addressed in any low-power frequency conversion device: boosting the efficiency above that of simple single-pass bulk devices (which are typically less than 1%/W) and achieving phase-matching for the desired interaction. We have used waveguide interactions to increase the conversion efficiency, and explored quais-phase-matching (QPM) as a broadly applicable approach to meeting the phasematching condition. Both oxide ferroelectrics like $LiNbO_3$ and quantum-wells in III-V semiconductors have been investigated for these applications. Second harmonic generation (SHG) of near-infrared lasers to produce green and blue radiation, as well as SHG of the 9 – 11 μm output of a CO_2 laser have been demonstrated in these materials.

These media together constitute a significant step towards the goal of "generic" nonlinear media for the far-infrared – ultraviolet, based on readily available materials and fabricated with standard technologies, applicable to essentially any frequency conversion application.

We have also carried out several other studies under the support of this program: single-crystal sapphire fibers for energy delivery and sensor applications, techniques for composition control of lithium niobate through vapor-phase transport, and polysilane thin films for waveguide applications. The sapphire fibers have high melting points (2040°C), broad transparency ranges (beyond 3 μm in the IR), good mechanical properties, and losses below 1 dB/m for $\lambda > 0.6$ μm, making them excellent candidates for medical applications with IR lasers, e.g. surgery with 2.9 μm Er:YAG lasers. The vapor-phase-transport (VTE) lithium niobate has excellent homogeneity and large, controllable birefringence useful for adjusting phase-matching wavelengths in nonlinear devices. The polysilane films, originally developed as photoresists for UV lithography, are readily spun on a variety of substrates as waveguide-quality films, have large third-order nonlinear susceptibilities, and can be optically patterned to produce birefringent waveguide structures.

II. SUMMARY OF MAJOR ACCOMPLISHMENTS

This research program involves work at the interface between materials and device technology for guided wave and nonlinear optics. The accomplishments summarized here span a wide range of topics, and are discussed in more detail in subsequent sections of this report.

1. Quasi-phase-matched second harmonic generation in lithium niobate waveguides

A technique based on in-diffusion of lithographically patterned Ti films into lithium niobate substrates was developed to induce periodic reversal of the ferroelectric domain orientation with periods as short as 4 μm. The associated periodic reversal in the sign of the nonlinear susceptibility allowed quasi-phase-matching (QPM, compensation of the phase velocity mismatch) of second harmonic generation of blue and green light in planar and channel waveguides fabricated in the periodically-poled substrates. This process eliminates the need for birefringence to phasematch, allowing the use of the large d_{33} nonlinear coefficient (14 times the efficiency of d_{15}) for any interaction within the transparency range of lithium niobate. The waveguide geometry provides an efficiency enhancement of 2 – 3 orders of magnitude over bulk interactions.

2. Growth of periodically-poled fibers and rods of lithium niobate

Our laser-heated pedestal growth apparatus was adapted to grow crystals with volume gratings of periodically reversed ferroelectric domains. Periodic modulation of the growth rate through amplitude modulation of the heating laser was used to induce periodic striations in the composition of the crystal. These striations lead to domain reversals with periods as short as 2 μm on cooling through the Curie temperature. These structures can be used for first order QPM any interaction within the transparency range of lithium niobate. SHG of blue light at 408 nm was demonstrated in these crystals, with approximately 250 domains contributing coherently to the interaction.

3. Observation of extremely large nonlinear susceptibility due to intersubband transitions in AlGaAs quantum wells

Transitions between subbands within the conduction band of III-V quantum wells have large oscillator strengths and characteristic energies in the mid- and far-infrared. The second order nonlinear susceptibilities in these structures, increased by the large oscillator

strengths and by resonant enhancements, can be extremely large if the inversion symmetry of the wells is broken. We have measured the wavelength and bias field dependence of the nonlinear susceptibility of wells in which the symmetry is broken by an applied electric field, for wavelengths between 9.6 μm and 10.8 μm and fields up to 36 kV/cm. The peak susceptibility, 28 nm/V, is 70 times larger than that of bulk GaAs, is among the largest measured in any medium, and agrees well with a model incorporating nonparabolicity, band bending and resonant screening effects.

4. Tissue ablation with 2.9 μm radiation delivered through a single-crystal sapphire fiber

The growth of optical quality single-crystal sapphire fibers has been an ongoing component of our research program. The properties of these fibers, including a broad transparency range (out to 4 μm in the infrared), high melting point (2050°C), mechanical strength and low toxicity make them attractive for delivery of IR lasers in surgical applications. We have grown 110 μm fibers in lengths up to 2.5 m, and characterized their absorption and scatter losses. At 2.9 μm the total loss is ≈ 1 dB/m, low enough for practical applications. We demonstrated the suitability of these fibers for laser surgery by in vitro ablation of post-mortem human arterial tissue with 6 mJ, 110 μs pulses of 2.9 μm radiation, 20 times lower energy than the observed damage threshold of the fibers.

5. Demonstration of optically written birefringence in polysilane thin films

We have been studying the linear and nonlinear spectroscopy of thin polysilane films to ascertain their suitability for waveguide applications. An important outcome of the studies is the observation that two-photon absorption induces a permanent birefringence in the films, of magnitude $\Delta n \approx 0.03$, with principal axes determined by the polarization of the pump field. This high degree of 'memory' of the polarization state of photoexposure has many potential applications, including the formation of birefringent gratings and variable waveplates through photoexposure, as well as the patterning of integrated optical devices or encoding of digital information. We have characterized such birefringent diffraction gratings fabricated by pulsed laser holography, and have observed grating efficiencies as high as 8%, with a polarization diffraction ratio greater than 10:1. Calculated estimates of the related two-photon enhancement of n_2, useful for nonlinear switching devices, show that polysilanes should be comparable to the more commonly studied polydiacetylenes.

III. PROGRESS AND ACCOMPLISHMENTS

A. Quasi-Phase-Matched Interactions

A.1. Introduction

The fundamental materials problem (and hence the fundamental problem) in low power frequency conversion devices is to obtain a medium with adequate nonlinearity and transparency that can be phasematched for interactions of interest. The latter constraint, phasematching, is generally satisfied by using the birefringence of the crystal to offset the dispersion. In practice, it is often difficult to obtain such a fortuitous combination of material parameters, particularly at short wavelengths, which leads to the use of materials like $KNbO_3$ that would otherwise be rejected because of other unattractive properties.

Our work has focussed on a more general technique, quasi-phasematching (QPM), which allows effective phasematching over the entire transparency range of a crystal. In a quasi-phasematched interaction, the fundamental and second harmonic waves have different phase velocities, but the sign of the nonlinear susceptibility is changed every time the waves drift out of phase by π, i.e. every coherence length, as seen in figure 1. The modulation of the nonlinear susceptibility resets the relative phase of the driving polarization and the generated second harmonic, so that the second harmonic power grows monotonically with interaction length, instead of oscillating as in a non-phase-matched interaction.

While the conceptually simplest approach to QPM, slicing the crystal into wafers one coherence length thick and rotating every other wafer by 180°, has been demonstrated for far-infrared interactions, it is impractical for visible interactions with coherence lengths of several microns. As an alternative, we have periodically reversed the orientation of ferroelectric domains (periodically-poled) in lithium niobate and lithium tantalate. The orientation of the polar crystal axes is inverted in antiparallel domains, so that such a periodically-poled crystal has the periodic sign change in the nonlinear susceptibility necessary for QPM.

Quasi-phasematched interactions in lithium niobate are of interest for several reasons. With an appropriate structure, one can quasi-phasematch any nonlinear interaction over the transparency range of the material. One is thus no longer constrained by the necessity of finding an appropriate combination of birefringence and dispersion to

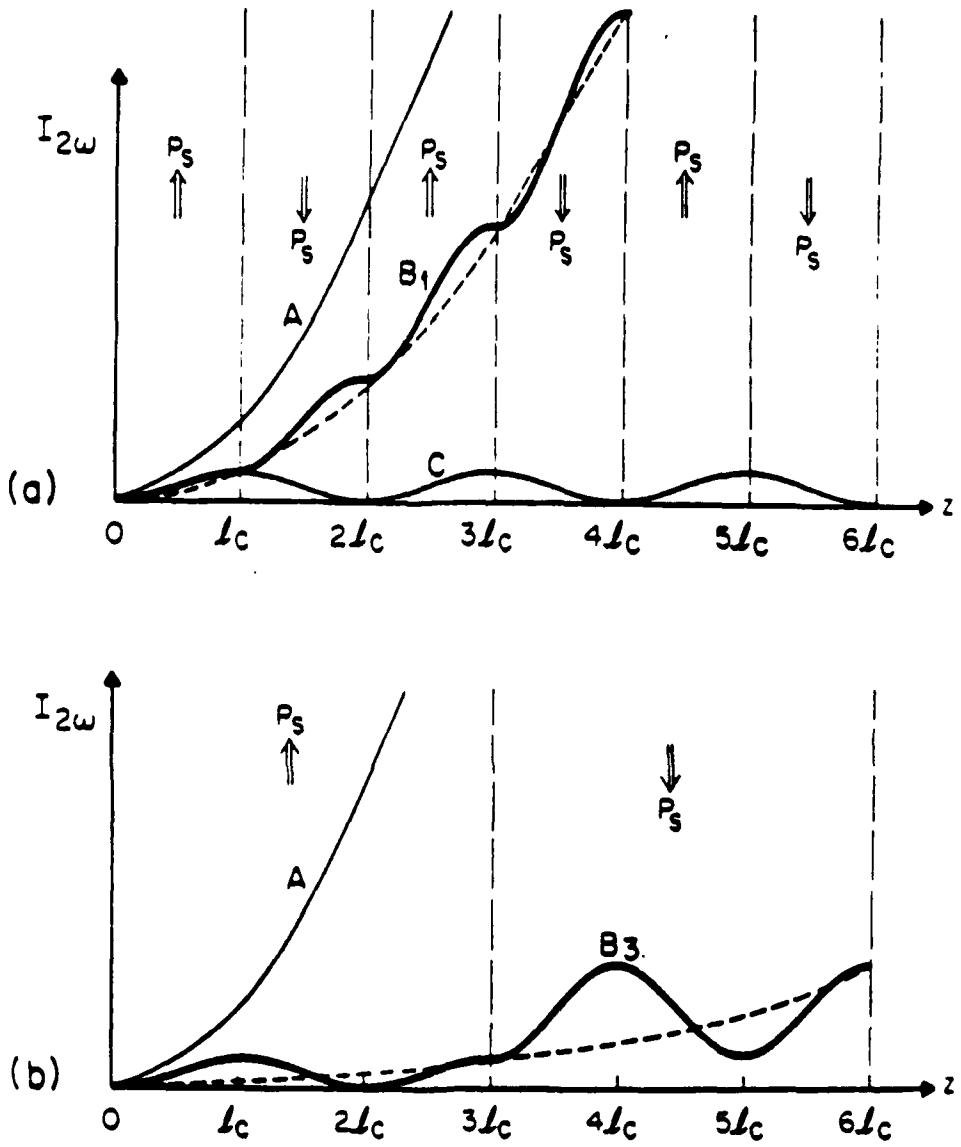

Figure 1: Effect of phasematching on the growth of second harmonic intensity with distance in a nonlinear crystal.

(a) Curve A: perfect phasematching in a uniformly poled crystal. Curve C: non-phasematched interaction. Curve B_1: first-order quasi-phasematching by flipping the sign of the spontaneous polarization every coherence length of the interaction curve C.

(b) Curve A: perfect phasematching Curve B_3: third-order quasi-phasematching by flipping P_S every three coherence lengths

phasematch a particular interaction. Since there is no longer any reliance on birefringence for phasematching, it is possible to polarize all the interacting waves along the c-axis, so that the relevant nonlinear coefficient is d_{33}. This coefficient is larger than the d_{15} coefficient used in birefringently phasematched interactions, leading to an 14 fold increase in the efficiency of the nonlinear interaction for a given length of material. One thus has access to interactions not birefringently phasematchable, can shift the phasematching temperature of phasematchable interactions to a more convenient operating point, and can take advantage of a significantly larger nonlinear susceptibility.

For typical visible light interactions, demonstration of QPM then requires the fabrication of ferroelectric crystals with domain reversals every 1.5 – 10 μm which retain the high optical quality of uniformly poled crystals. We have demonstrated two general approaches to fabricating such crystals. In one the domain reversals are induced by periodically perturbing the growth of fibers and small rods of lithium niobate. The other, a planar process, involves lithographic patterning of a dopant on a substrate, a heat treatment to drive in the dopant and create the domains, and finally a second lithographic step to define a channel waveguide by an ion-exchange process. Both techniques have successfully been applied to the generation of blue and green light by SHG of 800 – 1060 nm fundamental wavelengths in nonresonant, single-pass devices.

A.2. Modelling Lithium Niobate Devices

The analysis of ideal quasi-phase-matched structures is identical to that of conventionally phase-matched devices, with the exception that for mth order QPM (domain thickness equal to $m\, l_c$) the nonlinear coefficient is replaced by $d_Q = (2/m\pi)\, d_{eff}$. For interactions involving extraordinary polarized light in lithium niobate, $d_{eff} = d_{33} = 35$ pm/V, so that $d_Q = 22$ pm/V. The efficiency of confocally focused bulk interactions scales with the length of the crystal and with the input power, so it is convenient to define a normalized efficiency η, with units [%/W-cm], according to $P_{2\omega}/P_\omega = \eta\, L\, P_\omega$. One then predicts a conversion efficiency for bulk QPM doubling of an 800 nm pump of 13 %/W-cm, 14 times larger than that of birefringently phasematched lithium niobate, if it were possible to phase-match at this wavelength. Thus, in a 1 cm long bulk nonresonant device, one expects 1.3 mW of 400 nm output for 100 mW of input power.

In a waveguide, the conversion efficiency is increased by the elimination of diffraction effects. The efficiency then scales with the square of the length of the device

and with the input power so that the normalized efficiency has units [%/W-cm^2] and is defined by $P_{2\omega}/P_{\omega} = \eta L^2 P_{\omega}$. The normalized efficiency is inversely proportional to the effective area of the interacting waveguide modes, which is calculated from an overlap integral of the modes involved in the interaction, as discussed in the appended article from *Proc. SPIE.* by Fejer, Magel, and Lim.[1] For an effective area of 10 μm^2 (approximately the case for 3 μm spot size modes), the conversion efficiency for first order QPM SHG of 400 nm radiation is 3.5% /mW-cm^2, so that a 10 mW input would generate 3.5 mW of 400 nm light in a 1 cm long device, while 100 mW of input power would produce this same output in a 1 mm long device. It is easier to fabricate lower frequency gratings, so one often uses third order interactions, for which the theoretical conversion efficiency is 1/9 that of the first order device, or 0.4%/mW-cm^2.

The temperature and wavelength acceptance bandwidths of these devices are important practical considerations. Unlike the bandwidths for birefringent phasematching, which depend on the temperature or wavelength derivatives of the birefringence, the bandwidths for QPM depend on the dispersion of these quantities for the extraordinary index alone, i.e. if dn_e/dT were independent of wavelength, the temperature acceptance would be infinite. In the infrared, where these dispersions vary slowly with wavelength, the acceptances are in fact quite large, as much as 700°C-mm for SHG of 1.06 μm. As one tunes towards shorter wavelengths, the temperature acceptance becomes smaller as the wavelength dependence of the derivatives becomes larger. In the green, the temperature acceptance is 30°C-mm, and for 430 nm radiation, it is 15°C-mm. The wavelength acceptance for 430 nm generation is 7 Å-mm. Noting that diode lasers typically tune 2 – 4 Å/°C, we see from these bandwidths that the limitation of the diode/doubler system is the combination of the temperature tuning of the diode and the wavelength acceptance of the QPM doubler.

A.3. Planar Lithium Niobate Devices

We have studied both planar and channel devices in lithium niobate wafers. By patterning a thin (50 Å) Ti film with a straightforward liftoff process, gratings with 4 to 25 μm periods have been created on z-cut lithium niobate substrates. With suitable heat treatment, the Ti is diffused into the substrate, which, on cooling to room temperature, leads to an array of periodically reversed ferroelectric domains with a spatial period identical to that of the grating, as shown in figure 2. Waveguide fabrication is done with a low temperature proton exchange in benzoic acid, followed by a 350 °C annealing step.

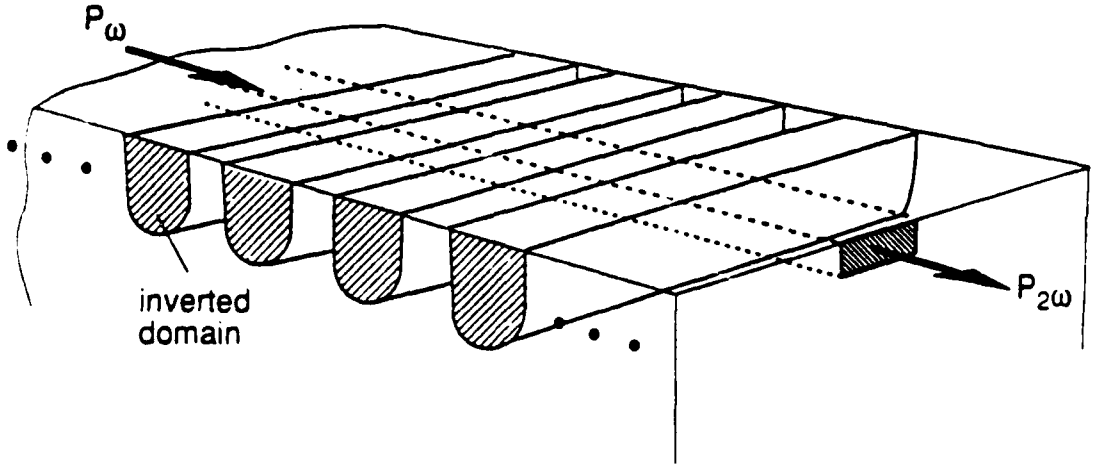

Figure 2: Section of a typical channel waveguide device, with periodically reversed ferroelectric domains at the surface, traversed by an ion-exchanged channel waveguide.

The resulting waveguides are single mode at the fundamental wavelength, and retain the domain distribution previously induced in the substrate. With an additional masking step before the proton exchange, it is possible to fabricate channel guides.

We have studied the generation of both 532 nm and 410 nm radiation in these waveguides. With prism input coupling of Nd:YAG or Styryl-9 dye lasers into planar waveguides, conversion efficiencies in 1 mm long gratings were ≈ 5%/W-cm^2. In channel guides, single-pass conversion as large as 40%/W-cm^2 has been observed for 820 nm fundamental wavelengths. This conversion efficiency is substantially smaller than the 350 %/W-cm^2 one predicts from the observed mode sizes, which were 3.7 μm and 3.1 μm for in-plane and out of plane at the fundamental, and 2.1 and 1.5 μm in the blue. The possible sources of the discrepancy will be discussed in the section A.6. The effective length of these devices, as calculated from the width of the wavelength tuning curve, was ≈0.9 mm, in good agreement with the actual 1 mm length of the grating, as shown in figure 3. We then attempted to scale these devices to 1 cm lengths, retaining the same fabrication steps, but changing the mask used to pattern the titanium that induces the domain

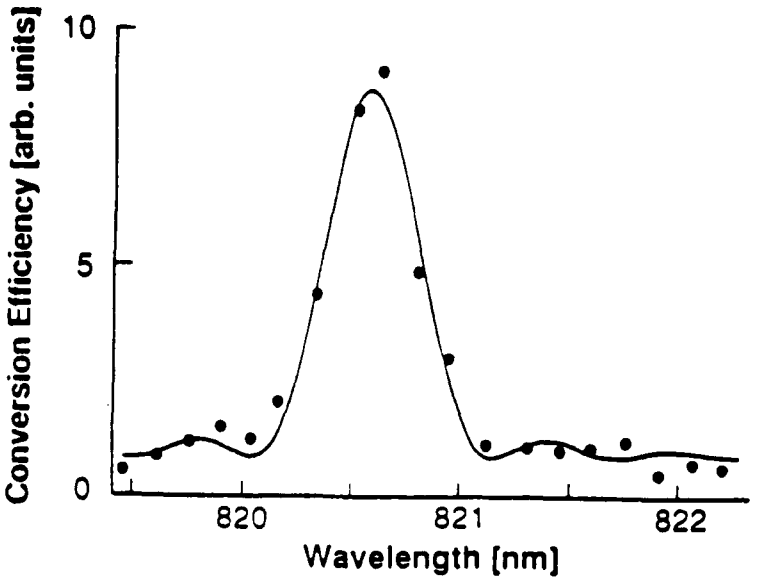

Figure 3: Wavelength tuning curve for second harmonic generation of 410 nm from an 820 nm pump in a 1 mm long periodically poled waveguide device. The $sinc^2$ dependence and the linewidth agree with theoretical predictions.

formation. Our first 1 cm long devices had effective lengths of only 1 mm, indicating serious problems with the homogeneity of the waveguides. The source of these inhomogeneities was identified to be temperature gradients in the benzoic acid bath. With a better stirred melt, our next generation of devices had an effective length of 3 mm, and produced 30 μW of 410 nm radiation for 25 mW input. The normalized conversion efficiency was therefore similar to that of the 1 mm devices, if the 10 mm actual length is replaced by the 3 mm effective length in the calculation. Recently we have generated as much as 130 μW of 410 nm radiation in similar devices, with no apparent photorefractive effects.

While these results demonstrate the possibility of QPM devices in the blue, construction of a practical device requires an understanding of the phenomena that limit the efficiency, particularly tolerances for inhomogeneities in the domain spacings and waveguide structures, and power handling capability of the material. These issues are discussed in section A.6.

A.4. Fiber/Rod Lithium Niobate

The growth of fibers and small rods of oxide crystals using a laser-heated pedestal-growth apparatus, shown in figure 4, has been an ongoing component of this program. One of the materials grown with high optical quality in these studies has been lithium niobate. We have succeeded in extending this work to the growth of crystals containing volume gratings of reversed domains by appropriate modulation of parameters during growth. For example, periodic modulation of the heat input to the molten zone leads to the creation of domains whose spacing is given by the ratio of the pull rate to the modulation frequency. In work with the laser-heated pedestal growth apparatus in our laboratory, periodic domains as small as 1 μm in size have been obtained.

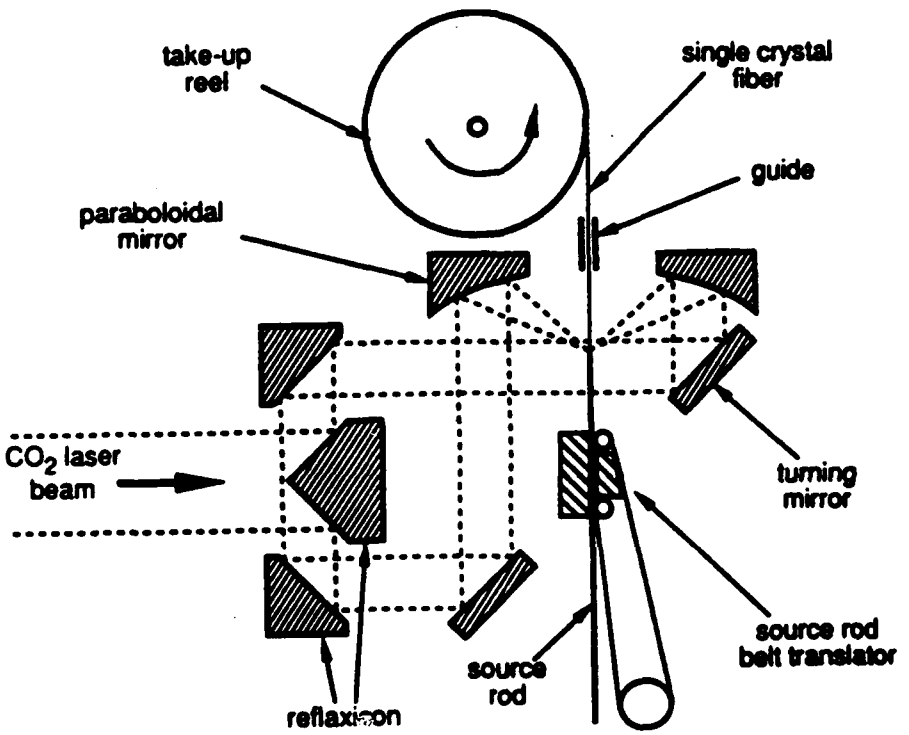

Figure 4: Cross sectional diagram of focussing optics and translators used to grow single-crystal fibers.

The original goal of this program was to produce fibers adequate for use as single mode waveguides for birefringently phasematched interactions at higher powers than are readily supported in conventional channel waveguides. As periodic poling technology advanced, this goal became less urgent, as the all-extraordinary polarization of the modes in QPM interactions allows the use of planar waveguides, discussed in section A.3, which are relatively damage resistant but support only the extraordinary polarization. In addition, periodically-poled crystals seem inherently to have dramatically higher resistance to photorefractive damage than do uniformly poled crystals. Hence the focus of the fiber growth project has shifted to the production of "bulk" (≈ 1 mm diameter) crystals, suitable for use with hundreds of milliwatts of visible power in microlaser applications.

A description of the techniques used to create periodic domains and the optical characteristics of several fibers used for blue light generation are given in a recently completed dissertation.[2] These measurements are summarized in the *Proc. SPIE* [1] article and the *Appl. Phys. Lett.*[3] appended to this document. The periodic domains are created by modulation of the power in the CO_2 laser beam used as the heat source in the pedestal growth apparatus. The consequent modulation of the growth rate leads to compositional striations (either in the Li/Nb ratio in undoped crystals or in the Mg/Nb ratio in Mg doped crystals) which lead, through mechanisms still under investigation, to domain reversals. The steep temperature gradients and rapid growth rate characteristic of the pedestal growth process result in a very short dwell time above the Curie temperature for the crystal, which in turn reduces the tendency of the striations to blur through diffusion.

Periodically-poled crystals of both *a*- and *c*-axis orientations have been grown by this technique, with domains as small as 1 μm, adequate for first order QPM of essentially any interaction in the transparency range of lithium niobate. The SHG curve for fundamental wavelengths of 800 – 900 nm have been made for both extraordinary and ordinary polarizations, and are shown in figure 5. Measurements of the width of the SHG curve show that the effective length is typically 300 μm, nearly long enough for device applications when the 14 fold increase in efficiency per unit length, discussed in section A.1, is taken into consideration. That the effective length is the same for both polarizations strongly suggests that the problem is with the periodicity of the domain spacing rather than with the homogeneity of the crystal, since the former affects both polarizations similarly, while the latter generally have much stronger effect on the extraordinary polarization.

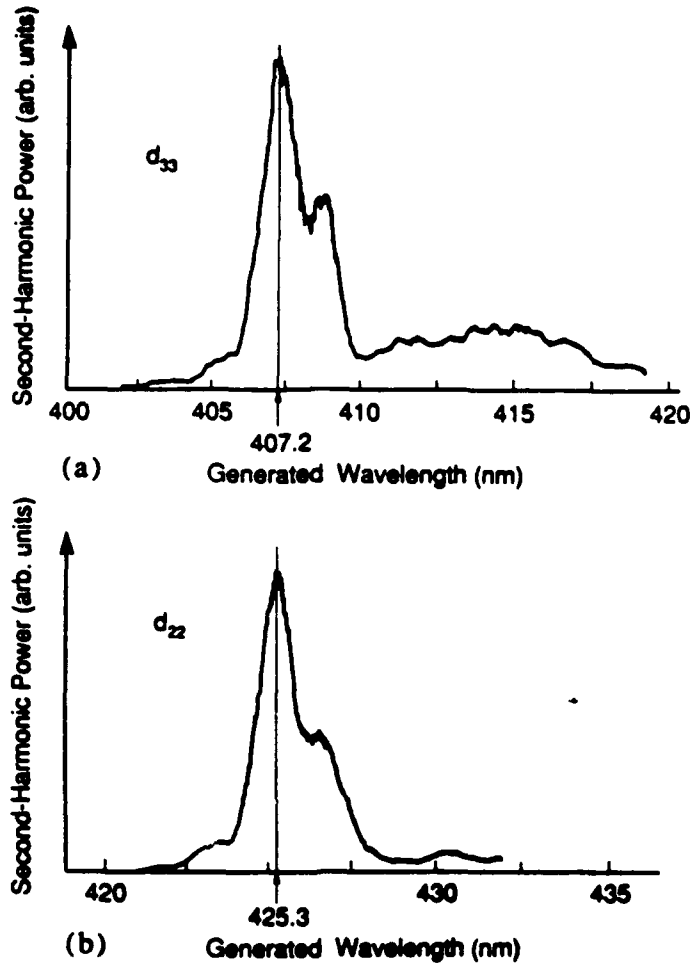

Figure 5: Second harmonic power as a function of fundamental wavelength for ordinary and extraordinary polarized radiation in periodically poled lithium niobate rod.

Another important result of the work in the bulk crystals is the observation that the resistance to photorefractive damage of periodically poled crystals is dramatically higher than that of uniformly poled crystals. 100 mW of 488 nm radiation focussed to a 10 μm spot through a 1 mm long periodically-poled crystal did not cause any measurable beam blooming, while microwatts led to visible blooming in uniformly poled crystals. This result can be understood qualitatively from the periodic sign change in the electro-optic coefficient, and hence in the direction of photorefractive beam coupling, on a very fine spatial scale in the periodically-poled crystal.

A.5. Planar Lithium Tantalate

We have also explored the possibility of periodically poling lithium tantalate. This crystal is of interest for its superior resistance to photorefractive damage (by two orders of magnitude) and its lower Curie temperature (≈600°C), which allows direct electric field poling of the crystals. We have poled the crystals by fabricating interdigital electrodes on a *z*-cut wafer and applying a constant current source across the electrodes while cooling the crystal through its Curie temperature. Under proper conditions, domains align with the poling fields, yielding well defined boundaries for the reversed regions. The electrodes are then stripped from the substrate, and a waveguide fabricated using proton exchange through a tantalum mask.

The major process development step was the identification of conditions under which sufficient current to produce well-defined domains could be passed through the crystal without damaging the surface under the electrodes. We found that standard Cr:Au electrodes were not appropriate, as the Cr had a strong tendency to electrodiffuse through the crystal. We had much better results with Ti:Au electrodes, and low current densities applied for a short interval just as the crystal passed through the Curie temperature.

With these techniques we fabricated our first device, designed with 13 μm domain spacing for SHG of 950 nm radiation. An unannealed proton exchanged waveguide was used, as literature reports indicated that, unlike lithium niobate, lithium tantalate showed no degradation of the electro-optic coefficient after proton exchange[4]. This device did not show any second harmonic generation with CW input radiation. Subsequent measurements using a Q-switched laser also showed no measurable SHG. We then tried annealing the waveguides, and found that the nonlinear coefficient was restored. It thus appears that the structural change associated with proton exchange has a dramatically different effect on the electro-optic and the nonlinear optic susceptibilities. This is not surprising for these ferroelectric oxides, in which the electro-optic coefficient is almost entirely due to ionic motion, while the nonlinear optic coefficient is almost entirely electronic.

A second batch of devices made with annealed proton exchange waveguides also did not work efficiently. This problem is currently being studied, with attention on the effect of the proton exchange process on the domain distributions.

A.6. Open Questions

While the progress in of these structures has been very encouraging, none are yet ready for practical application. The remaining questions revolve around either spatial inhomogeneities (waveguide structure in the planar devices, domain spacing in the bulk devices) or the effect of the fabrication steps on the material properties (control of spatial distribution of domains in titanium or electric field poling, effect of proton exchange on nonlinear susceptibilities, effect of proton exchange on domain orientation in lithium tantalate). In this section our present understanding of these effects is discussed.

In an ideal QPM structure, the dispersion of the medium is compensated by a periodic reversal of the sign of the nonlinear coefficient, with the period of the reversal equal to twice the coherence length. A simple way to understand the effect of QPM on the efficiency of the device is to decompose the patterned nonlinear susceptibility into its component spatial harmonics. For a square modulation of unit amplitude, the coefficient of the m^{th} odd spatial harmonic is $2/m\pi$.

In aperiodic devices, the peak conversion is in general reduced, essentially by the amount that the desired Fourier component of the grating is reduced, with an accompanying broadening of the phasematching bandwidth. The tolerance for these deviations from periodicity depend in detail on the statistics of the deviations. The strictest tolerance is for a simple error in the periodicity, that is, when the structure is periodic, but has the wrong period. For a structure with N domains and coherence length l_c, the allowable fractional error is $\delta l_c / l_c < 1/N$. Of course, such an error can be compensated by changing the wavelength of the laser or the temperature of the crystal slightly. If the domain spacing varies linearly through the crystal, from $l_c - \delta l_c$ to $l_c + \delta l_c$ at the other, the tolerance is $\delta l_c / l_c < 6/N$. If the error is random with an rms magnitude δl_c, the tolerance is $1/\sqrt{N}$. All of these cases can be understood from the general rule that the accumulated error in position of the N^{th} domain must be less than a coherence length. These considerations are discussed in detail in the Ph.D. dissertation of Greg Magel[2] and are being prepared for publication. Note that the structures are rather tolerant of random errors: a 1 mm long structure with 2 μm coherence length can tolerate 4.5% rms jitter in the domain position. The tolerance for taper is smaller, only 1%. The difference is more pronounced for longer structures: for a 1 cm device with 2 μm domains, the tolerances for linear taper and random error are 0.1% and 1.5% respectively.

The effective length of 0.3 mm observed for the bulk material corresponds to an error in domain width of 7% if random and 3% if tapered. The latter is more consistent with observations based on SEM photographs of the domains, and is not surprising in view of the friction-coupled belt-drive system used to translate the crystals during growth.

QPM interactions are much more tolerant of duty cycle variations and missing domains, and so are insensitive to the types of errors likely to occur with lithographic fabrication techniques. In these systems, it is generally the waveguide homogeneity that limits performance, as discussed below.

In waveguide devices two other issues arise: spatially varying dispersion due to inhomogeneities in the structure, and the overlap of the waveguide modes with each other and with the periodically-poled region. Because the propagation constants (described by the "effective refractive index") of the waveguide modes depend on the dimensions of the waveguide, and the dependence is different at different frequencies, variations in the dimensions of the waveguide lead to variations in the phase-mismatch in nonlinear interactions. Thus, a single periodic structure cannot quasi-phasematch the interaction over the entire length of the crystal. The tolerance for this type of inhomogeneity in the effective refractive index of the modes is the same as the tolerance for inhomogeneities in the refractive index of a bulk crystal. For a constant error, the tolerance can be estimated from $\Delta kL < \pi$, so that allowable error in the index difference between the fundamental and the second harmonic is $\delta n < \lambda/2L$. For a 1 cm long waveguide, the tolerance is then on the order of 5×10^{-5}.

To translate this tolerance on index dispersion errors to one on structural homogeneity in the waveguide, we must connect changes in waveguide dimension to changes in waveguide dispersion. We have carried out this calculation for several types of waveguide; the results discussed here for step profile waveguides are representative. In general, the sensitivity of the effective index to the waveguide dimensions scales with the core-cladding index difference, and inversely with the waveguide thickness. Thus, tightly confining waveguides, which produce the smallest effective area for the modes, also produce the greatest sensitivity to waveguide inhomogeneities. We can quantify these notions by writing the effective index as a Taylor series in the waveguide thickness:

$$\delta(n_{2\omega} - n_{\omega}) = \frac{\Delta n}{\rho}\left(g_1(r, V)\,\delta\rho + \frac{1}{\rho}g_2(r, V)\,(\delta\rho)^2\right)$$

where n_ω and $n_{2\omega}$ are the effective indices of the modes at the fundamental and second harmonic, δ indicates a small deviation in a quantity, Δn is the core-cladding index difference, ρ is a characteristic dimension of the waveguide, r is the ratio of Δn at the fundamental and second harmonic wavelengths, $V = (2\pi \rho / \lambda)\sqrt{2 n \Delta n}$ is the normalized frequency , and g_1 and g_2 are dimensionless functions on the order of unity.

For typical cases, g_1 is approximately 1/2, and we can find for $\Delta n \approx 0.01$ that the tolerance for a fixed error is $\delta\rho/\rho < 1\%$ in a 1 cm long, 3 μm wide waveguide. For a linear taper, the tolerance is ≈ 6%. These tolerances, while attainable, are difficult, so it is desirable to find conditions under which the constraints are relaxed. If $g_1 = 0$, there is no first order dependence on ρ of the difference in n_ω and $n_{2\omega}$, so that the tolerance scales inversely with the square root of the length of the device, rather than inversely with the length of the device, and "non-critical" phasematching is achieved. This noncritical point typically falls within the single-mode operating range of the fundamental, and increases the tolerance for variations in the waveguide width by an order of magnitude for the case described above. We have tested these predictions by measuring the effective indices at 916 nm and 458 nm for a series of proton exchanged waveguides and plotting the difference as a function of the depth of the waveguides. We find that a turning point occurs at $V = 2$, as predicted theoretically. These results are shown in figure 6. Incorporation of this design concept into our next generation of QPM devices is expected to yield substantial improvements in the effective length of the devices without necessitating any improvement in the quality of the lithography. A patent has been filed on these noncritically phase-matched devices.

The overlap of the waveguide modes with the periodically reversed domains is another point that must be considered in optimizing the performance of the devices. The efficiency is reduced if the penetration depth of the domains is smaller than that of the waveguide modes. A quantitative analysis of these effects is given in the appended *Proc. SPIE* article by Fejer, Magel, and Lim.[1] We have found that under the processing conditions that we currently use, domains shallower than their width are essentially rectangular in cross section, while those that penetrate to a depth comparable to their period become triangular. From our current measurements, it appears that the reduced overlap of the waveguide modes with these triangular domains contributes to the discrepancy between the observed and the theoretical conversion efficiency.

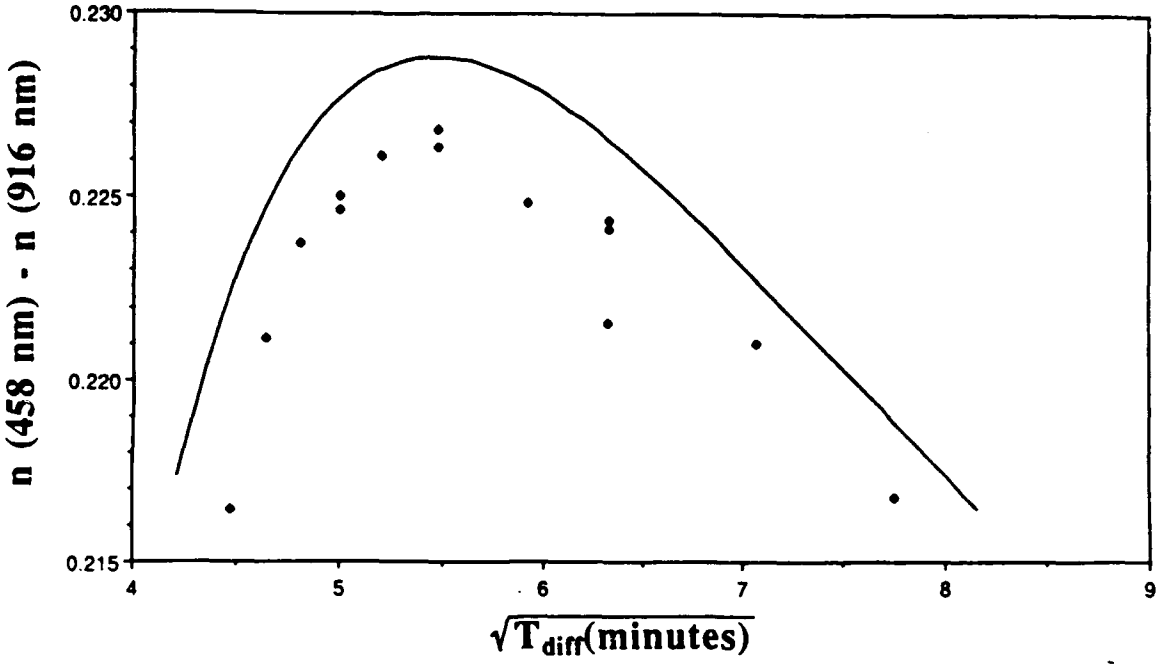

Figure 6: Difference between the effective indices of refraction for the fundamental and second harmonic mode in a lithium niobate waveguide as a function of waveguide depth (as given by square root of diffusion time). Solid line is theory, points are experimental measurements. Note the appearance of a turning point where there is no first order dependence of the dispersion on the waveguide depth.

The waveguide fabrication process used in these devices, annealed proton exchange, is less well characterized than several other waveguide processes, but has a combination of low temperature processing, low-loss performance, resistance to photorefractive damage, and retention of the nonlinear susceptibility that is not currently available by any other process. The nonlinear dependence of both the diffusion coefficient and the index of refraction on the proton concentration, and the "aperture effect" (effect of the mask material on the diffusion of the protons), exacerbate the difficulties associated with characterization of this process. The dependence of the nonlinear susceptibility on the proton concentration further clouds the issue of waveguide optimization for QPM devices. While we have evolved workable recipes for producing waveguide QPM devices, better understanding of the dependence of the waveguide and nonlinear properties on the process conditions would lead to better device designs.

B. Epitaxially-Grown Semiconductors

Periodically-poled lithium niobate comes close to defining a generic approach to the design of a nonlinear medium suited to the visible and NIR part of the spectrum. However, this material system has some limitations: The multiphonon absorption at wavelengths greater 4 μm in lithium niobate limits its use to visible and near-infrared interactions, and, since no technology for the growth of high quality lithium niobate films on GaAs substrates currently exists, the pump laser must be coupled to a waveguide fabricated on another substrate. Approaches based on epitaxially grown semiconductors could in principle extend the accessible wavelength range to the far-infrared, and would allow integration of the device on the same substrate as the pump. At present, these approaches are promising, but less well-developed than the oxide ferroelectrics.

Present epitaxial growth techniques make possible control of electronic and dielectric properties on the scale of a single atomic layer. This unprecedented design freedom has led to widespread interest in the application of epitaxially grown semiconductors in electronic and optical devices. The spatially varying bandgap produces quantum wells whose unique electronic properties, e.g. 2-d excitons and intersubband transitions, lead to a variety of interesting optical properties. We have studied the optical phenomena associated with the intersubband transitions, and initiated studies of phenomena based on patterning the bulk properties of III-V and II-VI semiconductors. The samples used in our studies to date were grown by J. S. Harris's group in Stanford's Electrical Engineering Department. We will continue this collaboration with his group in the future, and have begun work with the J. Gibbons group on II-VI materials.

B.1. Intersubband Transitions in III-V Quantum Wells

Our first studies of nonlinearities in nanostructures involved far-infrared intersubband transitions in AlGaAs quantum wells. We note that these are entirely different from the heavily studied excitonic nonlinearities observed at the band-edge (≈ 800 nm) in AlGaAs quantum wells. The bound states of electrons in the conduction band of an AlGaAs quantum well (subbands) can be accurately pictured as the "particle in a box" states familiar from basic quantum mechanics. Transitions between these subbands have large dipole matrix elements (oscillator strengths on the order of m_e/m^*, or 15 for GaAs), tunable energy differences typically resonant with 5 - 15 μm radiation, and narrow linewidths (the ground and excited subbands have approximately the same curvature). These large matrix

elements and resonant enhancements lead one to expect large nonlinear susceptibilities. Since square wells are inversion symmetric, their second order susceptibility vanishes, and enhancement occurs only in the third order susceptibilities. Large second order susceptibilities can be obtained in systems in which the inversion symmetry is broken either through asymmetric composition or doping profiles, or through the application of a bias electric field.

Our first work in this area, characterizing the absorption spectra and electric-field induced second harmonic generation of a Q-switched CO_2 laser in square AlGaAs wells was reported in the *Phys. Rev. Lett.* by Fejer, Yoo, Byer, Harwit, and Harris[5] included in the Appendix to this report. Extremely large second order susceptibilities, 70 times larger than bulk GaAs were observed. These nonlinearities are among the largest measured in any medium. Modelling the electronic properties of the quantum well in the effective mass approximation, with corrections for nonparabolicity and band bending, and calculating the optical properties in a self-consistent (Hartree) approximation yields results in good agreement with the experimental data. The results of calculations are shown, along with the experimental data, in figure 7.

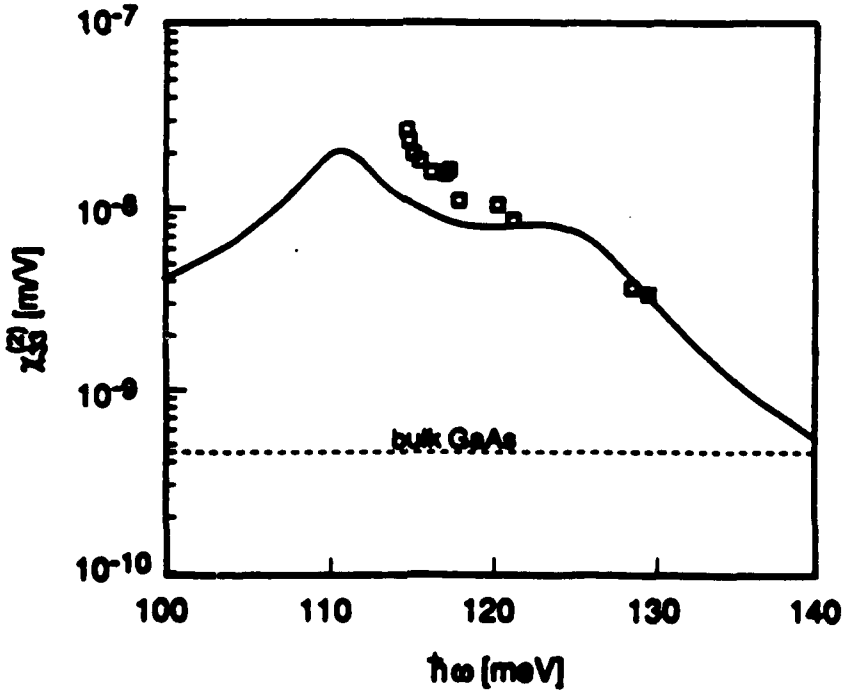

Figure 7: Calculated nonlinear susceptibility for second-harmonic generation $\chi^{(2)}$ as a function of the energy of the fundamental photon. Squares are the experimental measurements.

Our present work involves extension of the theoretical and experimental results to more complex quantum wells with larger ratios of nonlinearity to loss. We are characterizing compositionally asymmetric structures (InGaAs/GaAs/AlGaAs) grown by the J. S. Harris group in the Electrical Engineering department, and asymmetrically doped structures developed by L. C. West at the AT&T Holmdel Lab, both of which should exhibit nonlinearities 1 - 2 orders of magnitude larger than the electric-field -biased wells previously studied. Theoretical calculations indicate that asymmetric coupled wells should have even larger ratios of nonlinearity to loss. Work also continues in designing samples for measurements on quantum wells embedded in a waveguiding layer. In addition their use in efficient application of the quadratic susceptibilities already measured, the waveguide geometry will be useful for measurements of the resonant dispersion, AC and DC Kerr effects, and saturation intensities associated with the intersubband transitions.

Since the sign of the nonlinear susceptibility depends on the sign of the applied field, interesting device geometries based on spatial or temporal modulation of the nonlinear susceptibility are possible, including QPM with periodic electrode structures. One could also pattern the nonlinearity in quantum wells with built-in asymmetries, for example by using impurity induced disordering to locally eliminate the quantum wells, and hence the nonlinear susceptibility.

We are also improving the characterization equipment, setting up an FTIR spectroscopy facility with the low-temperature group of T. Geballe, M. Beasley and A. Kapitulnik in the Applied Physics department to cover the entire $10 - 50000\ cm^{-1}$ range. For nonlinear spectroscopy, we have obtained the components and crystals for a lithium niobate parametric oscillator pumped with a Q-switched Nd:YAG laser, and a frequency differencer for the signal and idler in a silver gallium selenide crystal to provide radiation tunable from 2 - 15 μm, covering a large part of the range important for intersubband physics.

B.2. Other Semiconductor Films

While the bulk nonlinearities in II-V and III-V semiconductors are generally quite large, it is difficult to use them for frequency conversion devices because, as cubic crystals, they have no birefringence for phasematching. Building on the QPM waveguide approach developed with lithium niobate, we have begun investigations of techniques for laterally patterning the bulk nonlinear properties of epitaxially grown films, with the ultimate goal of

building QPM devices monolithically on the same substrate as the pump laser. Since these semiconductors are not ferroelectric, other means for controlling the nonlinear susceptibility must be used. One approach is to periodically induce disorder in the films, eliminating the nonlinearity in the randomized region and thereby achieving on-off modulation for QPM. The studies are in their early stages, but promising approaches both for ZnO films produced in our microfabrication lab, and GaAs films produced through MBE by the J. S. Harris group in the Electrical Engineering department show promise.

While considerable effort will be necessary to bring these systems into control, the payoff is well worth it, both for the large available nonlinearities (d[GaAs] $\approx 20 d_{15}$[$LiNbO_3$]), visible operation with II-VI crystals, and for eventual integration with laser sources.

C. Single-Crystal Sapphire Fibers

Single-crystal sapphire fibers have been an ongoing part of this project, both as a model system for fiber growth, and for applications requiring optical fibers with extended IR transparency, resistance to high temperatures and chemical attack, low-toxicity, and good mechanical properties. The growth technique is laser-heated pedestal growth, with a 12 W CO_2 laser as the heat input. Details of the system appeared in previous reports, and in the *Appl. Phys. Lett* . by Jundt, Fejer, and Byer[6] found in the Appendix.

For typical energy delivery and sensor applications, low-loss fibers several meters in length are required. We have grown 110 μm diameter sapphire fibers with lengths up to 2.5 meters, and characterized their optical and mechanical properties relevant to device applications. The scatter losses, measured with an integrating sphere at several wavelengths, were less than 0.2 dB/m for 458 nm $<\lambda <$ 2900 nm. The absorption losses, measured calorimetrically and by total throughput measurements, had a minimum of 0.3 dB/m at 1060 nm, rose to 0.9 dB/m at 2936 nm, and had a pronounced peak at 410 nm. The visible absorption band is probably due to a color center, and thermochemical bleaching techniques to reduce its magnitude are being investigated. The fibers are quite strong: 4 mm bend radii have been demonstrated in 150 μm diameter fibers.

An important potential application of these fibers is as a flexible delivery medium for 2.9 μm radiation from an Er:YAG laser for surgical applications. We have tested fibers with a pulsed Er:YAG laser, and found that in vitro ablation of post-mortem arterial tissue was possible with 6 mJ, 110 μs long pulses, 20 times lower energy than the observed end-face damage threshold. These results were sufficiently encouraging that several samples have been distributed to medical researchers for in vivo studies in animals.

Detailed studies of the dynamic response of the growth process to perturbations, and thermal effects contributing to the growth dynamics have been carried out, and the resulting data are currently being analyzed.

D. Other Lithium Niobate Studies

D.1. Vapor-Transport-Equilibrated Lithium Niobate

It is well known that $LiNbO_3$ exists over a range of compositions, commonly specified by the ratio Li/[Li + Nb], of 0.5 to 0.41. The birefringence, and therefore the phasematching temperature, of the crystal depend strongly on the composition. It has not in the past been possible to exploit this control over the phasematching, because high optical quality crystals can be grown only from the congruently melting composition, 0.486. It was discovered by Holman, in the course of investigating the phase diagram of $LiNbO_3$, that the composition can be modified by vapor phase transport of lithium oxide into the crystal from powders of known composition[7]. For example, heating a crystal of congruent lithium niobate in the presence of lithium-rich powder results in a crystal equilibrated to the phase boundary near the 0.50 (stoichiometric) composition.

In the course of our studies of $LiNbO_3$ fibers, we measured the optical properties of stoichiometric lithium niobate fabricated by the vapor-phase equilibration (VTE) technique.[8] The birefringence, and therefore the phasematching temperature, are increased considerably with respect to the congruent composition. The phasematching temperature *vs* fundamental wavelength are shown in figure 8 for several types of $LiNbO_3$. The phasematching temperature at 1.06 μm for the stoichiometric crystal, 238° C, is the highest reported to date, and is well above the annealing temperature for photorefractive damage. We have demonstrated 45% efficient SHG of the output of a Q-switched Nd:YAG laser in such stoichiometric crystals. It was also possible to double 954 nm input radiation to generate 473 nm light. This is the first demonstration of blue light generation in bulk $LiNbO_3$. One further benefit of this process is that the final composition of the crystal is determined by a thermodynamic equilibrium, and is therefore extremely homogeneous. The inhomogeneities, as measured from the width of the phasematching curves for second harmonic generation, are not resolvable for crystals as long as 4 cm.

In order to better assess the device potential of this material, we made careful measurements of the index of refraction as a function of temperature and wavelength, and fit the data with a two-pole Sellmeier equation, which was verified by comparison to parametric fluorescence measurements. These results are discussed in detail in the *IEEE J.Quant. Electron.* paper by Jundt, Fejer, and Byer[9] in the Appendix. Phasematching calculations based on the Sellmeier equation show that room temperature second harmonic

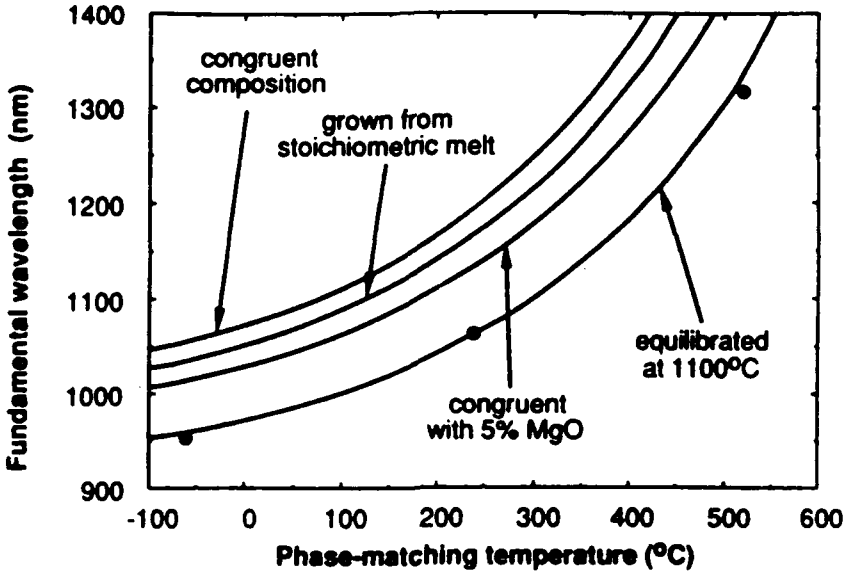

Figure 8: Comparison of predicted phase-matching conditions for different crystal compositions. Circles depict experimental data points for equilibrated $LiNbO_3$.

generation of wavelengths as short as 488 nm should be possible in stoichiometric lithium niobate.

Another interesting aspect of this technique is the possibility of producing crystals with a Li/Nb ratio smaller than congruent. The reduced birefringence associated with such compositions would permit operation of long wavelength devices such as 1.32 μm doublers and noncritically phasematched 1.06 μm optical parametric oscillators to operate at reasonably low temperatures. We have carried out studies of the VTE process for compositions within the existence range in collaboration with Peter Bordui at Crystal Technology, Inc. We measured the phase-matching temperature for SHG of 1.06 μm and 1.32 μm radiation as a function of Li/Nb ratio, while the Crystal Technology group measured the Curie temperature of the same samples, whose compositions ranged from 47% to the lithium-rich phase boundary. Because it is much easier to control the solid composition with this vapor-phase technique than with melt growth, we know the compositions of the samples to better than 0.01 mol%. Our results are thus of interest both because they provide a "key" allowing the results of the past two decades of lithium niobate research to be correlated to an absolute concentration scale, as well as showing the large range of birefringence, and hence phasematching temperatures, accessible with the VTE process. These results are being prepared for publication. The Crystal Technology group

has produced VTE crystals 2 mm thick and 75 mm diameter. These samples are being fabricated for assessment in device configurations.

Studies of VTE magnesium doped lithium niobate are also underway. It has been observed that the birefringence of lithium niobate increases both with increasing Li/Nb ratio, and with Mg doping. It was hoped that co-doping with both Mg and Li would increase the birefringence more than either of the dopants alone. The VTE process is a convenient one for studying this system, as several samples of different Mg/Nb ratio could be easily equilibrated to a series of different Li/Nb ratios, without the need to grow a new crystal for each data point. This study is not yet complete, but it appears from the available data that the highest birefringence is obtained with crystals with no Mg, and a Li/Nb ratio at the lithium-rich phase boundary.

D.2. Other Dopants in Lithium Niobate

We have undertaken studies of Nd and Zn diffusion in lithium niobate for waveguide devices, in collaboration with R. S. Feigelson's group in the Materials Science department. The former dopant is of interest for waveguides with gain, while the latter, a divalent ion that raises the indices of refraction of lithium niobate, was of interest in connection with waveguides resistant to photorefractive damage. Preliminary results of both studies are encouraging. We have obtained diffusion coefficients and activation energies for both species, and have found diffusion conditions under which it is possible to maintain the optical quality of the bulk material and a smooth surface on the substrate. The Zn diffuses rapidly, producing single-mode waveguides in approximately 12 minutes at 1100°C. Four orders of magnitude larger transmitted power without photorefractive damage at 532 nm has been observed in planar Zn waveguides than in similar Ti-indiffused waveguides. This is a very encouraging result for future high-power waveguides, and is being prepared for publication. The Nd in-diffused layers also performed well. We have produced 2 μm thick layers with 0.2 wt.% Nd, and measured fluorescence lifetimes ≈ 100 μs, similar to that of bulk crystals. The index of refraction change induced by the Nd is not large enough to produce a waveguide by itself, but we have followed the Nd in-diffusion with an annealed proton exchange process to produce a waveguide in the Nd doped crystal. These devices are currently being characterized, with preliminary results indicating losses smaller than 1 dB/cm. Unlike waveguides fabricated in uniformly doped substrates, this technology allows selective doping to provide gain at desired portions of the integrated-optic device, and can be extended to other wavelengths, e.g. 1.5 μm, with other dopants like Er.

E. Polysilane Thin Films

For future applications, polymeric materials have attracted a great deal of attention because of the ease of manipulating these materials by spin coating and standard lithography techniques. Although π-bonded carbon backbone polymers have been the usual substances studied for nonlinear applications, the new class of silicon backbone polymers, called polysilanes, is promising as well. These polymers consist of a long (>1000 atoms) backbone of σ-bonded silicon atoms, with two organic substituent groups attached to each Si atom. Polysilanes volatilize upon exposure to ultraviolet light, making them an efficient self-developing lithography material and have therefore been extensively investigated in the earlier part of the decade as photoresists. They have also been investigated as possible photoconductors, and as precursors to silicon carbide formation. A review of polysilane properties has recently been published by Miller and Michl[10].

Attention has recently turned to investigation of the nonlinear optical properties of these materials. These properties should be analogous to the extensively studied carbon-based polydiacetylene polymer system, with the delocalized electrons provided by the conjugation of the σ-bonded backbone, rather than conjugated π-bonds. Polysilanes, however, have several advantages as nonlinear materials. First, because of the interest in these materials as photoresists, the capability of fabricating thin (≤ 4 μm) films of excellent quality has already been developed. Second, the $\sigma \rightarrow \sigma^*$ absorption edge is typically ≈ 3.9 eV, so the material is transparent at all visible wavelengths. Finally, this absorption band edge is related to the unperturbed length of the silicon backbone, and can be shifted by adding various substituent groups to the silicon backbone, making resonant enhancement of various nonlinear effects at particular wavelengths possible.

Of special interest for nonlinear optical applications is the compound poly(di-n-hexylsilane), a polymer with two hexyl chains attached to each Si atom. At temperatures below 42°C, the hexane side chains undergo a crystallization which forces the Si backbone (normally helical) into a planar zigzag conformation. This crystallization occurs only on a microscopic scale; no evidence of spontaneous macroscopic orientation has been observed for this compound. The higher dipole moment associated with this new orientation can be seen in the formation of a strong absorption shifted from 313 nm (the peak for the amorphous region) to 375 nm, and also in a dramatic increase in the $\chi^{(3)}$ nonlinearity. Third harmonic generation measurements by Baumert *et al.* at IBM[11] have shown this may

be as large as an order of magnitude as the material goes through this phase transition. They report a value of $\chi^{(3)}(-3\omega;\ \omega,\omega,\omega) = 11.2 \times 10^{-12}$ esu (at $\lambda = 1.06\ \mu m$) for the crystalline phase.

A great deal of progress has been made in the past year in the study in the nonlinear optical properties of polysilane polymers. As has been reported last year, we have observed highly anisotropic birefringence caused by polymer chain scission induced through multi-photon photoexposure, with the axes of orientation determined by the exposing laser polarization. In contrast, polarized UV exposure induces an anisotropic response only in a shallow skin, due to strong polymer absorption, and the net birefringence for a film of waveguide dimensions is quite small. This high degree of polarization 'memory' produced by nonlinear photoexposure of isotropic materials is, to our knowledge, unique to the polysilanes. The effect can be as large as $\Delta n \approx 0.03$, and has the potential for many useful applications, and a patent describing these applications has been submitted. These include the formation of birefringent gratings and variable waveplates through photoexposure, as well as the patterning of integrated optical devices or encoding of digital information. We have characterized birefringent diffraction gratings fabricated by pulsed laser holography in our laboratory, and have observed grating efficiencies as high as 8%, with a polarization diffraction ratio greater than 10:1, as discussed in the appended *Opt. Lett.* by Schellenberg, Byer, and Miller.[12]

Our earlier work has concentrated on fabrication and characterization of polysilane films for use as birefringent waveguides and optical elements. This work was carried out in collaboration with R.D. Miller and J. Zavislan of the IBM Almaden Research Center. It was found that correct choice of polymer molecular weight, solvent, and spinning conditions can produce thin films and waveguides of excellent optical quality, and that the fabrication of birefringent gratings and optical elements was fairly straightforward.[13]

More recently, we have concentrated on a spectroscopic study of the multi-photon absorption to determine the origins of the effect. This experiment measures the polarization state of a He-Ne probe while inducing birefringence in the polymer film by exposure to pulsed dye laser light. The nonlinear absorption coefficient was then calculated from the measured birefringence growth curves, and determined for a variety of wavelengths and laser powers. In this experiment, we observe a clear quadratic dependence of the birefringence effect on laser power, indicating that the photochemistry is caused by two-photon absorption. Considering that two-photon absorption is also a $\chi^{(3)}$ process, it is not surprising that this is the case. A simple mathematical model, based on polarization

selective decomposition of an ensemble of randomly distributed polymer backbones, describes the growth and decay of the birefringence with exposure within experimental error. This is in marked contrast to UV induced single-photon photochemistry, which involves rapid energy transfer of the excitations to chains of other orientations.

The spectrum of the two-photon absorption for the polymer poly(di-n-hexylsilane) reveals some surprising features. These results have been reported in the appended *Chem. Phys. Lett.* by Schellenberg, Byer, and Miller[14]. The spectrum is generally characterized by a broad gaussian band, centered at 570 nm (corresponding to a two-photon energy of 4.35 eV). The width of this band is ≈400 meV, similar to the width of the absorption bands observed in single photon absorption (≈360 meV). However, superimposed on the broad peak is a sharp resonance at 579 nm (corresponding to a two-photon energy of 4.28 eV) with a linewidth of ≈30 meV. On resonance, the two-photon absorption is enhanced by as much as a factor of 5, to a value of $\beta \approx 1.5$ cm/MW (corresponding to $\mathrm{Im}\chi^{(3)} \approx 1 \times 10^{-9}$ esu). A plot of the two-photon absorption spectrum is seen in figure 9, along with a plot of the single photon absorption.

These measurements have concentrated on the determination of β, which is proportional to Im $\chi^{(3)}$. Associated with this transition should be a significant enhancement in Re $\chi^{(3)}$ as well. Because these two components of $\chi^{(3)}$ are related through the standard Kramers-Kronig relationship, it is possible to estimate the value of the nonlinear index of refraction n_2 for this polymer due to the two-photon resonance. A calculation of the nonlinear dispersion for poly(di-n-hexylsilane), based on our two-photon absorption measurements, is shown in fig. 10. The curve shows the characteristic dispersion lineshapes due to the broad band and the sharp spike, and indicates a spectral region with low two-photon absorption where the nonlinear index is significantly enhanced. The values of n_2 in this region (700-640 nm) are comparable with the nonlinearities observed in polydiacetylenes.

Commercial diode lasers are available which operate in this spectral region. Although these lasers are generally low power devices, when focussed into a waveguide with a few microns cross sectional area, the intensity becomes high enough to drive several proposed nonlinear switching devices. The ease of modulating the intensity of these laser sources, combined with the ease of fabricating and patterning polysilane waveguides, suggests that the polysilanes may have application as a material for demonstrating several nonlinear integrated optical switching devices that have currently existed only on paper due to the lack

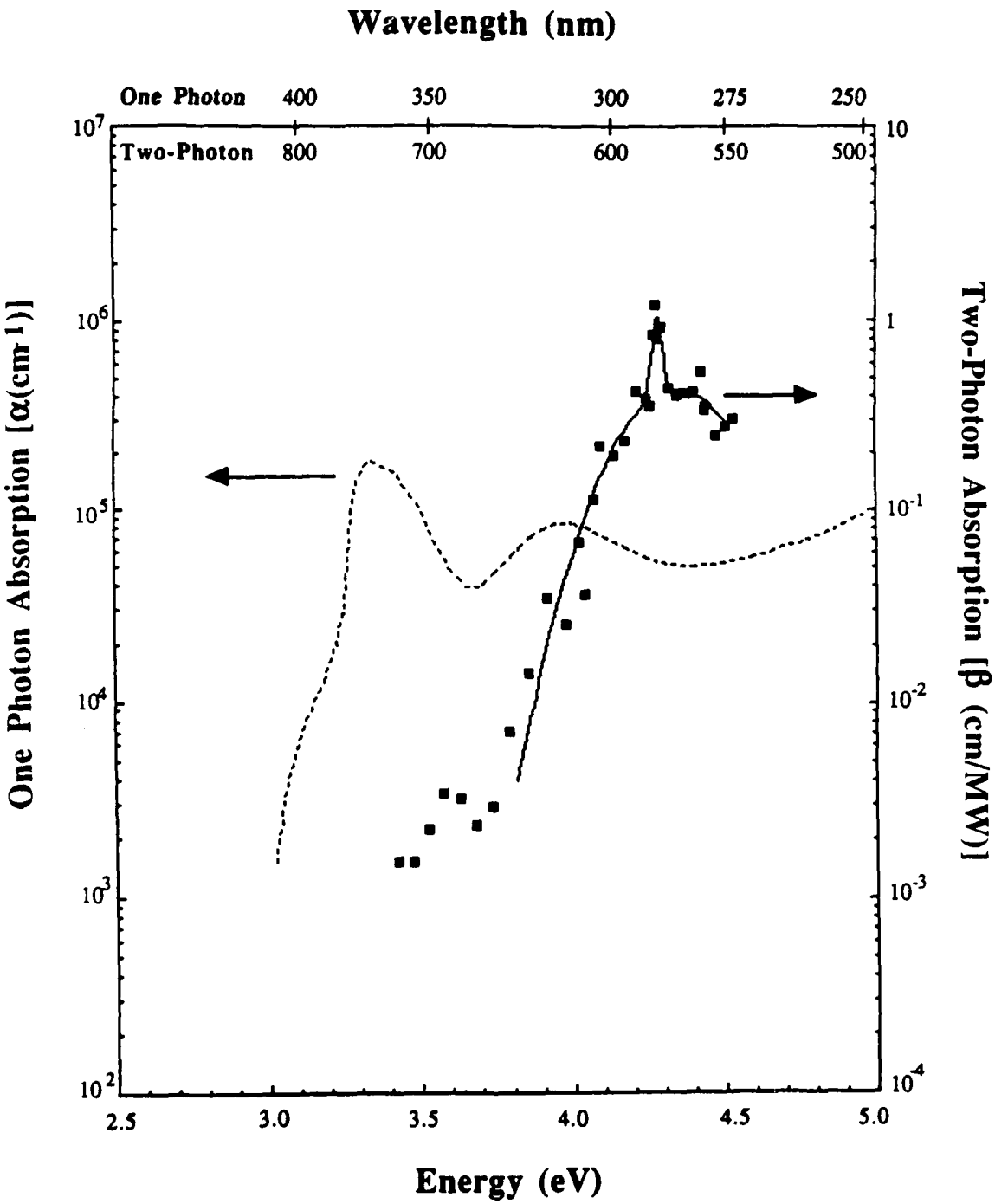

Figure 9: Spectrum of the two photon absorption coefficient β in cm/MW for poly(di-n-hexylsilane), calculated from birefringence growth curves, as a function of two-photon energy (•), compared with the single photon absorption spectrum (- - -). Solid line is a least squares fit to β using the sum of two gaussians, one broad (≈412 meV), the other narrow (≈33 meV).

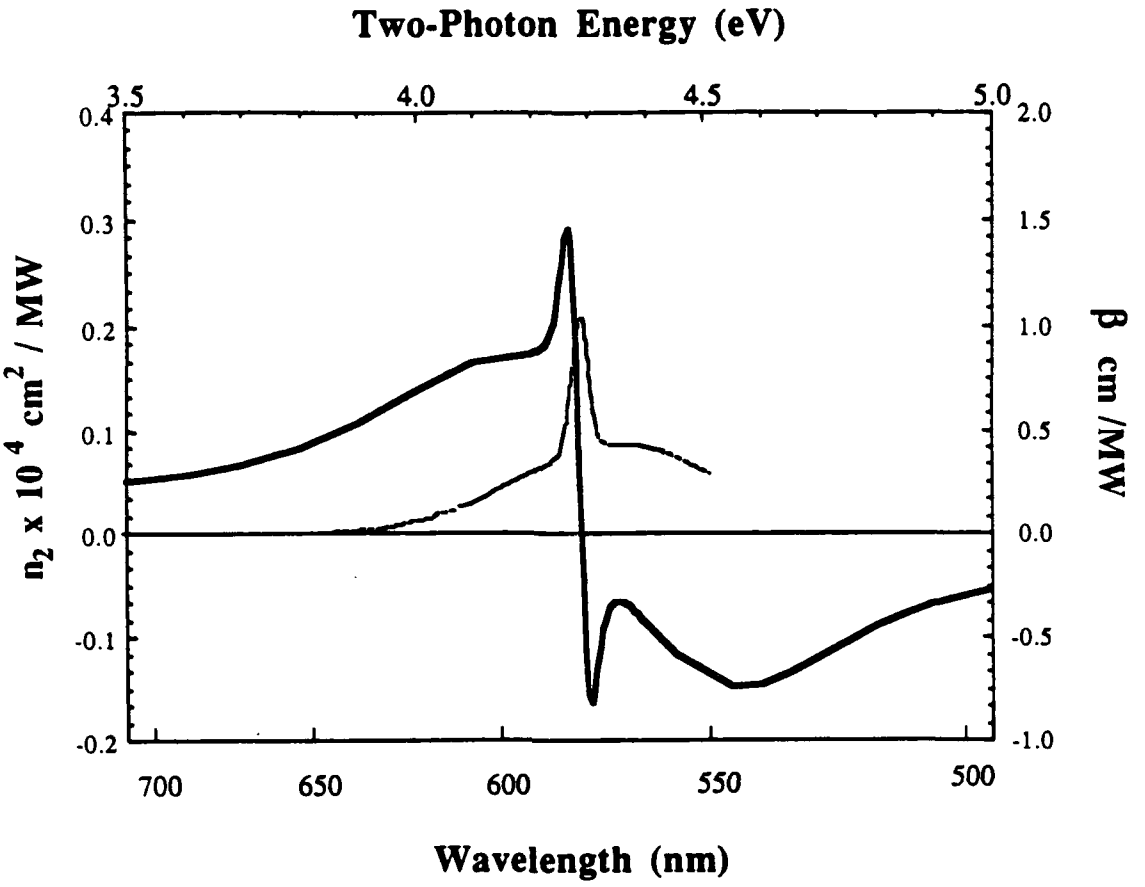

Figure 10: Nonlinear index of refraction n_2 for poly(di-n-hexylsilane), calculated from the measured two-photon absorption coefficient β.

of an appropriate nonlinear material. Preliminary measurements of n_2 for this polymer have yielded values 2-4 times higher than those calculated, although more research must be carried out to insure this is not a thermal effect but is in fact a nonlinear optical effect.

Single photon excitations decay both through chain scission and fluorescence, and it is therefore expected that two-photon excitations also decay by fluorescence. As can be seen in figure 11, emission from two-photon excitations in poly(di-n-hexylsilane) is identical to that observed from UV excitations, in spite of the increase in the excitation energy by more than ≈1eV. These fluorescence experiments were carried out at the University of Tokyo's Research Center for Advanced Science and Technology, with the assistance of Dr. S. Kano and Y. Takahashi of the IBM Tokyo Research Lab. The laser used was a sub-picosecond mode-locked dye laser, focussed onto the polymer film to produce similar power densities as were found in the birefringence experiment. Fluorescence was collected into a spectrometer with an OMA attachment. This indicated that emission either occurs by transfer along the chain to other, lower energy chain segments, or to local low energy traps. In view of the success of the birefringence growth model (with no assumption of energy transfer in the two-photon case), we now expect emission is due to conformal traps. Recent absorption measurements using low molecular weight polymers tend to support this hypothesis, although further work must be done to determine the exact nature of these traps.

Low temperature measurements of the two-photon fluorescence intensity as a function of wavelength for constant power agree well with the previously measured two-photon absorption spectrum. In this case, the excitation spectrum consists of a broad band and a sharp spike, with the same line centers and line widths found in the birefringence experiment. A comparison of these two results is shown in figure 12. At room temperature, however, the fluorescence intensity is reduced by a factor of ≈15, and no sharp spike is observed, in spite of the fact that a sharp spike is observed at room temperature in the birefringence spectrum. Decay of the fluorescence with time is also observed at room temperature (but not at low temperature). This suggests that the decay paths of fluorescence and chain scission are complementary, and that scission occurs more rapidly with thermal assistance.

Several models for the electronic structure of polysilanes have been proposed in the literature. Mintmire[15] and others have extensively modeled these polymers as infinite one-dimensional semiconductors. In this model, the lowest energy σ–σ^* optical absorption at ≈3-4 eV corresponds to the direct band gap of these materials. These band structure calculations also predict the existence of a delocalized π^* band approximately 1 eV above the σ–σ^* transition, coincident with the energy difference we observe in two-photon absorption. Although a direct σ–π^* transition is normally symmetry forbidden, it might be

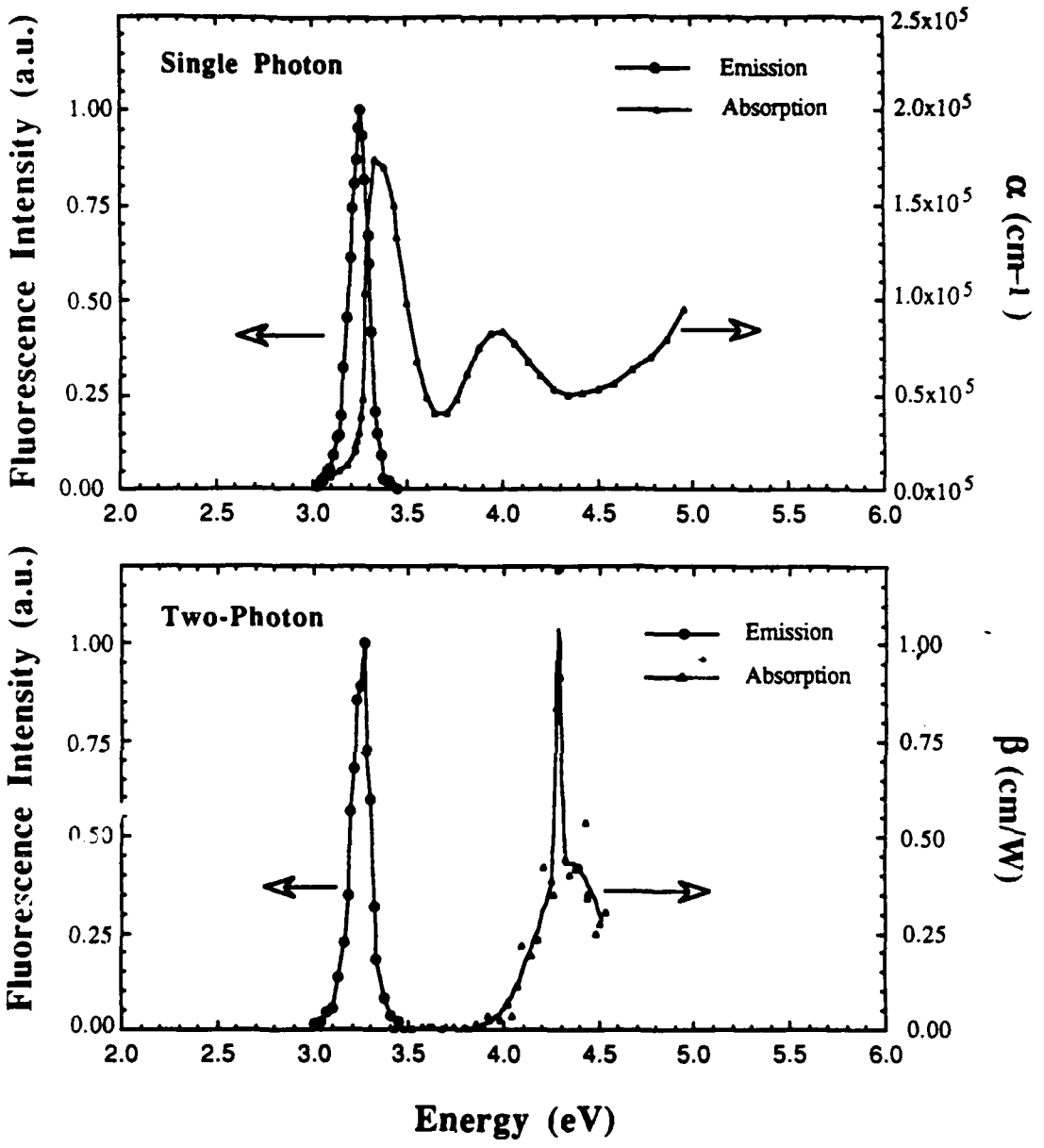

Figure 11: Upper) Absorption and emission for single photon absorption

Lower) Absorption and emission for two-photon absorption.

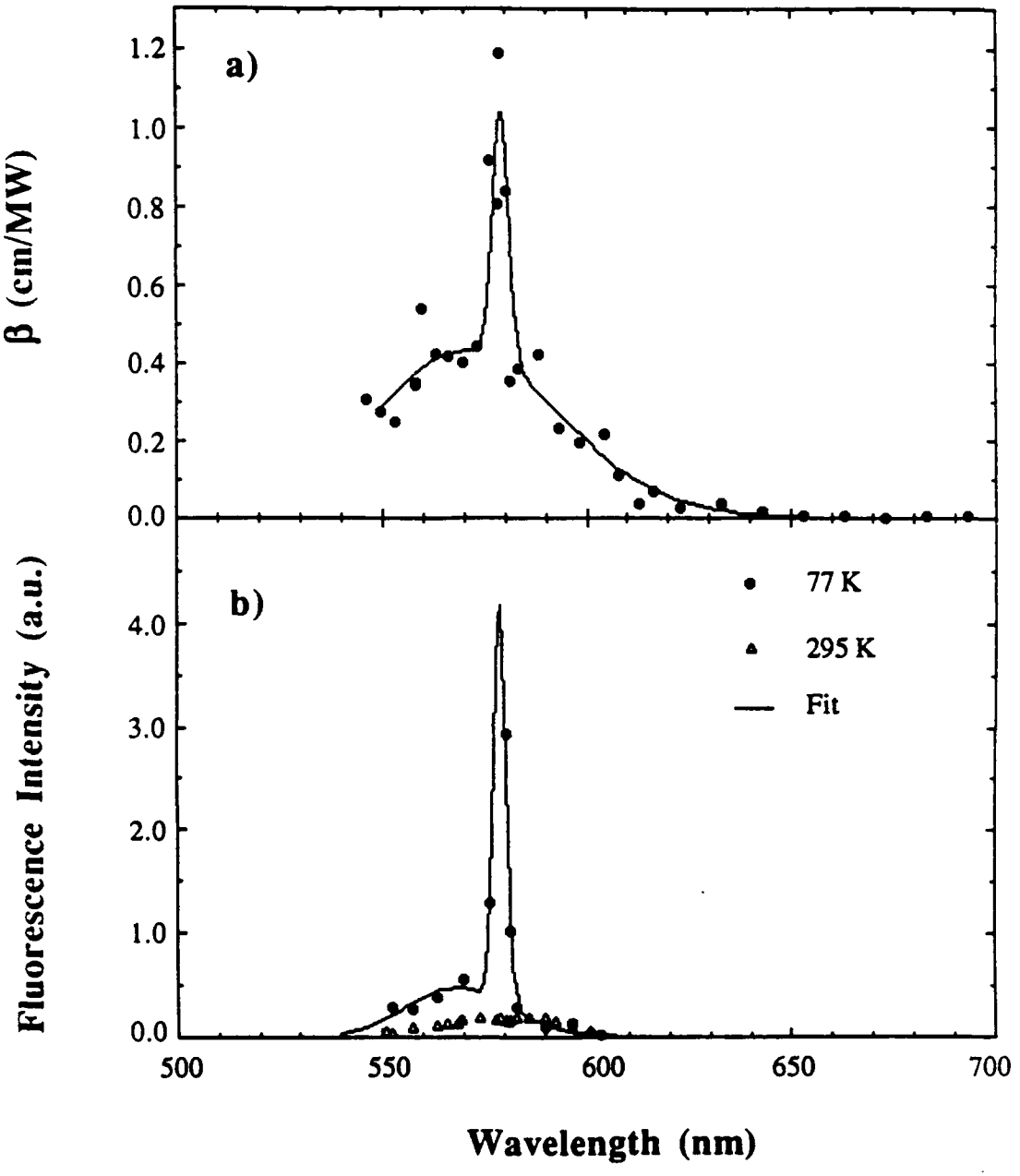

Figure 12: a) Plot of β for poly(di-n-hexylsilane) calculated from birefringence growth curves (•) on a linear scale as a function of exposing wavelength. The solid line is the double gaussian of fig. 9.

b) Linear plot of fluorescence for poly(di-n-hexylsilane) vs. exposing wavelength for both 77 K (•) and room temperature (Δ). The solid line is a least-squares fit of the sum of two gaussians to the low temperature data, adding one broad feature (≈234 meV) and one narrow (≈25 meV).

allowed for two-photon absorption and could be a possible explanation for spectrum we observe. Even though these *ab initio* calculations underestimate the energy of the lowest transition by about 40%, the calculated energy shifts for various regular backbone conformations correlate well with those actually measured for a number of polysilanes of known structure, giving some credibility to the model and the methods used.

In fact, the polysilanes are not infinite one-dimensional chains. Several measurements[10] have determined that the polysilanes in the solid state are linear only over 20-50 silicons, restricted at each end by conformal kinks that electronically isolate the chain segment. Several recent papers have discussed the similarity of the excitations in polysilanes to π-conjugated carbon systems, such as the polydiacetylenes, in which the lower energy transitions are excitonic in nature[16]. These authors suggest that the first direct UV transition may be due to a tightly bound Frenkel exciton, in which an electron hole pair created by the photon move together down the polymer chain. They propose the two-photon excitation might produce a more loosely bound exciton, in which the electron transfers one or two silicon atoms from the hole. Although the electron and hole in this charge transfer exciton case would still travel as a pair, it would conceivably be less probable for this type of exciton to move intact through conformal kinks at the end of a chain segment. If correct, this may give a possible explanation for the very different birefringence results for the two types of excitation, in which one appears to exhibit energy transfer while the other does not. Further measurements are, however, necessary to determine if this model is in fact a satisfactory explanation of the electronic structure of the polysilanes.

IV. SUMMARY

We have studied a variety of oxide, semiconducting and polymer media suitable for guided wave and nonlinear optics, and demonstrated device applications of several. The effort was focussed on the use of standard fabrication technologies to modify available media to suit a broad range applications, rather than on developing entirely new material systems for a specific application. The advantages of this approach are the large body of knowledge already available for the basic media, and the low cost inherent in their ready commercial availability, which make possible rapid progress towards practical devices. Emphasis was placed on media for nonlinear frequency conversion applications, such as periodically-poled lithium niobate for SHG of green and blue light, and SHG of 9 - 11 μm radiation using intersubband nonlinearities in AlGaAs quantum wells, but other media for guided wave devices were also studied, including sapphire fibers for delivery of infrared laser beams and polysilane thin films for birefringent guided wave devices.

Perhaps the most important result of this project is the development of "generic" media like periodically-poled lithium niobate, which can be adapted easily to a solve a variety of problems. For example, after our first demonstration of quasi-phase-matched SHG of green light , it was a matter of weeks until a new set of masks were obtained to produce the shorter periods necessary for the generation of blue light. This powerful approach will be exploited in the near future for other devices like difference frequency generators and parametric amplifiers in the lithium niobate system, and in the longer term extension to other media like II-VI semiconductors will allow integration of nonlinear frequency convertors with diode pump lasers for truly monolithic devices.

REFERENCES

1. M. M. Fejer, G. A. Magel, and E. J. Lim, "Quasi-phase-matched interactions in lithium niobate", *Proc. SPIE* **1148**, 213 – 224 (1989).

2. G. A. Magel, "Optical Second Harmonic Generation in Lithium Niobate Fibers", Ph.D. dissertation, Stanford University (1990).

3. G. A. Magel, M. M. Fejer, and R. L. Byer, "Quasi-phase-matched second harmonic generation of blue light in periodically-poled $LiNbO_3$", *Appl. Phys. Lett.* **56**, 108 – 110 (1990).

4. Y.S. Li, K. Tada, T. Murai and T. Yuhara, "Electrooptic Coefficient r_{33} in Proton-Exchanged z-Cut $LiTaO_3$ Waveguides", *Jpn. J. Appl. Phys.* **28**, L263-L265 (1989)

5. M.M. Fejer, S.J.B. Yoo, R.L. Byer, A. Harwit, and J.S. Harris Jr, "Observation of Extremely Large Quadratic Susceptibility at 9.6 - 10.8 μm in Electric-Field Biased Quantum Wells", *Phys. Rev. Lett.* **62**, 1041-1044 (1989)

6. D. H. Jundt, M. M. Fejer, and R. L. Byer, "Characterization of single-crystal sapphire fibers for optical power delivery systems", *Appl. Phys. Lett.* **55**, 2170– 2172 (1989).

7. R.L. Holman, "Novel uses of gravimetry on the processing of crystalline ceramics", in *Processing of Crystalline Ceramics* (*Mat.Sci. Rev.*, vol 11), H. Palmour and R.F. Davis, eds. (New York, Plenum, 1978)

8. Y. S. Luh, M. M. Fejer, R. L. Byer, and R. S. Feigelson, "Stoichiometric $LiNbO_3$ for nonlinear optical applications", *J. Cryst. Growth* **85**, 264 (1987).

9. D. H. Jundt, M. M. Fejer, and R. L. Byer, "Optical Properties of Lithium-Rich Lithium Niobate Fabricated by Vapor Transport Equilibration", *IEEE J. Quantum Electron.* **26**, 135 – 138 (1990).

10. R.D. Miller and J. Michl, "Polysilane High Polymers", *Chem. Rev.* **89**, 1359 (1989)

11. J.C. Baumert, G.C. Bjorklund, D.H. Jundt, M.C. Jurich, H. Looser, R.D. Miller, J. Rabolt, R. Sooriyakamaran, J.D. Swalen, and R.J. Twieg, "Temperature dependence of the third-order nonlinear optical susceptibilities in polysilanes and polygermanes", *Appl. Phys. Lett.* **53**, 1147-1149 (1988).

12. F.M. Schellenberg, R.L. Byer, and R.D. Miller, "Fabrication of birefringent gratings using nonlinear polysilane thin films", *Opt. Lett.* **15**, 242-244 (1990)

13. F.M. Schellenberg, R.L. Byer, J. Zavislan, and R.D. Miller, "Nonlinear Polysilane Thin Films", in *Nonlinear Optics of Organics and Semiconductors*, T. Kobayashi, ed. (Springer Verlag, New York, 1989), pp. 192-196;

14. F.M. Schellenberg, R.L. Byer, and R.D. Miller, "Two-photon-induced birefringence in polysilanes", *Chem. Phys. Lett.* **166**, 331-339 (1990)

15. J.W. Mintmire, "Conformal effects in organopolysilanes: A first-principles approach", *Phys. Rev. B* **39**, 13350 (1989)

16. J.R.G. Thorne, Y. Ohsako, J.M. Zeigler, and R.M. Hochstrasser, "Two-photon spectroscopy of polysilanes", *Chem. Phys. Lett.* **162**, 455 (1989)

V. PUBLICATIONS, PRESENTATIONS, AND PATENTS

This list covers the period since September 1988. All the listed publications acknowledge AFOSR support.

A. Publications

1. D. H. Jundt, M. M. Fejer, and R. L. Byer, "Growth and optical properties of single-crystal sapphire fibers," *Proc SPIE* **1048**, 39 - 43 (1989).

2. M. M. Fejer, S. J. B. Yoo, R. L. Byer, A. Harwit, and J. S. Harris, Jr., "Observation of Extremely Large QuadraticSusceptibility at 9.6 – 10.8 μm in Electric-Field-Biased Quantum Wells," *Phys. Rev. Lett.* **62**, 1041-1044 (1989).

3. E. J. Lim, M. M. Fejer, and R. L. Byer, "Second Harmonic Generation of Green Light in a Periodically-Poled Planar Lithium Niobate Waveguide," *Electron. Lett.* **25**, 174-175 (1989).

4. E. J. Lim, M. M. Fejer, R. L. Byer, and W. J. Kozlovsky, "Blue light generation by frequency doubling in a periodically poled lithium niobate channel waveguide," *Electron. Lett.* **25**, 731-732 (1989).

5. D. H. Jundt, M. M. Fejer, and R. L. Byer, "Characterization of single-crystal sapphire fibers for optical power delivery systems," *Appl. Phys. Lett.* **55**, 2170 – 2172 (1989).

6. G. A. Magel, E. J. Lim, M. M. Fejer, and R. L. Byer, "Second harmonic generation in periodically-poled lithium $LiNbO_3$," *Optics News* **15** (12), 20-21 (1989).

7. M. M. Fejer, G. A. Magel, and E. J. Lim, "Quasi-phase-matched interactions in lithium niobate," *Proc. SPIE* **1148**, 213 – 224 (1989).

8. G. A. Magel, M. M. Fejer, and R. L. Byer, "Quasi-phase-matched second harmonic generation of blue light in periodically-poled $LiNbO_3$," *Appl. Phys. Lett.* **56**, 108 – 110 (1990).

9. D. H. Jundt, M. M. Fejer, and R. L. Byer, "Optical Properties of Lithium-Rich Lithium Niobate Fabricated by Vapor Transport Equilibration," *IEEE J. Quantum Electron.* **26**, 135 – 138 (1990).

10. F. M. Schellenberg, R. L. Byer, and R. D. Miller, "Fabrication of biefringent gratings using nonlinear polysilane thin films," *Opt. Lett.* **15**, 242-244 (1990).

11. F. M. Schellenberg, R. L. Byer, and R. D. Miller, "Two-photon induced birefringence in polysilanes," *Chem. Phys Lett.* **166**, 331-339 (1990).

B. Invited Presentations

1. M. M. Fejer, "New Media for Nonlinear Optics," AACG/West, Fallen Leaf Lake, CA, June 1988.

2. M. M. Fejer, "Optoelectronic Materials and Structures," Stanford Materials Research Forum, Stanford, CA, May 1989.

3. M. M. Fejer, "Engineering Lithium Niobate for Optical Applications," NCCG Meeting, Palo Alto, CA, May 1989.

4. M. M. Fejer, "Tailored Materials for Quadratic Nonlinear Optics," Gordon Conference on Nonlinear Optics and Lasers, Wolfeboro, NH, July 1989.

5. M. M. Fejer, "Quasi-phasematched Interactions in Lithium Niobate," SPIE Symposium on Optical and Optoelectronic Applied Science and Engineering, San Diego CA, August 1989.

6. M. M. Fejer, "Nonlinear Media For Optical Frequency Conversion Applications," Ninth International Conference on Crystal Growth, Sendai, Japan, August 1989.

7. M. M. Fejer and E. J. Lim, "Quasiphasematched SecondHarmonic Generation in Lithium Niobate Waveguides," Integrated Photonics Research Conference, Hilton Head S.C., March 1990.

8. M. M. Fejer, "Second Order Nonlinearities in Asymmetric Quantum Wells," IQEC, Anaheim CA, May 1990.

C. Patents

1. M. M. Fejer and R. L. Byer, "Nonlinear Optical Processes in Electric-Field-Biased Quantum Wells," patent number 4,880,297, issued 1989.

2. Y. S. Luh, M. M. Fejer, R. L. Byer, and R. S. Feigelson, "Tailored Properties of Lithium Niobate for Nonlinear Optical Applications by Vapor Transport Equilibration," pending.

3. A. Cordova, S. Sudo, M. M. Fejer, M. Digonnet, C. Gaeta, H. J. Shaw, R. L. Byer, "Claddings for Single Crystal Fibers and Devices and Methods and Apparatus for Making Such Claddings," pending.

4. E. J. Lim, M. M. Fejer, and R. L. Byer, "Optical Radiation Generator amd Method of Forming Regions of Dominant Electrical Polarization Domains in Solid State Bodies," pending.

5. G. A. Magel, M. M. Fejer, and R. L. Byer, "Method of Producing Monocrystalline Rods Having Regions of Reversed Dominant Ferroelectric Polarity and Method for Clarifying Such a Rod," pending.

6. E. J. Lim, and M. M. Fejer, "Waveguide Devices with Large Tolerance for Dimensional Variations," pending.

7. F. M. Schellenberg, "Birefringent Structures Formed by Photo-Exposure of Polymer Films and Method of Fabrication Thereof," pending.

VI. PERSONNEL ASSOCIATED WITH THE PROGRAM

Robert L. Byer — Principal Investigator
Professor, Applied Physics

Martin M. Fejer
Assistant Professor, Applied Physics

Robert C. Eckardt
Senior Research Associate, Ginzton Laboratory

Graduate Students, Byer Group:

Dieter H. Jundt

Eric J. Lim

Mei Lü

Franklin M. Schellenberg

S. J. Ben Yoo

Graduate Students, Robert S. Feigelson Group (Materials Science and Engineering)

Whu-Ming Young

Visiting Scholar

Hans Hertz — Lund University, Sweden

Advanced degrees awarded:

Gregory A. Magel, Ph.D., January, 1990.
Dissertation title: Second Harmonic Generation in Lithium Niobate Fibers

VII. APPENDIX

The following papers are appended for reference:

1. M. M. Fejer, G. A. Magel, and E. J. Lim, "Quasi-phase-matched interactions in lithium niobate," *Proc. SPIE* **1148**, 213 – 224 (1989).

2. G. A. Magel, M. M. Fejer, and R. L. Byer, "Quasi-phase-matched second harmonic generation of blue light in periodically-poled $LiNbO_3$," *Appl. Phys. Lett.* **56**, 108 – 110 (1990).

3. M. M. Fejer, S. J. B. Yoo, R. L. Byer, A. Harwit, and J. S. Harris, Jr., "Observation of Extremely Large Quadratic Susceptibility at 9.6 – 10.8 μm in Electric-Field-Biased Quantum Wells," *Phys. Rev. Lett.* **62**, 1041-1044 (1989).

4. D. H. Jundt, M. M. Fejer, and R. L. Byer, "Characterization of single-crystal sapphire fibers for optical power delivery systems," *Appl. Phys. Lett.* **55**, 2170 – 2172 (1989).

5. D. H. Jundt, M. M. Fejer, and R. L. Byer, "Optical Properties of Lithium-Rich Lithium Niobate Fabricated by Vapor Transport Equilibration," *IEEE J. Quantum Electron.* **26**, 135 – 138 (1990).

6. F. M. Schellenberg, R. L. Byer, and R. D. Miller, "Fabrication of biefringent gratings using nonlinear polysilane thin films," *Opt. Lett.* **15**, 242-244 (1990).

7. F. M. Schellenberg, R. L. Byer, and R. D. Miller, "Two-photon induced birefringence in polysilanes," *Chem. Phys Lett.* **166**, 331-339 (1990).

PROCEEDINGS REPRINT

SPIE—The International Society for Optical Engineering

Reprinted from

Nonlinear Optical Properties of Materials

Howard R. Schlossberg
Raymond V. Wick
Chairs/Editors

10–11 August 1989
San Diego, California

Volume 1148

Quasi-phase-matched interactions in lithium niobate

M. M. Fejer, G. A. Magel, and E. J. Lim

Edward L. Ginzton Laboratory
Stanford University, Stanford, California 94305

ABSTRACT

Phase-matching nonlinear interactions by periodic variations in the nonlinear susceptibility, quasi-phase-matching, offers advantages in accessible tuning range and in choice of nonlinear coefficients over the conventional birefringent technique. Periodically reversed ferroelectric domains can be used to create monolithic structures with the necessary high-spatial-frequency variations in the nonlinear susceptibility. We present two techniques for the fabrication of periodically-poled lithium niobate crystals, and results for bulk and guided-wave second harmonic generation of blue and green light.

1. INTRODUCTION

Recent advances in III-V diode laser technology have led to the commercial availability of near-infrared diode lasers with single mode output powers in excess of 100 mW. The more difficult materials problems involved in producing similar diode lasers for the visible or the mid-infrared have not yet been solved. Thus, nonlinear optical devices suitable for frequency conversion of existing diode-laser pump sources are of considerable technological interest. Because single-pass bulk nonlinear devices cannot operate efficiently at the pump powers available with diode lasers, resonant enhancement of the fundamental fields,[1,2] or waveguide confinement[3,4] is necessary for the generation of useful amounts of output radiation. Materials used in these devices must meet stringent requirements on their nonlinear susceptibility, transparency, and particularly on their birefringence for phase-matching. Lithium niobate, which has large nonlinear susceptibilities, transparency from 350 nm – 4000 nm, well-developed waveguide technologies, and ready commercial availability, is an attractive material for these applications. Unfortunately, the usefulness of lithium niobate is limited by its birefringence, which is too small for second harmonic generation (SHG) of blue light and too large for noncritical phase-matching of difference frequency generation of mid-infrared radiation. We describe here the use of periodic poling to achieve quasi-phase-matching, extending the applicability of lithium niobate to any interaction within its transparency range.

2. QUASI-PHASE-MATCHING

Phase-matching, broadly defined as a means for maintaining the phase relationship between the waves participating in a nonlinear interaction, is essential for efficient frequency-conversion devices. Conventionally, the phase velocity mismatch caused by dispersion of the refractive indices is compensated by use of a birefringent crystal to match the velocity of orthogonally-polarized waves. While birefringent phase-matching has been used in essentially all practical nonlinear devices, it limits the choice of nonlinear crystals to those having appropriate relationships between dispersion and birefringence, and forces the use of only those elements of the nonlinear susceptibility tensor that couple orthogonally polarized waves. Alternative approaches to phase-matching, such as modal dispersion[3] or the Cerenkov effect[4] in waveguides, are generally accompanied by reduced conversion efficiency and nonoptimal output spatial modes.

Another approach, quasi-phase-matching (QPM), was proposed early in the development of nonlinear optics.[5,6] In QPM, the interacting waves travel with different phase velocities, but accumulation of phase mismatch is prevented through appropriate spatial modulation of the sign or magnitude of the nonlinear

susceptibility. Using second harmonic generation (SHG) as an example, the wavevector mismatch Δk is given by

$$\Delta k = k_{2\omega} - 2\,k_{\omega} \ , \tag{1}$$

where the subscripts ω and 2ω refer to the fundamental and second harmonic frequencies, respectively. QPM is achieved by introducing a component of the nonlinear susceptibility with a spatial frequency equal to Δk . In the simplest form of modulation, the sign of the nonlinear susceptibility is reversed every coherence length ($l_c \equiv \pi/\Delta k$), so that the sign of the coupling coefficient between the fundamental and the second harmonic is changed at every point where a phase shift of π accumulates between the two waves. A monotonic increase in the magnitude of the second harmonic wave then results, instead of the periodic oscillation characteristic of non-phase-matched interactions. In a more general case, the sign reversal occurs every m coherence lengths. The effective nonlinear coefficient for the quasi-phase-matched interaction, d_Q, is then related to the effective nonlinear coefficient for a conventional interaction involving the same waves, d_{eff}, by the component at spatial frequency Δk of the Fourier expansion of the square wave, i.e.

$$d_Q = \begin{cases} (2/m\pi)d_{eff} & \text{for } m \text{ odd} \\ 0 & \text{for } m \text{ even} \end{cases} \ . \tag{2}$$

Note that d_Q for mth order QPM is inversely proportional to m, so that the efficiency of nonlinear devices, proportional to $(d_Q)^2$, decreases as m^{-2}. First-order interactions are thus desirable from the standpoint of efficiency, but higher-order QPM is sometimes used for ease of fabrication. The more general case where the duty cycle is not 50% is discussed in section 3.

The advantages of QPM result from the decoupling of phase-matching from material birefringence. With QPM, one can use a material for any interaction within its transparency range, adjust for phase-matching at any convenient temperature, use any of the nonlinear coefficients (including those coupling waves of the same polarization), and carry out interactions in waveguides that support only one polarization (proton exchange in lithium niobate). In many materials, the nonlinear coefficients coupling fields of the same polarization are often larger than those coupling orthogonally-polarized fields. For lithium niobate, d_{33} = 34 pm/V,[7] so that d_Q for this polarization, 22 pm/V, is 3.7 times larger than the d_{31} coefficent used for birefringent phase-matching, and the efficiency of QPM devices is 13 times larger than that of comparable birefringently phase-matched devices.

In order to be useful for device applications, the periodicity of the domains must be accurately controlled. If the spacing of the domains deviates from the ideal structure, phase error accumulates between the interacting waves, and the efficiency is reduced. The tolerance for such errors depends on the statistical nature of the variations and the length, L, of the device. It can be shown that for small random errors, the efficiency is reduced by 50% when the rms deviation, $\delta\Lambda$, of the domain period, Λ, is[8]

$$\delta\Lambda/\Lambda = (1/\pi)\sqrt{l_c/L} \tag{3}$$

while for a fixed deviation, $\Delta\Lambda$, a 50% reduction occurs when

$$\Delta\Lambda/\Lambda = (2.78/\pi)\,l_c/L \ . \tag{4}$$

Eq. (4) states essentially that the useful length of the structure is the length over which the accumulated error in the position of the last layer is one coherence length. Note that this is a rather strict criterion, since typical coherence lengths are on the order of microns and typical devices are millimeters long.

Because typical coherence lengths for interactions involving visible light are 1–10 μm, a major difficulty in QPM is modulation of the nonlinear susceptibility on the rather short spatial scale necessary for efficient interactions. The conceptually simplest approach to creation of the sign reversal, cutting the crystal into a series of wafers one coherence length long and restacking the slices with alternating 180° rotations, is feasible only for far-infrared interactions.[9,10] This difficulty can be avoided with monolithic techniques based on the sign changes in the nonlinear susceptibility associated with rotational twinning,[11] partial orientation of polymer films,[12] or reversed ferroelectric domains.[13]

Our studies of QPM have been focused on lithium niobate, which undergoes a ferroelectric transition at a Curie temperature, T_C, of approximately 1150°C to a low temperature phase with spontaneous polarization oriented parallel to the crystallographic z-axis.[14] Antiparallel ferroelectric domains, which are related crystallographically to one another by a 180° rotation around the x-axis, can easily be induced at temperatures close to T_C, but are extremely difficult to reorient at room temperature.[14] Because the signs of all components of the nonlinear susceptibility tensor change in adjacent domains, crystals with appropriately-spaced periodic domain reversals (periodically-poled lithium niobate or PPLN) can be used to achieve QPM.

Domain reversal has been induced during Czochralski growth of bulk lithium niobate crystals by periodic perturbation of the growth conditions, either through a pulsed current passed through the crystal[15] or by rotation of the crystal in an asymmetric thermal field.[16] Reversed domains with periods as small as 6.8 μm have been created by these techniques.

We report here two methods for producing PPLN crystals, one based on indiffusion of lithographically patterned dopants on planar substrates, the other based on modulation of the heat input during laser-heated pedestal growth of small diameter crystals. Frequency conversion experiments are also described, including SHG of green and blue light in planar and channel waveguides fabricated by proton exchange in the planar substrates, and bulk SHG of blue light in the pedestal-grown crystals.

3. PLANAR DEVICES

Waveguides enhance the efficiency of nonlinear optical interactions because they maintain high optical intensities over long interaction lengths. Previous guided wave devices for frequency conversion have relied on birefringence, modal dispersion, or the Cerenkov effect for phasematching. Guided wave devices using quasi-phase-matching techniques are particularly attractive for frequency conversion applications because they combine the high efficiency resulting from waveguides with the advantages of QPM discussed previously.

It is convenient to define a normalized conversion efficiency, η_{nor}, which accounts for the effective nonlinear coefficient of the material, the overlap of the fundamental and harmonic waveguide modal fields, and the effects of quasi-phase-matching. The normalized conversion efficiency η_{nor} of a quasi-phase-matched waveguide frequency doubler is related to the absolute conversion efficiency, η, by

$$\eta = \frac{P_{2\omega}}{P_{\omega}} = \eta_{nor} P_{\omega} L^2 , \tag{5}$$

where P_{ω} and $P_{2\omega}$ are the powers of the fundamental and harmonic, respectively, and L is the length over which QPM occurs.

The ideal configuration for a waveguide device which relies on periodic sign reversals of the nonlinear susceptibility for QPM requires a sign-reversal grating with a 50% duty cycle that is constant over the depth of the waveguide. In this case, η_{nor} is given by

$$\eta_{nor} = \frac{8\pi^2 d_Q^2}{n_\omega^2 n_{2\omega} c\varepsilon_0 \lambda_\omega^2} \left| \int_{-\infty}^{+\infty} E_{2\omega}^*(y)\, E_\omega^2(y)\, dy \right|^2 \tag{6}$$

where y is the depth coordinate, E_ω and $E_{2\omega}$ are the normalized modal field distributions, and n_ω and $n_{2\omega}$ are the corresponding modal effective indices of the waveguide. We have assumed a planar waveguide for simplicity; the analysis for a channel waveguide requires an additonal integral in the width dimension. The integral in Eq. (6) reflects the confinement and overlap of the modes, and is the same as appears in the theory of conventionally phase-matched waveguide interactions.[3]

In the general nonideal case, the sign reversals of the nonlinear susceptibility can be aperiodic and can vary over the depth of the waveguide. A function $g(y,z)$, taking the values ± 1, can be used to specify the spatial variation of the nonlinear coefficient according to $d_{eff}(y,z) = |d_{eff}| g(y,z)$. As will become evident from the experimental results which follow, we are interested in the nonideal periodic structure which consists of a sign-reversal grating whose duty cycle varies over the depth of the waveguide. In this case

$$\eta_{nor} = \frac{8\pi^2 d_Q^2}{n_\omega^2 n_{2\omega} c\varepsilon_0 \lambda_\omega^2} \left| \int_{-\infty}^{+\infty} G_m(y)\, E_{2\omega}^*(y)\, E_\omega^2(y)\, dy \right|^2 \tag{7}$$

Here d_Q takes the value $2d_{eff}/m\pi$ for even as well as odd m. The new quantity $G_m(y)$ in the modal overlap integral is the m^{th} coefficient of the Fourier series representation of $g(y,z)$, normalized to $(2/m\pi)$,

$$G_m(y) = \left(\frac{m\pi}{2}\right) \frac{1}{\Lambda} \int_0^\Lambda g(y,z)\, e^{-i(2m\pi/\Lambda)z}\, dz \tag{8}$$

For ideal, 50% duty-cycle structures with no depth dependence, G_m becomes 1 for odd m and 0 for even m, recovering the results of Eq. (6). If the penetration depth of the domains is small compared to the depth of the waveguide, the overlap integral in Eq. (7) can be substantially smaller than that for the ideal case.

We have investigated methods for creating arrays of periodically reversed ferroelectric domains at the surface of lithium niobate wafers, in which planar or channel waveguides for quasi-phase-matched nonlinear interactions can be fabricated. The conceptually simplest approach is to use an interdigital electrode to apply a periodic electric field to a crystal heated close to its Curie temperature. The domains will then align with the applied field, and be frozen into a periodic configuration as the temperature is lowered. While this technique has been successfully applied to lithium tantalate, whose Curie temperature is $\approx 620°C$,[17] it is difficult to find suitable electrode materials for lithium niobate. At temperatures close to the Curie temperature of lithium niobate, diffusion of the electrode into the substrate is a problem, especially in the presence of a poling field, which tends to enhance the penetration through electrodiffusion.

An alternative approach was suggested by the work of Nakamura, who observed that an inverted domain appears at the +z surface of lithium niobate plates heated to temperatures close to T_C.[18] The depth of the domain reversal increased with both the soak time at a given temperature and the temperature at a given soak time. One model that explains these results, and is also consistent with domain distributions observed in single crystal fibers, is that the domains align with the temperature gradients in the surface cooled bodies under the influence of thermoelectrically generated fields.[19] The influence of the soak temperature would then be due to the reduction of the coercive field as the temperature approaches T_C, while the influence of the soak time is through increased lithium outdiffusion, which reduces T_C,[20] and hence reduces the coercive field at a given temperature. We carried out further experiments, including suppression of the counter-poling by processing the crystal in a lithium-rich atmosphere, which have tended to support this model. Note that the mechanisms leading to domain reversal in lithium niobate are complex, and other effects due to gradients in the concentration may contribute to observed behavior, as discussed in section 4 below. Details of these measurements are being prepared for publication.[21] The process for periodic poling suggested by these observations is to spatially modulate the concentration of Li by outdiffusion through a periodic mask, and to choose the thermal conditions so that the lithium-poor regions counterpole while the remainder of the crystal does not. While this poling method does not require the application of electric fields, and hence allows insulating mask materials, we again found it difficult to identify an appropriate material for the mask, i.e. one that blocks Li outdiffusion but does not indiffuse into the substrate and is readily removed after the thermal processing. Encouraging results with SiO_2 masks have recently been obtained by Webjörn *et al.*[22]

Since it is difficult to find an electrode or mask material that does not diffuse into lithium niobate at elevated temperatures, a technique based on intentional indiffusion of an innocuous dopant is attractive. We have had success with a method using indiffusion of a patterned Ti film, based on the same principle as the poling method using Li concentration variations described above. Regions doped with Ti have a lower Curie temperature than do undoped regions, so that periodic doping leads to periodic domain inversion after thermal processing. This method was suggested by the observation by Miyazawa that fabrication of Ti-indiffused waveguides on +z substrates is often accompanied by domain reversal.[23,24]

We investigated a range of Ti film thicknesses, stripe widths, soak temperatures, and soak times with the goal of reducing the Ti concentration as much as possible to minimize changes in the refractive index while maintaining well-defined regions of domain reversal with adequate penetration depth for good overlap with the waveguide modes. As the number of parameters is large, an optimum process has not yet been identified, but useful results have been obtained with 50–300 Å thick Ti films patterned with liftoff lithography, process temperatures of 1000–1100°C, and soak times less than one hour. Bearing in mind the isotropic nature of Ti diffusion,[25] the parameters should be chosen to prevent excessive overlap of the Ti distributions from adjacent lines. To prevent simultaneous lithium outdiffusion, the poling process was carried out in a closed alumina boat filled with congruent lithium niobate powder. Details of processes for specific devices are discussed later in this section. Typical results are shown in Figs. 1 and 2, which are photomicrographs of the top (z) and end (y) faces of periodically-poled wafers which have been etched for 30 minutes at room temperature in HF to reveal the domain structure. The sharply delineated domains created by this process can be seen in Fig. 1. The triangular shape of the domains in Fig. 2 is typical for cases where the depth of the reversed regions is comparable to the period of the structure. Domains shallower than the period of the structure tend to be more rectangular in cross-section. As is characteristic of diffusion driven processes, the periodic variations in the dopant concentration that cause the poling tend to wash out if the diffusion depth is larger than the period of the structure, which limits the attainable depth of domain reversal.

To fabricate a waveguide in the periodically-poled substrates, a low-temperature process is desirable to prevent erasure of the domain pattern. Proton exchange, which is typically carried out at 200–300°C, is ideal for this purpose, and has the additional advantage of reducing the photorefractive sensitivity of the waveguide. While waveguides fabricated by this process, which guide only z-polarized modes, cannot be

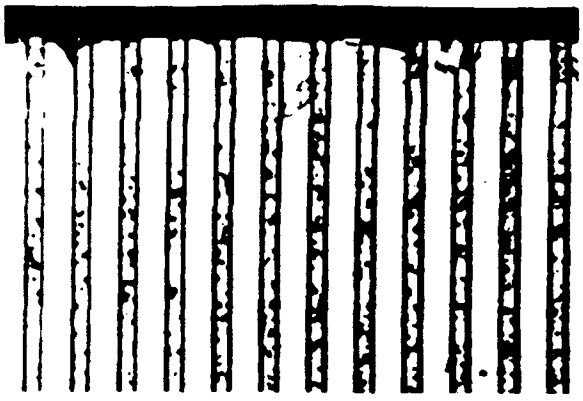

Fig.1. Periodic domains on the z-face of a lithium niobate wafer revealed by etching in HF acid. Period of pattern is 10 μm.

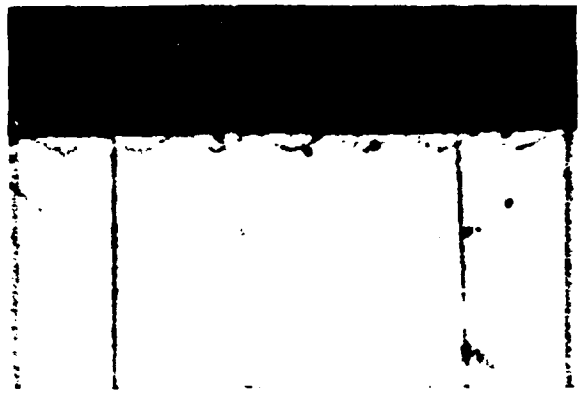

Fig. 2. End-view of periodic domains seen on y-face of lithium niobate wafer. Period of pattern is 10 μm, but sample is not the same as shown in Fig. 1.

used for birefringently phase-matched interactions, they are well-suited to quasi-phase-matched interactions using the d_{33} coefficient, which require only z-polarized modes. Initial experiments suggested that waveguides fabricated by the conventional exchange process in molten benzoic acid had an extremely small nonlinear susceptibility, so we instead used the annealed proton-exchange process from Ref. 26.

The first device that we constructed was a quasi-phase-matched frequency doubler for the 1.06 μm output of a CW Nd:YAG laser.[27] The device was fabricated on the +z face of a 0.5 mm thick lithium niobate substrate obtained from Crystal Technology, Inc. For ease of fabrication, third-order QPM was used, so that the necessary grating period was approximately 18 μm. As the dispersion of the annealed proton-exchanged waveguides is not well-characterized, we fabricated the device with four 1 mm long Ti gratings with periods ranging from 15 to 22 μm arranged so that the pump beam would traverse all four gratings. The Ti gratings consisted of a 50 Å thick film patterned with liftoff lithography into 4 μm wide bars. The heat treatment consisted of a 2 h ramp from room temperature to 1100°C, a 30 min soak at 1100°C, and cooling back to room temperature at an initial rate of 8 K/min. A planar waveguide was then fabricated with a 30 min soak at 200 °C in pure benzoic acid followed by annealing in flowing oxygen at 350°C for 4 h. The resulting waveguide supported one TM mode at 1.06 μm.

Rutile prisms were used for input and output coupling of radiation to characterize the device. The input radiation was focused in the plane of the waveguide with an 8-cm focal length cylindrical lens. A TM-polarized output of 0.5 nW at 532 nm was measured for 1 mW of TM-polarized CW 1.06 μm outcoupled power, yielding a normalized conversion efficiency of 5%/W-cm^2.

To estimate the theoretical conversion efficiency, we modeled the device as a step-index guide with a refractive index difference of 0.003 and an in-plane beam waist of 30 μm. For waveguide depths in the range 4 to 7 μm, the calculated efficiency is 7 to 10%/W-cm^2, in good agreement with the observed conversion efficiency, and approximately 1500 times larger than would have been obtained in the absence of phase-matching.

The next devices used a finer grating to shift the operating wavelength to the vicinity of 800 nm.[28] The poling process was similar to that for the green doubler, but gratings of 6.5, 7, 7.5, and 7.75 μm periods, with 2 μm wide Ti lines were used. The heat treatment, again carried out in a closed crucible filled with congruent lithium niobate powder, was scaled to shorter times because of the shorter grating period. A ramp from room temperature to 1100°C in 2 h was followed by a 10 minute soak at 1100°C and a ramp back to room temperature with an initial cooling rate of 8 K/min. Both planar and channel

waveguides were fabricated in these substrates. The channel waveguides were fabricated by proton exchange through 3 μm wide channels in a 2000 Å thick aluminum film deposited on the substrate. The exchange was in pure benzoic acid for 20 min at 200°C, after which the mask was removed in a solution of sodium hydroxide. The sample was then annealed for 3 h at 350°C in flowing oxygen. Fabrication of the planar waveguides was identical with the exception of the masking step. The end faces of the channel samples were polished to produce a finished device approximately 1 cm long.

Optical measurements of the planar waveguides, which supported one TM mode at 850 nm, were made with a CW Styryl-9 dye laser and prism coupling. The normalized conversion efficiency into the TM_0 mode at 424 nm was 2%/W-cm^2, 5 to 10 times lower than theoretical estimates.

The channel devices were characterized with dye-laser radiation launched through a microscope objective in an end-fire geometry. With an 820-nm pump, the $1/e^2$ in-plane diameter of the fundamental and second harmonic modes were approximately 3.7 and 2.1 μm, respectively, and the out-of-plane diameters were 3.1 and 1.5 μm. The dependence of the output power on the pump wavelength is shown in Fig. 3, along with a sinc^2 curve fitted to the data. The FWHM of 0.5 nm is in reasonable agreement with the theoretical value of 0.4 nm obtained under the assumption that the dispersion of the proton-exchanged material is the same as that of congruent lithium niobate.[29] A plot of the TM polarized output power at 410 nm vs the square of the TM input power at 820 nm is shown in Fig. 4, illustrating the quadratic dependence up to 940 nW, the highest blue output power measured. The internal normalized conversion efficiency, corrected for 14% Fresnel reflection at the end face, is 37%/W-cm^2. The order of magnitude increase in efficiency over the planar device is expected from the in-plane mode confinement, but the conversion remains smaller than the theoretical value. The discrepancy for both the planar and the channel guides is probably due to the shallower domains that result from the short coherence length of this interaction, which reduce the overlap with the modal fields (Eq. 7).

The first step in improving these devices is to increase the length from 1 mm to 1 cm. Since the conversion efficiency scales with the square of the interaction length, one would expect 37%/W conversion in such a device, and thus approximately 1 mW of blue output for 50 mW of infrared input. If the aspect ratio of the domains can be increased through improved processing techniques, the better overlap with the modal fields would yield an order of magnitude increase in the normalized conversion efficiency, to 350%/W-cm^2. Another order of magnitude improvement would result from the use of first-order, rather than third-order, QPM. Such first-order devices would require further increases in the aspect ratio of the domains, or else more strongly guiding waveguides that confine the modes to the periodically-poled region near the surface of the device. Thus, it is interesting to investigate the tradeoff in proton-exchanged waveguides between high proton concentrations for tight confinement and low proton

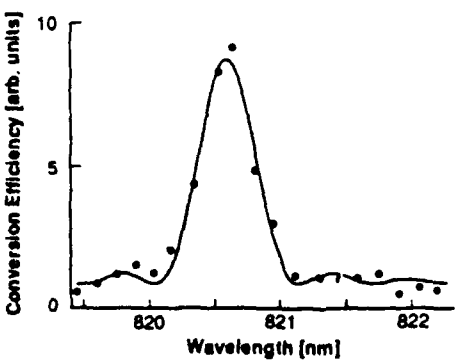

Fig. 3. Experimental wavelength tuning curve for second harmonic generation, shown with a fitted sinc^2 curve.

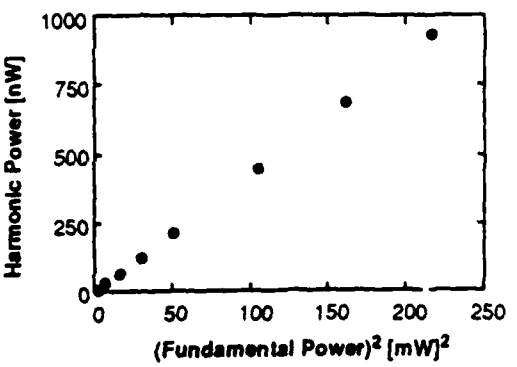

Fig. 4. Measured second harmonic power plotted against the square of the fundamental power, showing the quadratic relation between them.

concentrations to maintain the nonlinear susceptibility. Other topics currently under investigation include mixing two near-infrared sources in a periodically-poled channel waveguide to produce mid-infrared radiation, and the use of periodically-poled lithium tantalate waveguides for higher power applications where photorefractive damage may limit lithium niobate devices. The question of photorefractive damage in periodically-poled crystals is an open one, though indications exist that the magnitude of the effect is dramatically reduced, as is discussed in the following section.

4. LASER-HEATED PEDESTAL GROWTH OF PERIODICALLY-POLED CRYSTALS

An alternative approach to the production of periodically-poled lithium niobate is to grow crystals with reversed domains throughout their volume. Such crystals can be used in bulk optical devices, and would simplify the design of guided-wave devices by eliminating the penetration depth problem described in the previous section. This idea is not new; the effects of domain reversals on nonlinear optical interactions were investigated early in the history of nonlinear crystals.[30] Among the work that has been reported are techniques based on passing a pulsed current through the crystal either during[31] or after[32] growth, growth of a crystal rotated in an asymmetrical temperature field,[16] and growth at a periodically modulated rate.[31] The last of these techniques was employed during Stepanov growth, the remainder were applied to Czochralski grown crystals. However, widespread use of periodically-poled crystals has not yet been possible because of the difficulty in growing crystals meeting the strict periodicity criteria given in Eqs. (3) and (4). The best optical results were reported by Xue *et al.*[33], who demonstrated first order quasi-phase-matched SHG of a 1.06 μm pump in a crystal containing a 6.8-μm-period domain structure, approximately 100 periods of which contributed coherently to the interaction.

We report here on the growth of crystals up to 0.5 mm in diameter containing domain structures with periods as small as 2 μm, and on CW SHG of radiation with wavelengths as short as 407 nm.[34]

The crystals are grown in a laser-heated pedestal growth apparatus, described in Ref. 35, which uses the focused 10.6 μm output of a CO_2 laser to melt the tip of a typically 500-μm diameter source rod of either congruent composition or nominally 5% Mg-doped lithium niobate.[36] An oriented lithium niobate seed crystal is dipped into the melt, then withdrawn at a constant rate to pull the crystal while the molten zone is replenished by continuously feeding in the source rod. The ratio of the pull rate to the feed rate determines the diameter of the crystal. Crystals are grown either in air or a 4:1 mixture of helium and oxygen, at a typical rate of 2 mm/min. Lengths up to 5 cm of both *x*- and *z*-axis crystals are easily grown. The crystals are brownish after growth, but can be made transparent by annealing in dry flowing O_2 for several hours at 725°C.

Fig. 5. SEM photograph of the *y* face of a polished and etched *x*-axis crystal, showing periodically-alternating domains with a period of approximately 3.5 μm. The curvature of the domains is due to the convex shape of the growth interface.

The domain structure of undoped crystals grown by this technique is discussed in Ref. 19; similar results have been obtained with Mg-doped crystals. *z*-axis crystals grow with a single domain, oriented with +*z* toward the melt, while *x*-axis crystals have a single domain wall perpendicular to the *z*-axis at the center of the crystal, dividing the crystal into two domains with the +*z*-axis pointing outward towards the surface. As discussed in Ref. 19, these patterns are most easily explained with the assumption that the domain orientation is controlled by thermoelectric fields generated by the large temperature gradients present in

this growth process, but composition gradients may also have an influence.

Periodically-poled crystals are grown by periodically perturbing the growth, either by rotating an asymmetric heat input created by a rotating mask in the CO_2 laser beam or by modulating the laser power. The period of the domain structures is given by $\Lambda = v_{pull} / f_{mod}$, where v_{pull} is the pull rate and f_{mod} is the frequency of the modulation. Using these techniques, it has been possible to produce domain structures with periods as small as 2 μm in both z- and x-axis crystals (Fig. 5). It is difficult to explain these results in terms of a model based on thermoelectric effects; it is probable that the domain reversals result from compositional striations induced by the periodic perturbation of the freezing interface. Models based on composition gradients have been advanced to explain the domain structures in bulk periodically-poled crystals.[37] While the microscopic mechanism responsible for the domain reversals remains a topic of current research, it appears that the large axial temperature gradients, high growth rates, and short dwell time at elevated temperatures characteristic of the laser-heated pedestal growth system aid in the formation of well-defined domain structures with small periods.

The sample used in the nonlinear optical experiments discussed here is a 1.77-mm long piece of a Mg-doped x-axis crystal approximately 250 μm in diameter, grown at a rate of 2 mm/min while the laser power was modulated at f_{mod} = 12.35 Hz. The resulting domain period, $\Lambda \approx 2.7$ μm, was chosen so that SHG using either the d_{33} or the d_{22} coefficient could be first-order quasi-phase-matched within the tuning range of a CW Styryl-9 dye laser. Figure 6 shows the phase-matching curves generated by tuning the wavelength of the dye laser, focused with a 5× microscope objective to a 6 μm diameter spot in the crystal. Curves (a) and (b) were obtained by polarizing the fundamental wave along the z and y axes, respectively. As expected, the polarization of the second harmonic was the same as that of the fundamental in both cases. The difference in the peak wavelengths, 814.5 nm for d_{33} and 850.5 for d_{22}, is due to the difference between the dispersion of n_e and and that of n_o.

The quality of the sample can be estimated from the effective interaction length, l_{eff}, inferred from the width of the tuning curves.[38] With the tight focus used to generate the curves in Fig. 6, l_{eff} is limited by the confocal length of the beam. To determine the limit on l_{eff} due to inhomogeneities in the crystal, the tuning curves were remeasured using a 65-mm focal-length lens to focus the beam, resulting in a confocal length of 1.3 mm. In this case the FWHM of the two curves were 1.4 nm and 1.5 nm for d_{33} and d_{22}, respectively. Using the dispersion data of Ref. 29, $l_{eff} \approx 320$ μm was obtained for both d_{33} and d_{22}, corresponding to an effective number of domains $N \approx 240$. That the same effective length was obtained for both polarizations suggests that it is limited by variations in the domain spacing rather than by compositional inhomogeneities, as the latter generally affects the two indices of refraction differently.

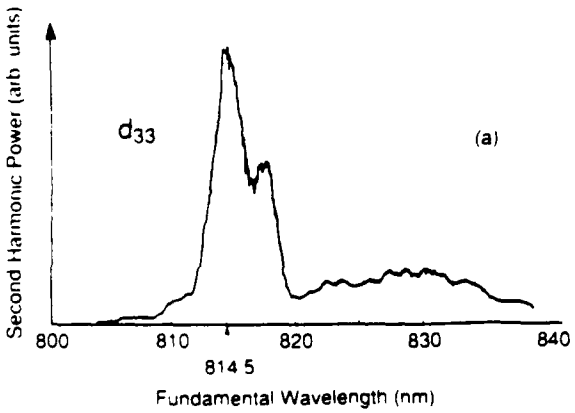

Fig.6(a). Second harmonic power vs fundamental wavelength, for extraordinary polarization, focusing with 5× objective.

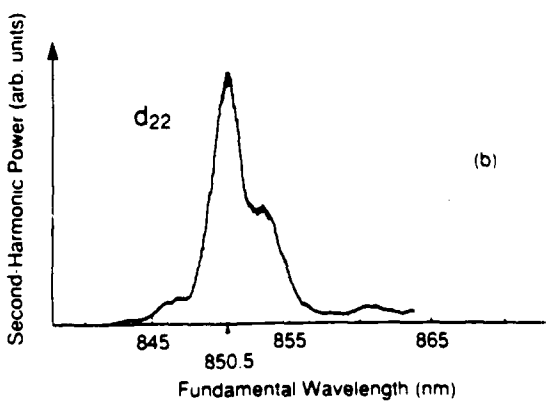

Fig. 6(b). Same as (a), except ordinary polarization.

According to Eq. (4), the accumulated error in the position of the Nth domain is approximately $\Lambda/2 \approx 1.3$ μm, a magnitude not unlikely given the slippage in the friction-coupled belt-drive system, designed to pull long continuous lengths of fiber for other applications, used to translate the lithium niobate fibers during growth.

The theoretical conversion efficiency was calculated using $d_{eff} = 22$ pm/V, obtained from Eq. (2) and the value for d_{33} from Ref. 7, and $l_{eff} = 320$ μm. The conversion efficiency for the measurement with the 65-mm lens agreed within 20% with this calculation. With the 5× objective, close to the optimum focusing for this effective length, as much as 7 μW of blue light was generated with 83 mW of input at the fundamental. The normalized theoretical conversion efficiency for an optimally-focused interaction using d_{33} and QPM is 5.2%/W-cm, 13.5 times larger than would be obtained for a birefringently phase-matched interaction using d_{31} (were it possible to phase-match).

Photorefractive damage is an important consideration for applications of lithium niobate involving visible radiation.[39] In lithium niobate, a bulk photovoltaic effect is responsible for the charge separation that leads to the changes in the index of refraction that cause the light scattering. The sign of this current changes in antiparallel domains, so one would expect the photorefractive effect to be substantially altered in periodically-poled crystals. To test this supposition, we compared the photorefractive response of an ≈ 2 mm long, undoped x-grown periodically-poled sample with $\Lambda = 3$ μm against that of an identically-prepared uniformly-poled sample. 488-nm radiation from an argon laser was polarized along the z-axis and focussed to a 12-μm diameter spot inside the sample. An adjustable slit, oriented so that photorefractive beam spreading along the z-axis would reduce the proportion of the beam transmitted, was centered in the far-field of the transmitted beam at a very low input power and adjusted to block approximately half the total power. The power was then increased, and the time-dependent throughput of the slit was recorded. The results depended on the power of the input beam; typically an initial rapid (100 ms – 10 s) decrease in throughput was followed by a slow recovery (10 s – 10 min) to a level somewhat below the original low-power value. For the uniformly poled sample with 100 mW incident power, the fraction passed by the slit dropped to less than 40% of the low power value in 100 ms. Under the same conditions, no significant reduction in the throughput was seen with the periodically-poled sample. As is typical of photorefractive phenomena, the behavior was a complicated function of input power, thermochemical history of the samples, etc., so more studies are necessary to properly characterize the effect. However, the present data support the hypothesis that the optically-induced changes in the index of refraction are dramatically altered by the domain reversal, and suggest that periodically-poled lithium niobate can support useful intensities of blue light at room temperature.

In future work, the crystals will be pulled with precision linear stages to improve the uniformity of the domain structures and thus increase the effective length of the crystal. Assuming losses comparable to bulk crystals, even the present periodically-poled crystals are adequate to produce milliwatts of blue power from commercially available diode lasers if used in resonantly-enhanced SHG devices.[1,2] Samples are currently being prepared for use in intracavity second harmonic generation in a 946-nm Nd:YAG laser. Further characterization and modeling of the photorefractive effect in perodically-poled crystals are also of interest.

5. CONCLUSIONS

Periodically-poled lithium niobate can be engineered to quasi-phase-match any nonlinear interaction within the transparency range of the the crystal at any desired temperature, using any nonlinear coefficient. Control over the phase-matching makes this readily-available crystal applicable to a broad range of interactions. We have produced periodically-poled lithium niobate both by processing the surface of uniformly-poled wafers and through the growth of crystals containing volume gratings of domains. Domain structures with periods as small as 5 μm in the planar material and 2 μm in the bulk material have been produced. Quasi-phase-matched SHG of CW blue and green radiation has been demonstrated in planar and channel annealed proton-exchange waveguides with a normalized efficiency of 37%/W-cm^2, as

has SHG of blue light in the bulk samples. Photorefractive damage resistance at room temperature is dramatically increased in the periodically-poled crystals. Improved single-pass waveguide devices and resonant bulk interactions both appear capable of generating milliwatts of blue light from available laser diodes. Infrared generation by mixing near-infrared diodes is also possible.

6. ACKNOWLEDGMENTS

We are grateful to Crystal Technology, Inc. for providing the substrates, and to T. Carver, L. Goddard, and J. Vrhel for assistance in fabrication. This work was supported by the Air Force Office of Scientific Research, contract AFOSR-88-0354, the Joint Services Electronics Program, contract N00014-84-K-0327, and IBM corporation, contract 703211.

7. REFERENCES

1. W. J. Kozlovsky, C. D. Nabors, and R. L. Byer, "Efficient Second Harmonic Generation of a Diode-Laser-Pumped CW Nd:YAG Laser Using Monolithic MgO:$LiNbO_3$ External Resonant Cavities," *IEEE J. Quantum Electron.* **24**, pp. 913–919 (1988).

2. G. J. Dixon, C. E. Tanner, and C. E. Wieman, "432-nm Source Based on Efficient Second-Harmonic Generation of GaAlAs Diode-Laser Radiation in a Self-Locking External Resonant Cavity," *Opt. Lett.* **14**, pp. 731–733.

3. G. I. Stegeman and C. T. Seaton, "Nonlinear Integrated Optics," *J. Appl. Phys.* **58**, pp. R57–R78 (1985).

4. G. Tohmon, K. Yamamoto, and T. Taniuchi, "Blue Light Source Using Guided Wave Frequency Doubler With a Diode Laser," *Proc. SPIE* **898**, pp. 70–75 (1988).

5. J. A. Armstrong, N. Bloembergen, J. Ducuing, and P. S. Pershan, "Interaction Between Lightwaves in a Nonlinear Dielectric," *Phys. Rev.* **127**, pp. 1918–1939 (1962).

6. K. C. Rustagi, S. C. Mehendale, and S. Meenakshi, "Optical Frequency Conversion in Quasi-Phase-Matched Stacks of Nonlinear Crystals," *IEEE J. Quantum Electron.*, **QE-18**, pp. 1029–1041 (1982).

7. S. K. Kurtz, J. Jerphagnon, and M. M. Choy, "Nonlinear Dielectric Susceptibilities," in *Landolt-Börnstein, New Series*, edited by K.-H. Hellwege (Springer-Verlag, Berlin, 1979), Vol. 11, p. 682.

8. M. M. Fejer, "Single Crystal Fibers: Growth Dynamics and Nonlinear Optical Applications," Ph.D. dissertation, Stanford University, Stanford, CA (1986).

9. A. Szilagyi, A. Hordvik, and H. Schlossberg, "A Quasi-Phase-Matching Technique for Efficient Optical Mixing and Frequency Doubling," *J. Appl Phys.* **47**, pp. 2025–2032 (1976).

10. D. E. Thompson , J. D. McMullen, and D. B. Anderson, "Second-Harmonic Generation in GaAs 'Stack of Plates' Using High-Power CO_2 Laser Radiation," *Appl. Phys. Lett.* **29**, pp. 113–115 (1976).

11. C. F. Dewey Jr. and L. O. Hocker, "Enhanced Nonlinear Optical Effects in Rotationally Twinned Crystals," *Appl. Phys. Lett.* **26**, 442–444 (1975).

12. G. Khanarian, D. Haas, R. Keosian, D. Karim, and P. Landi, "Phase Matched Second Harmonic Generation in a Polymeric Waveguide," paper ThB1, Conference on Lasers and Electro-Optics, Baltimore, MD, April 24-28, 1989.

13. R. C. Miller, "Optical Harmonic Generation in Single Crystal $BaTiO_3$," *Phys. Rev.* **134**, pp. A1313–A1319 (1964).

14. A. Räuber, "Chemistry and Physics of Lithium Niobate," in *Current Topics in Materials Science*, Vol. 1, edited by E. Kaldis (North-Holland, Amsterdam, 1978), pp. 481–601

15. A. Feisst and P. Koidl, "Current Induced Periodic Ferroelectric Domain Structures in $LiNbO_3$ Applied for Efficient Nonlinear Optical Frequency Mixing," *Appl. Phys. Lett.* **47**, pp. 1125–1127 (1985).

16. N. B. Ming, J. F. Hong, and D. Feng, "The Growth Striations and Ferroelectric Domain Structures in Czochralski-Grown $LiNbO_3$ Single Crystals," *J. Mater. Sci.* **17**, pp. 1663–1670 (1982).

17. K. Nakamura and H. Shimizu, "Poling of Ferroelectric Crystals by Using Interdigital Electrodes and its Application to Bulk-Wave Transducers," *1983 IEEE Ultrasonics Symp. Proc.*, pp. 527–530 (1983).

18. K. Nakamura, H. Ando, and H. Shimizu, "Ferroelectric Domain Inversion Caused in $LiNbO_3$ Plates by Heat Treatment," *Appl. Phys. Lett.* **50**, pp. 1413–1414 (1987).

19. Y. S. Luh, R. S. Feigelson, M. M. Fejer, and R. L. Byer, "Ferroelectric Domain Structures in $LiNbO_3$ Single-Crystal Fibers,"*J. Cryst. Growth* **78**, pp. 135–143 (1986).

20. J. R. Carruthers, G. E. Peterson, M. Grasso, and P. M. Bridenbaugh, "Nonstoichiometry and Crystal Growth of Lithium Niobate," *J. Appl. Phys.* **42**, 1846–1851 (1971).

21. E. J. Lim and M. M. Fejer, "Effects of Lithium Outdiffusion on Ferroelectric Domains in Lithium Niobate," in preparation for *Appl. Phys. Lett.*

22. J. Webjörn, F. Laurell, and G. Arvidsson, "Blue Light Generated by Frequency Doubling of Laser Diode Light in a Lithium Niobate Channel Waveguide," *IEEE Photonics Technology Letters* **1**, to be published October 1989.

23. S. Miyazawa, "Ferroelectric Domain Inversion in Ti-indiffused $LiNbO_3$ Optical Waveguide," *J. Appl. Phys.* **50**, pp. 4599–4603 (1979).

24. S. Thaniyavarn, T. Findakly, D. Booher, and J. Moen, "Domain Inversion Effects in Ti-$LiNbO_3$ Integrated Optic Devices," *Appl. Phys. Lett.* **46**, pp. 933–935 (1985).

25. S. K. Korotky and R. C. Alferness, "Ti:$LiNbO_3$ Integrated Optic Technology," in Integrated Optical Circuits and Components, Design and Applications, L. D. Hutcheson, ed., pp. 169–227, Marcel Dekker, Inc., New York, (1987).

26. P. G. Suchoski, T. K. Findakly, and F. J. Leonberger, "Stable low-loss proton-exchanged $LiNbO_3$ waveguide devices with no electro-optic degradation," *Opt. Lett.* **13**, pp. 1050–1052 (1988).

27. E. J. Lim, M. M. Fejer, and R. L. Byer, "Second Harmonic Generation of Green Light in Periodically Poled Planar Lithium Niobate Waveguide,"*Electron. Lett.* **25**, pp. 174–175 (1989).

28. E. J. Lim, M. M. Fejer, and R. L. Byer, "Blue Light Generation by Frequency Doubling in Periodically Poled Lithium Niobate Channel Waveguide," *Electron. Lett.* **25**, pp. 731–732 (1989).

29. G. J. Edwards and M. Lawrence, "A Temperature-Dependent Dispersion Equation for Congruently Grown Lithium Niobate," *Optical and Quantum Electronics* **16**, pp. 373–375 (1984).

30. R. C. Miller, "Optical Harmonic Generation in Single Crystal $BaTiO_3$," *Phys. Rev.* **134**, pp. A1313–A1319 (1964).

31. B. S. Red'kin, V. N. Kurlov, and V. A. Tatarchenko, "The Stepanov Growth of $LiNbO_3$ Crystals," *J. Cryst. Growth* **82**, pp. 106–109 (1987).

32. V. V. Antipov, A. A. Blistanov, N. G. Sorokin, and S. I. Chizhikov, "Formation of Regular Domain Structure in the Ferroelectrics $LiNbO_3$ and $LiTaO_3$ Near the Phase Transition," *Sov. Phys. Crystallogr.* **30**, pp. 428–430 (1985).

33. Y. H. Xue, N. B. Ming, J. S. Zhu, and D. Feng, "The Second Harmonic Generation in $LiNbO_3$ Crystals with Periodic Laminar Ferroelectric Domains," *Chinese Phys.* **4**, pp. 554–564 (1983).

34. G. A. Magel, M. M. Fejer, and R. L. Byer, "Quasi-Phase-Matched Second Harmonic Generation of Blue Light in Periodically-Poled $LiNbO_3$," submitted to *Appl. Phys. Lett.*

35. M. M. Fejer, J. L. Nightingale, G. A. Magel, and R. L. Byer, "Laser-Heated Miniature Pedestal Growth Apparatus for Single-Crystal Optical Fibers," *Rev. Sci. Instrum.* **55**, pp. 1791–1796 (1984).

36. The source rods for the congruent and the Mg-doped samples were cut from integrated optic substrates and nominally 5% Mg-doped $LiNbO_3$, respectively. Both were obtained from Crystal Technology, Inc., Palo Alto, CA.

37. J. Chen, Q. Zhou, J. F. Hong, W. S. Wang, N. B. Ming, D. Feng, and C. G. Fang, "Influence of Growth Striations on Para-Ferroelectric Phase Transitions: Mechanism of the Formation of Periodic Laminar Domains in $LiNbO_3$ and $LiTaO_3$," *J. Appl. Phys.* **66**, pp. 336–341 (1989).

38. S. Blit, E. G. Weaver, and F. K. Tittel, "Wavelength Temperature and Angle Bandwidths in SHG of Focused Beams in Nonlinear Crystals," *Appl. Opt.* **18**, pp. 733–736 (1979); F. R. Nash, G. D. Boyd, M. Sargent III, and P. M. Bridenbaugh, "Effect of Optical Inhomogeneities on Phase Matching in Nonlinear Crystals,"*J. Appl. Phys.* **41**, pp. 2564–2576 (1970). [These results had to be slightly modified for evaluating QPM spectral bandwidths.]

39. A. M. Glass, "The Photorefractive Effect," *Opt. Eng.* **17**, pp. 470–479 (1978).

Quasi-phase-matched second-harmonic generation of blue light in periodically poled $LiNbO_3$

G. A. Magel, M. M. Fejer, and R. L. Byer
Edward L. Ginzton Laboratory, Stanford University, Stanford, California 94305

(Received 24 August 1989; accepted for publication 31 October 1989)

$LiNbO_3$ crystals with periodically alternating ferroelectric domains have been produced using laser-heated pedestal growth. Domain thicknesses as small as 1 μm have been achieved. This material was applied to room-temperature, quasi-phase-matched frequency doubling tc generate light at wavelengths as short as 407 nm, using the d_{33} and d_{22} nonlinear coefficients. The measured conversion efficiencies and wavelength and temperature tuning bandwidths are consistent with an effective interaction length of $\approx 320\,\mu$m (> 230 domains). An initial test with high-intensity focused blue beams showed that the periodically poled material exhibits no discernible photorefractive damage effect.

Materials with high nonlinearity, good optical quality, and the ability to phase match for direct frequency doubling of GaAlAs diode lasers are in demand for the development of compact sources of short-wavelength light to be used in optical storage and other applications. Lithium niobate ($LiNbO_3$) has insufficient birefringence to use conventional phase-matching techniques at these wavelengths. We have demonstrated the capability of growing periodic ferroelectric domain structures of high spatial frequency in $LiNbO_3$. Using quasi-phase-matching in this material, we have accomplished collinear cw second-harmonic generation (SHG) with wavelengths and nonlinear coefficients which would have been impossible to phase match using only the material birefringence.

Quasi-phase-matching (QPM) was the first technique to be suggested for compensating refractive-index dispersion to obtain efficient SHG.[1] In this technique, the nonlinear coefficient is modulated spatially with a period $\Lambda = 2ml_c$, where $m = 1,3,5...$ is the "order" of QPM and l_c is the coherence length, given by

$$l_c = \lambda/4(n_2 - n_1), \tag{1}$$

where λ is the fundamental wavelength, and n_1 and n_2 are the refractive indices at the fundamental and second-harmonic wavelengths, respectively. The condition for QPM is

$$\mathbf{k}_2 - 2\mathbf{k}_1 - \mathbf{K} = 0, \tag{2}$$

where $\mathbf{K}$ is the wave vector of the nonlinear coefficient grating, having the magnitude $K = 2m\pi/\Lambda$, and $\mathbf{k}_1$ and $\mathbf{k}_2$ are the wave vectors for the fundamental and second-harmonic waves. The effective nonlinear coefficient is determined by the amplitude of the pertinent spatial-frequency component of the periodic structure. If the modulation consists of alternating the sign of the nonlinear coefficient d_{ij} at equal intervals, then

$$d_{\text{eff}} = (2/m\pi)d_{ij}. \tag{3}$$

It is thus desirable to use the lowest-order QPM possible, where $m = 1$ and $\Lambda = 2l_c$, in order to obtain the highest conversion efficiency, which is proportional to d_{eff}^2. In $LiNbO_3$, the sign of the nonlinear coefficient can be reversed either by rotating a slice of the crystal through 180° around the x axis, or by creating an oppositely polarized ferroelectric domain, which is crystallographically equivalent to this rotation. Quasi-phase-matched SHG in $LiNbO_3$ has been previously demonstrated in Czochralski-grown periodically poled $LiNbO_3$ at $\lambda = 1.06\,\mu$m, for which $l_c = 3.4\,\mu$m,[2] and, more recently, using periodically reversed domains in an integrated-optic geometry.[3]

Small-diameter single crystals of $LiNbO_3$ are produced by laser-heated pedestal growth using the apparatus described in Ref. 4. In this technique, 10.6 μm radiation from a CO_2 laser is focused on the tip of a typically 500-μm-diam single-crystal source rod of $LiNbO_3$ to make a small molten droplet into which a seed crystal is dipped. The seed, which determines the growth orientation, is then withdrawn from the droplet as fresh source material is supplied; the ratio of the pull rate to the feed rate determines the average diameter of the growing crystal, which in these experiments was approximately 250 μm. Crystals are grown either in air or in a 4:1 mixture of helium and oxygen. Periodically reversed ferroelectric domains with boundaries following the growth interface shape, as shown in Fig. 1, are created during growth by modulating the freezing interface position, either by ro-

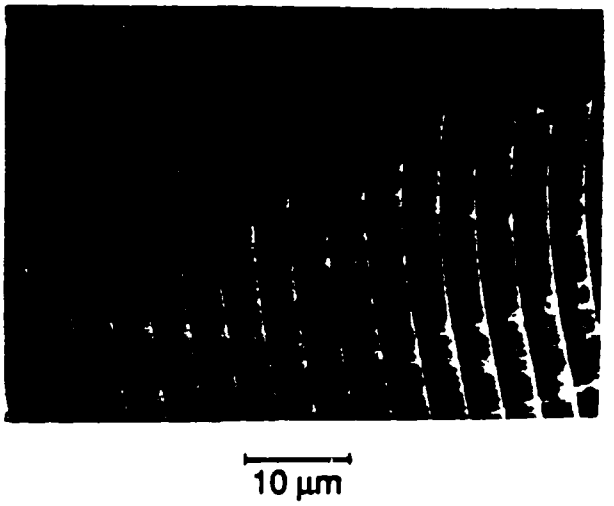

FIG. 1. SEM photograph showing periodically alternating domains with period ~3.5 μm as revealed by polishing and etching the y face of a pedestal-grown crystal. The crystal pull direction (along the x axis) is to the right in the photograph. The curvature of the domains is due to the convex shape of the growth interface. Straight lines are scratches from polishing

 0003-6951/90/020108-03$02.00

tating an asymmetric heat input produced by a rotating mask or by periodically modulating the heating power. The period of the domain structure in μm is given by $\Lambda = v_{pull}/f_{mod}$, where v_{pull} is the crystal pull rate in μm/s and f_{mod} is the frequency of modulation in Hz. Using these techniques, we have grown domain structures with periods as small as 2 μm, in either nominally 5% Mg-doped or undoped congruent material, and in crystals grown along either the x or z axis.

Modulation of the position of the freezing interface corresponds to a modulation of the microscopic growth rate at the interface. Components or dopants with an effective segregation coefficient $k_{eff} \neq 1$ are, as a result, incorporated into the growing crystal with a periodically varying concentration.[5] Sections of the length of the growing crystal with composition gradients of the correct sign and sufficient magnitude to overcome steady-state self-generated poling fields[6] form reversed ferroelectric domains. The mechanisms through which composition gradients influence the domain formation is a topic of current research.[7] The large axial temperature gradients and high growth rates present during laser-heated pedestal growth, together with the high Curie temperature of the material, aid in the formation of well-defined domain walls near the freezing interface.

The sample used in the optical experiments was a Mg-doped[8] x-axis $LiNbO_3$ crystal approximately 250 μm in diameter, grown at a pull rate of $v_{pull} = 2$ mm/min. The heat input was modulated using a periodically triggered electromechanical shutter with $f_{mod} = 12.35$ Hz, resulting in a domain structure of period $\Lambda = 2.7$ μm. This period was picked so that SHG using either the d_{33} or d_{22} nonlinear coefficient could be first-order quasi-phase-matched within the wavelength tuning range of a cw Styryl-9 dye laser. After annealing in flowing dry O_2 for 3 h at 725 °C to increase the crystal transparency without erasing the periodic domain structure, the sample was glued into a 2 mm length of glass capillary tubing and polished on the x faces to a length of 1.77 mm.

Figure 2 shows phase-matching curves obtained by plotting the second-harmonic power while scanning the dye laser wavelength λ. The d_{33} nonlinear coefficient was addressed by polarizing the x-propagating fundamental wave linearly along the crystal z axis; then, without moving the sample, the d_{22} coefficient was addressed by rotating the polarization 90° so that it was parallel to the y axis. The similarity of the shapes of these two curves suggests that phase matching occurs in the same region of the sample, and that both n_e (d_{33}) and n_o (d_{22}) have similar optical quality, in spite of the many domain walls and the modulated composition. We confirmed that the generated second-harmonic wave has the same polarization as the fundamental wave for both these coefficients. QPM occurred at $\lambda = 814.5$ nm for d_{33} and at 850.5 nm for d_{22}. The effective interaction length l_{eff} inferred from the width of these tuning curves[9] is limited by the depth of focus of the 5× microscope objective (focal length ≈ 30 mm) used to obtain them.

To determine l_{eff} as limited by the uniformity of the periodicity of the domain structure, the 5× objective was replaced by a 65 mm focal length lens. With this lens, the

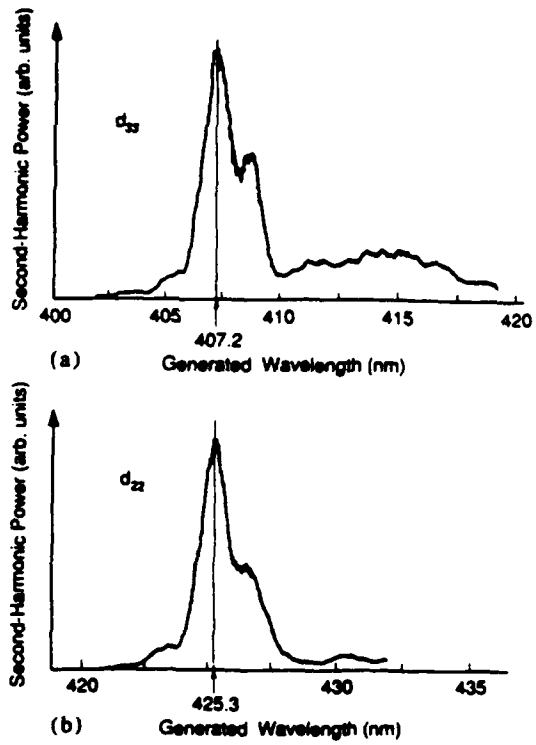

FIG. 2. Second-harmonic power vs wavelength tuning curves obtained with 5× microscope objective for (a) d_{33} and (b) d_{22}.

confocal parameter of the fundamental beam within the crystal was 1.3 mm. The width of the d_{33} and d_{22} wavelength-tuning curves indicated an $l_{eff} \approx 320$ μm. Temperature-tuned phase-matching curves for both the nonlinear coefficients were also obtained by placing the sample in a heated mount. The temperature-tuned widths were found to be consistent with the above l_{eff} when values for dn/dT from Ref. 10 were used. We conclude that in this sample the effective length is due to the nonuniformity of the domain periods, since it is significantly shorter than both the overall length of the sample and the confocal parameter of the fundamental beam.

The theoretical conversion efficiency for d_{33} interaction was calculated using $l_{eff} = 320$ μm and $d_{eff} = 22$ pm/V, obtained by inserting $m = 1$ and the value for d_{33} tabulated by Kurtz *et al.*[11] into Eq. (3). The conversion efficiency measured using the 65 mm lens agreed with this calculation within 20%. Using the 5× lens, which produced nearly optimal focusing, we measured a maximum conversion efficiency, corrected for Fresnel reflection at the crystal faces, of 8×10^{-5}. This efficiency was obtained with 83 mW of input fundamental power and 6.7 μW of blue light generated within the crystal. The second-harmonic power was quadratic with input power over the entire range measured. The normalized theoretical conversion efficiency using d_{33} and QPM with optimal focusing is calculated to be 0.52% W^{-1} mm^{-1}, or 13.5 times that which would be obtained were it possible to birefringently phase match a d_{31} interaction at this wavelength.

It was surmised that the photorefractive properties of the periodically poled material might be altered by the rapid-

ly alternating sign of charge transport or by fields present at the many domain walls. This question is of great importance in applications of $LiNbO_3$ at visible wavelengths. No photorefractive effect was observed in periodically poled Mg-doped or undoped $LiNbO_3$ with the relatively low levels of blue light generated in the SHG experiments. Therefore, a separate experiment was performed to compare an undoped periodically poled sample with $\Lambda = 3\ \mu m$ against an identically processed undoped uniformly poled sample. In this experiment, extraordinarily polarized 488 nm light from an argon-ion laser, propagating along the x axis, was focused to a beam waist of radius $w = 6\ \mu m$ in the sample. A slit was centered in the transmitted beam and adjusted at very low power ($\sim 3\ \mu W$) to block approximately half of the light. The slit was oriented so that beam spreading along the z axis, characteristic of the photorefractive effect,[12] would reduce the proportion of light transmitted by the slit. When the incident power was stepped up to 100 mW in the uniformly poled material, the fraction passed by the slit dropped to 37% of the low-power value in < 100 ms. In contrast, at the same power level in the periodically poled material, the transmitted fraction stayed at 100% of the low-power value, with no sign of change for measurement intervals of several minutes. After the test, the uniformly poled sample exhibited spots of persistently changed refractive index where it had been exposed to the blue beam, whereas there were no such marks in the periodically poled sample. These results indicate that periodically poled $LiNbO_3$ grown and processed by our methods should be useful for interactions involving hundreds of milliwatts of visible light.

Periodically poled $LiNbO_3$ can be engineered to quasi-phase-match nonlinear interactions at any desired temperature, using any nonlinear coefficient, and involving any wavelengths within the transparency range of the crystal. This control over its phase-matching properties makes the already important material $LiNbO_3$ potentially applicable to a much wider variety of interactions. The material is easy to grow and the domain structure is stable to at least several hundred degrees Celsius.

In future work, the uniformity of the domain-structure periodicity may be improved, and hence the effective interaction length increased, by upgrading the translators in the crystal puller to achieve better velocity stability. Other nonlinear interactions utilizing QPM will be investigated, as well as the use of resonantly enhanced SHG[13] to obtain milliwatts of blue light at input power levels available from laser diodes.

In summary, we have grown periodically poled $LiNbO_3$ with domains as thin as 1 μm using the laser-heated pedestal growth method. This material was used to demonstrate room-temperature, cw, quasi-phase-matched SHG using either the d_{33} or d_{22} nonlinear coefficients, at wavelengths as short as 407 nm. The measured conversion efficiencies and wavelength and temperature tuning bandwidths are all consistent with an effective phase-matched interaction length of $\approx 320\ \mu m$ (> 230 domains). An initial test with high-intensity focused blue beams showed that the periodically poled material exhibits no discernible photorefractive effect.

We would like to thank Professor H. J. Shaw and Professor B. Y. Kim for the use of their dye laser, and Crystal Technology, Inc. for supplying source material. This work was supported by the Air Force Office of Scientific Research, the Joint Services Electronics Program, and the IBM Corp. G. A. Magel gratefully acknowledges the past support of the Fannie and John Hertz Foundation.

[1] J. A. Armstrong, N. Bloembergen, J. Ducuing, and P. S. Pershan, Phys. Rev. 127, 1918 (1962); N. Bloembergen, U.S. Patent No. 3 384 433 (1968).
[2] Y. H. Xue, N. B. Ming, J. S. Zhu, and D. Feng, Chin. Phys. 4, 554 (1983); A. Feisst and P. Koidl, Appl. Phys. Lett. 47, 1125 (1985).
[3] E. J. Lim, M. M. Fejer, R. L. Byer, and W. J. Kozlovsky, Electron. Lett. 25, 731 (1989); J. Webjörn, F. Laurell, and G. Arvidsson, paper ThA2, Topical Meeting on Nonlinear Guided-Wave Phenomena, Houston, TX, February 2–4, 1989.
[4] M. M. Fejer, J. L. Nightingale, G. A. Magel, and R. L. Byer, Rev. Sci. Instrum. 55, 1791 (1984).
[5] N. B. Ming, J. F. Hong, and D. Feng, J. Mater. Sci. 17, 1663 (1982).
[6] Y. S. Luh, R. S. Feigelson, M. M. Fejer, and R. L. Byer, J. Cryst. Growth 78, 135 (1986).
[7] See, for example, J. Chen, Q. Zhou, J. F. Hong, W. S. Wang, N. B. Ming, D. Feng, and C. G. Fang, J. Appl. Phys. 66, 336 (1989).
[8] The source material was nominally 5% Mg-doped $LiNbO_3$ obtained from Crystal Technology, Inc., Palo Alto, CA.
[9] S. Blit, E. G. Weaver, and F. K. Tittel, Appl. Opt. 18, 733 (1979); F. R. Nash, G. D. Boyd, M. Sargent III, and P. M. Bridenbaugh, J. Appl. Phys. 41, 2564 (1970). (These results had to be slightly modified for evaluating QPM spectral bandwidths.)
[10] D. H. Jundt, M. M. Fejer, and R. L. Byer, IEEE J. Quantum Electron. 26, 135 (1990). (We used the Sellmeier coefficients for stoichiometric $LiNbO_3$ from this reference because previously published fits for congruent $LiNbO_3$ cannot be accurately extrapolated to blue wavelengths.)
[11] S. K. Kurtz, J. Jerphagnon, and M. M. Choy, "Nonlinear Dielectric Susceptibilities," in *Landolt-Börnstein, New Series*, edited by K.-H. Hellwege (Springer, Berlin, 1979), Vol. 11, p. 682.
[12] A. Ashkin, G. D. Boyd, J. M. Dziedzic, R. G. Smith, A. A. Ballman, J. J. Levinstein, and K. Nassau, Appl. Phys. Lett. 9, 72 (1966).
[13] W. J. Kozlovsky, C. D. Nabors, and R. L. Byer, IEEE J. Quantum Electron. 24, 913 (1988).

Observation of Extremely Large Quadratic Susceptibility at 9.6–10.8 μm in Electric-Field-Biased AlGaAs Quantum Wells

M. M. Fejer, S. J. B. Yoo, and R. L. Byer
Edward L. Ginzton Laboratory, Stanford University, Stanford, California 94305

Alex Harwit[a] and J. S. Harris, Jr.
Stanford Electronics Laboratory, Stanford University, Stanford, California 94305
(Received 28 December 1988)

We have observed an extremely large second-order susceptibility for second-harmonic generation of 9.6–10.8-μm radiation due to intersubband transitions in electric-field-biased GaAs quantum wells. For 92-Å GaAs wells with 309-Å $Al_{0.48}Ga_{0.52}As$ barriers under a bias of 36 kV/cm, the peak value of the susceptibility was 28 nm/V, 73 times larger than for bulk GaAs. The magnitude and sign of the susceptibility depend on the bias field, and are in accord with theoretical predictions.

PACS numbers: 42.65.Ky, 73.20.Dx, 78.65.Fa

Transitions between the subbands of an isolated quantum well have extremely large oscillator strengths.[1] Strong infrared absorption features associated with transitions between the lowest two subbands in a GaAs quantum well have been observed by several groups.[1-3] Since nth-order nonlinear susceptibilities are proportional to the product of $n+1$ dipole matrix elements, strong nonlinear effects can also be expected.[4-7] As even-order susceptibilities vanish in structures with inversion symmetry, finite second-order susceptibilities can only be observed if the symmetry of the conduction-band potential is broken through either the growth of an asymmetric well or the application of an external bias field. We report here on the first measurement of the second-order susceptibility of a quantum well biased with an external field. The measurements of electric-field-induced second-harmonic generation of the 9.6–10.8-μm output of a CO_2 laser in modulation-doped AlGaAs quantum wells are in accord with theoretical predictions.

To calculate the nonlinear susceptibilities, we need the energy eigenvalues and dipole matrix elements for an electron in a quantum well under an applied electric field. The wave function is the product of a Bloch function, a plane wave in the plane normal to the layers ($\perp\hat{z}$), and an envelope function ψ that depends only on z. Assuming vertical transitions between the subbands and unity overlap of the Bloch functions,[1] we need only consider the dipole matrix elements and energies of the envelope functions. The expression for the nonlinear polarizability for second-harmonic generation $\alpha^{(2)}$ is then the same as that given in Ref. 8 for transitions between discrete states,

$$\alpha_{33}^{(2)}=\frac{2e^3}{\epsilon_0\hbar^2}\sum_{mn}\langle z_{1n}\rangle\langle z_{nm}\rangle\langle z_{m1}\rangle\{[(\omega-\Omega_{n1}-i\gamma_{n1})(2\omega-\Omega_{m1}-i\gamma_{m1})]^{-1}+[(\omega+\Omega_{n1}-i\gamma_{n1})(2\omega+\Omega_{m1}-i\gamma_{m1})]^{-1}$$
$$-(2\omega-\Omega_{mn}-i\gamma_{mn})^{-1}[(\omega-\Omega_{m1}-i\gamma_{m1})^{-1}+(\omega+\Omega_{n1}-i\gamma_{n1})^{-1}]\}, \quad (1)$$

where $\langle z_{ij}\rangle=\langle\psi_i|z|\psi_j\rangle$, $\Omega_{ij}=(E_i-E_j)/\hbar$, $1/\gamma_{ij}$ is the dephasing time, and e is the magnitude of the electronic charge. We have assumed that only the lowest subband is thermally populated. In the low-density limit, the nonlinear susceptibility $\chi^{(2)}$ is given by $\chi^{(2)}=N\alpha^{(2)}$, where N is the number density of conduction electrons. Since at least one of the matrix elements in each term vanishes if the states are of definite parity, the magnitude of the nonlinearity depends strongly on those matrix elements, forbidden at zero field, that are induced by the bias field.

For a well of depth U_0 and width L centered at $z=0$, under a bias electric field $F\hat{z}$ normal to the well, the envelope function ψ_n obeys $H(z)\psi_n=E_n\psi_n$, where we take the effective-mass Hamiltonian to be

$$H(z)=-\frac{\hbar^2}{2}\frac{d}{dz}\frac{1}{m(z)}\frac{d}{dz}+U(z)+eFz. \quad (2)$$

For $|z|<L/2$, $U(z)=0$ and the effective mass $m_e(z)=m_w$, while for $|z|>L/2$, $U(z)=U_0$ and $m_e(z)=m_b$. While the Schrödinger equation obtained with this Hamiltonian is readily solved numerically, insight into the effects of the bias field on the optical properties of the system can be obtained from an approximate solution of the infinite-well ($U_0\to\infty$) model. For this analysis, it is useful to introduce a characteristic confinement energy,

$E_0 \equiv \pi^2\hbar^2/2m_w L^2$, and a dimensionless measure of the strength of the bias field, $\Phi \equiv eFL/\pi E_0$. For the range of bias fields applied in this experiment, it is adequate to treat the electric field as a perturbation. In this case, we can obtain wave functions correct to first order in Φ[9]:

$$\psi_n(z) = \left[\frac{2}{L}\right]^{1/2}\left\{\cos(n\zeta) + \frac{\Phi}{4n}\left[(-1)^n\left(\frac{\pi^2}{4} - \zeta^2\right)\sin(n\zeta) + \frac{\zeta}{n}\cos(n\zeta)\right]\right\} \quad (3)$$

for n odd, and the same expression with cos and sin interchanged for n even. $\zeta \equiv \pi z/L$ is a dimensionless length. The energy eigenvalues accurate to second order in Φ are

$$\frac{E_n}{E_0} = n^2 + \Phi^2\frac{\pi^2}{48n^2}\left[1 - \frac{15}{\pi^2 n^2}\right]. \quad (4)$$

The dipole matrix elements are necessary for the calculation of the optical properties of the quantum well. The allowed matrix elements in a symmetric square well, i.e., those between states of opposite parity, have been given previously as[1]

$$\frac{\langle z_{mn}\rangle}{L} = (-1)^{(n+m+1)/2}\frac{8}{\pi^2}\frac{mn}{(m^2-n^2)^2}, \quad (5)$$

where we have neglected a correction proportional to Φ^2. From Eq. (3) we can obtain the dipole matrix elements that are disallowed at zero field, i.e., those between states of the same parity: for $m = n$,

$$\frac{\langle z_{nn}\rangle}{L} = \Phi\frac{\pi^2 n^2 - 15}{24\pi n^4}; \quad (6a)$$

for m,n odd,

$$\frac{\langle z_{mn}\rangle}{L} = \Phi\frac{(-1)^{(n+m)/2}}{\pi}\frac{m^2+n^2}{nm(m^2-n^2)^2}, \quad (6b)$$

and the negative of the latter expression for m,n even. Despite the derivation of Eqs. (3) and (4) as expansions in powers of Φ, the dipole matrix elements calculated with Eqs. (5) and (6) agree to within several percent with numerical calculations for Φ on the order of 1 (fields of 200 kV/cm for a 92-Å GaAs well).[10]

For wells of finite depth, the wave function spreads into the barrier region, and the above analysis is no longer valid. For the purpose of discussion, it is adequate to use the effective-width approximation,[11] where we replace L in the expressions for the infinite well with L_e, where L_e is chosen to yield the correct ground-state energy for the finite well at zero bias. For a 92-Å GaAs well, with $Al_{0.48}Ga_{0.52}As$ barriers, we take the material parameters at 80 K to be $m_w = 0.067m_0$, $m_b = 0.107 \times m_0$,[12] the direct-bandgap energy $E_{g,w} = 1.507$ eV in the well[13] and $E_{g,b} = 2.163$ eV in the barrier,[12,14] and the conduction-band discontinuity as $0.63(E_{g,b} - E_{g,w})$.[15] With these parameters, we find that the ground-state energy of the unbiased well is 38 meV, resulting in an effective width of $L_e = 122$ Å. The quantities of interest for the calculation of optical properties can then be obtained by scaling the infinite-well results by $L_e/L = 1.32$. These scaled values, followed by the results from numerical solutions, are $E_1 = 38$ (38) meV, $E_2 = 152$ (152) meV, $E_3 = 342$ (332) meV, $\langle z_{12}\rangle = 22$ (22) Å, $\langle z_{23}\rangle = -24$ (−24) Å. For a bias field of 36 kV/cm, we find $\langle z_{13}\rangle = 0.74$ (0.74) Å, $\langle z_{11}\rangle - \langle z_{22}\rangle = -3.9$ (−3.7).

With Eqs. (5) and (6) for the dipole matrix elements and Eq. (4) for the eigenvalues, we can evaluate Eq. (1) for the nonlinear susceptibility. Consider a well with three bound states. The peak in the nonlinear susceptibility at $2\omega = \Omega_{31}$ ($\hbar\omega = 152$ meV for our example) is dominated by the $n = 2$, $m = 3$ term of Eq. (1). Considering only this term, we have with Eqs. (4) and (6)

$$\alpha^{(2)}(\omega = \Omega_{31}/2) \approx i\frac{1024}{45\pi^2}\frac{e^4}{\epsilon_0\hbar}\frac{F}{m_w^2\gamma_{31}\omega^4}. \quad (7)$$

Taking $N = 5\times10^{17}$ cm^{-3}, $\hbar\gamma_{13} = 7.5$ meV, and $F = 36$ kV/cm, we find $N\alpha^{(2)}(2\omega = \Omega_{31}) = 2.4\times10^{-8}$ m/V. For comparison, the nonlinear susceptibility of bulk GaAs, a highly nonlinear material, is $\chi_{14}^{(2)} = 3.8\times10^{-10}$ m/V.[16] From Eq. (7) it can be seen that the nonlinearity is inversely proportional to the square of the effective mass of electrons in GaAs, reflecting the fact that the size of a quantum well in resonance with a photon of a given energy increases with decreasing effective mass. The nonlinear susceptibility is also inversely proportional to the linewidth of the resonant transition. The magnitude of the discontinuity in the conduction band does not appear in the expression, as might be expected in the effective-width approximation. Finally, we note that the magnitude and sign of the nonlinear susceptibility are proportional to the applied bias field.

While the simple Hamiltonian in Eq. (2) is useful for a qualitative discussion of the nonlinear susceptibility, the nonparabolicity of the conduction band must be included in quantitative calculations.[17] We approximate the nonparabolicity with an energy-dependent effective mass defined by $\hbar^2k^2/2m(E) = E(k)$, chosen to agree with the quartic dispersion relation for GaAs given in Ref. 12. The reduction in the energy of the eigenstates caused by the nonparabolicity affects the magnitude of $\alpha^{(2)}$ both by shifting the location of the resonances, and by reducing the magnitude of the dipole matrix elements by reducing the barrier penetration of the wave functions. For our 92-Å example, E_3 shifts by 42 meV, significantly reducing the separation of Ω_{21} and $\Omega_{31}/2$, approximately doubling $\alpha^{(2)}(\omega = \Omega_{31}/2)$.

The magnitude of the intersubband nonlinearity can

be obtained experimentally from a measurement of electric-field-induced second-harmonic generation. We used a sample grown by molecular-beam epitaxy in a Varian Gen-II system. A 0.5-μm, $n=2\times10^{17}$-cm^{-3}-doped GaAs buffer layer followed by fifty periods of the superlattice was grown on a 500-μm, $n=7\times10^{16}$-cm^{-3}-doped substrate. A period of the superlattice consists of a 309-Å $Al_{0.48}Ga_{0.52}As$ barrier and a nominally 92-Å GaAs well. The center 132 Å of the barrier is doped at 6×10^{17} cm^{-3}, while the well is undoped. The structure is capped with a 1.3-μm GaAs layer, the first 500 Å of which is doped at 1×10^{18} cm^{-3}, the next 0.75 μm at 2×10^{17} cm^{-3}, and the top 0.5 μm at 2×10^{18} cm^{-3}. The dopant in all layers is silicon.

The sample was first characterized by infrared absorption measurements on a Digilab FTS-40 Fourier-transform infrared spectrometer. The wafer was oriented at Brewster's angle in a beam polarized in the plane of incidence. At 80 K an absorption line was observed at 112 meV with FWHM of 5 meV. The integrated absorption strength was 0.50 as large as predicted from the theoretical oscillator strength, which is accounted for in the remainder of the calculations by using a similarly reduced effective doping density. Measurements of the much weaker absorption of the 1-3 transition have not yet been obtained.

The transition energies and dipole matrix elements were calculated by numerical solution of Eq. (1) with a quartic dispersion relation, including a first-order perturbation calculation of the energy shift due to band bending. The macroscopic susceptibilities, related to the polarization $\mathcal{P}^{2\omega}$ by $\langle\mathcal{P}^{2\omega}\rangle=\chi^{(1)}\langle E^{2\omega}\rangle+\chi^{(2)}\langle E^{\omega}\rangle^2$, where the angular brackets indicate averaging over one period of the structure, were calculated in a self-consistent field approximation[18] carried out to second order in the applied fields. Many-body effects were neglected, and the numerical calculation was simplified by neglecting coupling of the different subband transitions. The major differences between this calculation and the simple result $\chi^{(2)}\approx Nf\alpha^{(2)}$, where f is the fraction of the structure filled by the quantum wells, are a blue shift of the resonances, and an overall reduction in the magnitude due to the difference between the bulk linear susceptibilities of the well and barrier. The magnitude of the second-order susceptibility for $F=36$ kV/cm, calculated with the empirical values for Ω_{21} and γ_{21}, the theoretical value for Ω_{31}, and $\hbar\gamma_{31}=7.5$ meV, is plotted versus fundamental frequency in Fig. 1.

The harmonic generation measurements were made with a grating-tuned, rotating-mirror, Q-switched CO_2 laser focused to a spot of approximately 50 μm diameter at the sample. The laser output was typically a train of 200-ns-long pulses with a peak power of 1 kW and a 100-Hz repetition rate. The bias voltage was applied every other laser pulse, and the second-harmonic output was monitored with a boxcar integrator operated in an active baseline-subtraction mode, so that only the portion

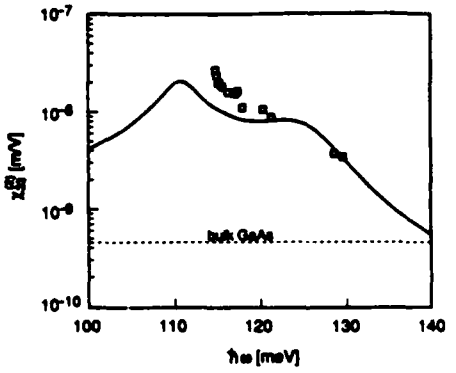

FIG. 1. Calculated nonlinear susceptibility for second-harmonic generation $\chi^{(2)}$ as a function of the energy of the fundamental photon. Squares are experimental measurements.

of the second-harmonic radiation that depended on the applied voltage was measured.

The total second-harmonic output is the coherent sum of the contributions from the quantum-well layer and the substrate. For a fundamental beam propagating at an angle θ to $\hat{z}$, it can be shown that the total second-harmonic power generated in the sample $P_{2\omega}$ is given by

$$P_{2\omega}\propto P_{\omega}^2\,|A\chi_{33}^{(2)}+B\chi_{14}^{(2)}[\cos(\theta)\phi-t\gamma]\,|^2, \qquad (8)$$

where A and B are possibly complex geometry-dependent factors, t is the ratio of the transmission coefficients for radiation polarized normal and parallel to the plane of incidence, and $\chi_{14}^{(2)}$ is the nonlinear susceptibility of bulk GaAs. ϕ, the angle between a [100] axis of the crystal and the intersection of the plane of incidence with the surface of the wafer, and γ, the angle between the fundamental electric field and the plane of incidence, are assumed to be small. As can be seen from Eq. (7), to first order $\chi_{33}^{(2)}$ is proportional to the applied bias field F. It is then clear from Eq. (8) that $P_{2\omega}$ is a quadratic function of the bias voltage V and that the minimum of the parabola shifts linearly with ϕ and γ.

$P_{2\omega}$ was measured for several wavelengths as a function of V at $\phi=\gamma=0$. The expected parabolic dependence is obeyed, with wavelength-dependent curvature reflecting the dispersion of $\chi_{33}^{(2)}$. The minima of the parabolas fall at $V=V_0\approx3$ V, rather that at $V=0$ as predicted by Eq. (8). That V_0 is the same for all the wavelengths suggests that the shift is a result of built-in asymmetry in the well, rather than misorientation of the sample or imperfect polarizers. We note that measurements of the quadratic Stark shift of the 1-2 transition showed a similar offset.[19] Repeating the measurement of $P_{2\omega}$ vs V for several values of γ at a fixed wavelength showed a linear dependence of V_0 on γ, as predicted by Eq. (8). For fundamental wavelengths close to the absorption peak, deviations from the parabolic dependence of $P_{2\omega}$ vs V, attributed to the Stark shift of the peak, were observed at high bias fields.

To extract an absolute value for $\chi_{33}^{(2)}$, $P_{2\omega}$ was normalized to the second-harmonic power generated at room temperature in a 110-μm-thick undoped GaAs plate mounted in the same apparatus. The connection of the second-harmonic generation in the quantum-well layer to the nonlinear susceptibility is complicated by the resonant birefringence and dichroism, and the subwavelength thickness of the layer.[20] The linear index of refraction data necessary for the calculation were estimated from a Lorentzian model fitted to the absorption spectrum. The experimental values for $\chi_{33}^{(2)}$ plotted in Fig. 1 are obtained at $F=36$ kV/cm. The agreement between the experimental data and the model is reasonable in view of the uncertainty in the device parameters and AlGaAs material properties, the unknown energy and linewidth of the 1-3 transition, and the neglect of many-body effects.

The largest value of $\chi^{(2)}$, measured at a fundamental wavelength of 10.8 μm, is 28 nm/V, 73 times larger than for bulk GaAs. This susceptibility is among the highest measured for any material, and is typical of the large second- and third-order effects, e.g., sum and difference frequency generation, electro-optic modulation, dc and optical Kerr effect, that can be expected in intersubband transitions. The control of the sign and magnitude of $\chi^{(2)}$ through the bias electric field suggests novel device geometries; e.g., a periodic bias electrode could be used to induce a periodic sign alternation in $\chi^{(2)}$ for quasi-phase-matching nonlinear interactions.[21] The utility of these nonlinearities for most optical devices, especially those involving nonlinear frequency conversion, will depend largely on the ratio of the pertinent nonlinearity to the absorption coefficients, which could be considerably improved by working in the vicinity of a weakly allowed transition well separated from the allowed transitions. More complete data on the absorption spectra and material parameters are necessary for the evaluation of the potential of these structures for device applications.

The authors thank Eric Hellman for many helpful discussions, and acknowledge the support of the Air Force Office of Scientific Research through Contract No. AFOSR-88-0354 and the Joint Services Electronics Program through Contract No. N00014-84-K-0327.

[a]Currently at IBM Thomas J. Watson Research Laboratory, Yorktown Heights, NY 10598.

[1]L. C. West and S. J. Eglash, Appl. Phys. Lett. **46**, 1156 (1985).

[2]B. F. Levine, R. J. Malik, J. Walker, K. K. Choi, C. G. Bethea, D. A. Kleinman, and J. M. Vandenberg, Appl. Phys. Lett. **50**, 273 (1987).

[3]Alex Harwit and J. S. Harris, Jr., Appl. Phys. Lett. **50**, 685 (1987).

[4]L. C. West, Ph.D. dissertation, Stanford University, 1985 (unpublished).

[5]M. K. Gurnick and T. A. DeTemple, IEEE J. Quantum Electron. **19**, 791 (1983).

[6]S. J. B. Yoo, M. M. Fejer, Alex Harwit, R. L. Byer, J. S. Harris, Jr., J. Opt. Sci. Am. A **4**, 27 (1987).

[7]L. Tsang, D. Ahn, and S. L. Chuang, Appl. Phys. Lett. **52**, 697 (1988).

[8]Y. R. Shen, *The principles of Nonlinear Optics* (Wiley, New York, 1984), Chap. 2.

[9]L. I. Schiff, *Quantum Mechanics* (McGraw-Hill, New York, 1968), p. 263.

[10]Note that by symmetry the only second-order correction to the dipole matrix elements between states of the same parity is in the normalization constant, which, to second order in Φ, is $(2/L)^{1/2}C_n$, where $C_n^{-2}\equiv 1+\Phi^2\frac{1}{360}n^{-6}(2\pi^4n^4+5\pi^2n^2-210)$.

[11]D. A. B. Miller, D. S. Chemla, T. C. Damen, A. C. Gossard, W. Weigmann, T. H. Wood, and C. A. Burrus, Phys. Rev. B **32**, 1043 (1985).

[12]S. Adachi, J. Appl. Phys. **58**, R1 (1985).

[13]J. S. Blakemore, J. Appl. Phys. **53**, R123 (1982).

[14]D. E. Aspnes, S. M. Kelso, R. A. Logan, and R. Bhat, J. Appl. Phys. **60**, 754 (1986).

[15]M. Nakayama, H. Kuwahara, H. Kato, and K. Kubota, Appl. Phys. Lett. **51**, 1741 (1987).

[16]*Handbook of Lasers*, edited by R. J. Pressley (Chemical Rubber Co., Cleveland, 1971), p. 504.

[17]T. Hiroshima and R. Lang, Appl. Phys. Lett. **49**, 456 (1986).

[18]S. J. Allen, Jr., D. C. Tsui, and B. Vinter, Solid State Commun. **20**, 425 (1976).

[19]Alex Harwit, Ph.D. dissertation, Stanford University, 1987 (unpublished).

[20]D. Chemla and P. Kupecek, Rev. Phys. Appl. **6**, 31 (1971).

[21]K. C. Rustagi, S. C. Mehandale, and S. Meenakshi, IEEE J. Quantum Electron. **18**, 1029 (1982).

Characterization of single-crystal sapphire fibers for optical power delivery systems

D. H. Jundt, M. M. Fejer, and R. L. Byer
Applied Physics Department, Stanford University, Stanford, California 94305

(Received 11 August 1989; accepted for publication 18 September 1989)

Sapphire single-crystal fibers with diameters of 110 μm and lengths of over 2 m have been grown by the laser-heated pedestal growth method. The fibers are free of imperfections such as voids and bubbles. The minimum loss of 0.5 dB/m was measured in the near infrared at 1064 nm. Absorption loss at 2936 nm was 0.88 dB/m with a damage threshold higher than 1.2 kJ/cm^2 for 110-μs-long pulses making tissue ablation feasible with fibers several meters in length.

Sapphire (α-Al_2O_3) has long been recognized as a good material for optical components due to its wide transparency range (240–4000 nm), high melting temperature (2053 °C), low solubility in water, and favorable mechanical and chemical properties. Sapphire single-crystal fibers are well suited for sensor applications in high temperature or chemically hostile environments,[1] as well as for use in medical power delivery systems operating at the 2936 nm Er:YAG wavelength[2] where silica glass fibers are highly absorbing.

In this letter we report on the optical properties of single-crystal sapphire fibers prepared with the laser-heated pedestal growth method (Fig. 1).[3] The fibers are grown by dipping an oriented single-crystal seed into a molten droplet produced above a feed rod[4] by CO_2 laser heating (Fig. 1). By carefully controlling the ratio of the speeds at which the source rod is pushed into and the fiber is pulled out of the molten zone, a reduction ratio of source rod to fiber diameter of 3.5 is typically obtained. A 6-cm-long, 0.4-mm-diam source rod generates a 70-cm-long, 110-μm-diam fiber. The sapphire fibers were typically grown in air at a speed of 4 mm/min. The cross section of the *c*-axis fibers is roughly circular with slight deviations reflecting the trigonal symmetry.

Longer fibers were grown by using a two-step reduction. A fiber grown from an 800-μm-diam source rod was used as the source material for a second step with a diameter reduction ratio of 3.5. The resulting 120-μm-diam fibers were as long as 2.5 m (Fig. 2). For the remainder of this letter, data given are for *c*-axis fibers with a diameter of 110 μm.

The fibers grown are unclad (core index = 1.78) and therefore highly multimode. Despite the large numerical aperture, the measured modal power distribution after propagating a laser beam through a 0.71-m-long fiber has a full angle at half intensity of only 11°. This distribution was only weakly sensitive to bends in the fiber and input launching conditions.

Low propagation loss is necessary for optical applications of sapphire fibers. Two effects, scattering and absorption, contribute to the total loss. Absorption can arise from point defects in the crystal and from impurities. Since there is no contact of the liquid zone with crucibles or dies during the growth process, contamination of the crystal with metallic impurities during growth is not a problem, suggesting that impurities in the source material, gaseous species (H_2O), or color centers are responsible for extrinsic absorption. Inclusions, inhomogeneities, and surface irregularities increase the scattering losses. We could not detect any inhomogeneities in the volume of the fibers with optical microscopy, nor were any scattering centers apparent under laser illumination, which suggests that diameter variations are the most important factor influencing the scattering loss.

Variations in diameter can be caused by several sources. Heating power fluctuations and variations in the diameter of the source rod or the feed rate affect the molten zone volume which in turn affects the diameter of the fiber. A diameter measurement system[5] recorded the variations in the diameter of the fiber during growth. The diameter variations, which typically have a maximum at a spatial period of 5 mm for 110-μm-diam fibers, roll off rapidly for shorter periods. This is fortunate, since short-period variations efficiently couple power to higher order modes and ultimately lead to scatter loss.[6] The rms diameter variation is 2–3% for spatial periods shorter than 15 mm. Even though an active stabilization loop kept the laser power constant to within 0.5%, we believe that the main source for diameter variations are laser power fluctuations, amplified by the resonant response of the molten zone.[7] Further studies of the growth dynamics are in progress.

Scatter losses were measured by launching laser light into the fiber and measuring scattered radiation along the

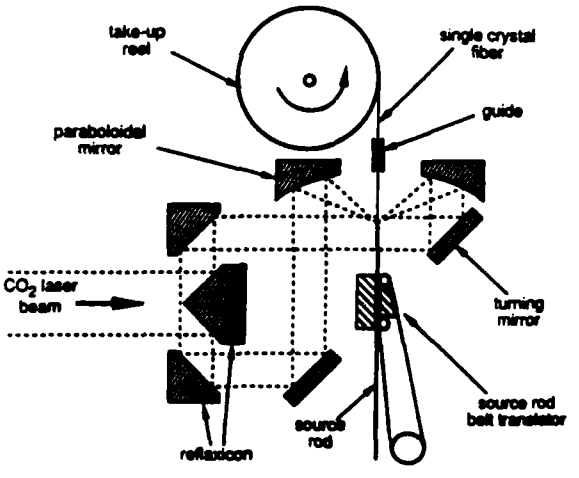

FIG. 1. Cross-sectional diagram of focusing optics and translators used to grow single-crystal fibers.

 0003-6951/89/472170-03$01.00

FIG. 2. Photograph of a 110-μm-diam c-axis single-crystal sapphire fiber. The ruler unit is mm.

fiber with a photodiode in a 6-cm-diam integrating sphere.[8] As the scatter losses are dependent on the modal power distribution,[6] there is no unique loss figure for a given wavelength. Since the angular distribution of the output light was found to be largely insensitive to moderate fiber bending, we expect the loss measurements, taken near the output end of the 0.71-m-long fiber, to be representative of those for actual applications. Results of scatter loss measurements at wavelengths ranging from 458 to 2936 nm are shown in Table I. The scatter losses for all the wavelengths measured are the same, 0.16 dB/m, within experimental accuracy. The change in throughput of a fiber bent in a loop with a radius of 13 mm was found to be less than 1%.

Calorimetry was used to measure absorption losses in fibers.[9] The calorimeter consisted of two identical capillary tubes each 30 cm long, one containing the sample and the other serving as a reference. The absorbed laser light heated the fiber, and the resultant temperature difference between the two capillary tubes was measured with six thermocouple junctions in series. The responsivity of the calorimeter was measured with a heating wire in place of the fiber. The guided power was calculated from the measured output, taking into account the Fresnel reflection loss and attenuation as the light travels from the point of measurement to the end of the fiber.

The results of the absorption measured by calorimetry at six different wavelengths for a fiber grown in air are shown in Table I. A lower absorption loss of 0.88 dB/m for 2936 nm light was measured for a fiber grown in an atmosphere of pure oxygen, probably due to reduced OH incorporation.[10] From the data in Table I, it can be seen that absorption dominates scattering losses in the visible and the mid-infrared. In the near-infrared, absorption is small and comparable in magnitude to the scatter losses.

The absorption in the UV-visible region of the spectrum was measured using an arc lamp. The arc was imaged by a

TABLE I. Scattering and absorption losses for a fiber grown in air. The data point in parentheses is for a fiber grown in an oxygen atmosphere.

Wavelength (nm)	Scattering loss (dB/m)	Wavelength (nm)	Absorption loss (dB/m)
458	0.16 ± 0.03	458	17.4 ± 0.8
488	0.17 ± 0.03	488	6.30 ± 0.1
515	0.16 ± 0.03	515	4.6 ± 0.15
633	0.13 ± 0.03	633	1.3 ± 0.2
1064	0.18 ± 0.035	1064	0.28 ± 0.08
		2936	1.7 ± 0.2 (0.88 ± 0.2)

lens onto the plane of an aperture which let pass light from a small section of the arc that had a well-defined spectral emission. One end of the fiber was positioned in the aperture; the other end was placed inside an integrating sphere. The wavelength dependence of the ouput of the sphere was measured with a 1 m spectrometer and photomultiplier detector. The wavelength dependence of the throughput of the measurement system was removed by normalizing the data to the signal obtained by directly imaging the aperture onto the input of the integrating sphere. The overall scale factor was set by comparison with the 633 nm data point in Table I.

The resulting curve for the attenuation constant α in a c-axis fiber is shown in Fig. 3, along with the absorption losses measured at the laser wavelengths. There is a broad absorption band centered at 400 nm (corresponding to a photon energy of 3.1 eV) with a peak absorption of 18 dB/m (0.04 cm^{-1}). An absorption band centered at 3 eV with a full width at half maximum of 1.5 eV, similar to the observed band, has previously been reported in γ-irradiated sapphire crystals.[11,12] The type of color center responsible for the absorption has been attributed to hole (or V-type) centers. Two hole (V^-), one hole (V^{2-}), and V_{OH}^- centers[13] all absorb near 3.0 eV.[14] Bauer and Whitmore[15] propose a hole trapped on an anion which is adjacent to a substitutional divalent iron impurity. The absorption bands of all of these centers were reported to be bleached when the samples were annealed at a high temperature. We are currently investigating annealing as a means of reducing the 3.0 eV absorption in the sapphire fibers.

The possibility of laser surgery using sapphire fibers was

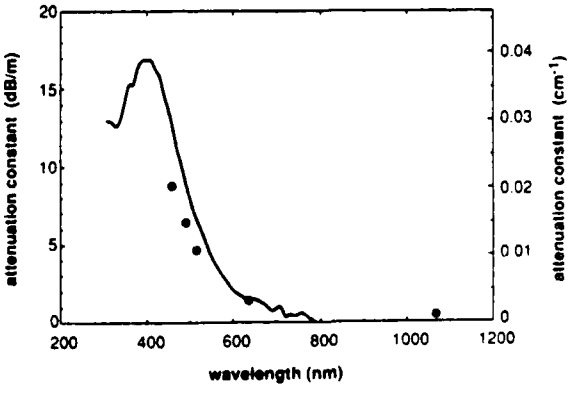

FIG. 3. Loss coefficient in 110-μm-diam fiber. The solid line depicts the attenuation constant measured with the arc lamp apparatus. Circles are absorption losses from Table I measured by laser calorimetry.

investigated with a Quantronix model 294 Er:YAG laser operating at 2936 nm with a pulse duration of 110 μs and a repetition rate of 3 Hz. To establish the damage threshold, the flash lamp energy was slowly increased. The energy incident on the input end of the fiber was estimated by recording the ouput of the fiber and correcting for propagation losses. No damage was observed for 130 mJ pulses falling on the 110-μm-diam input face of the fiber. Assuming uniform intensity across the end face yields a damage threshold in excess of 1.2 kJ/cm^2 (an intensity of 11 MW/cm^2). Ablation of post-mortem human arterial tissue was observed with 6 mJ per pulse at the output of the fiber. Assuming a fiber delivery system 4 m in length with a loss coefficient of 1 dB/m, reflection losses of 8% at each end, and with an output energy of 6 mJ per pulse, the incident fluence on the fiber would be at least seven times below the damage threshold. We conclude that sapphire single-crystal fiber power delivery systems are feasible for medical applications.

Because the Er:YAG laser exhibited spiking and operated in multiple transverse modes, the local damage threshold of the sapphire fiber surface is probably higher than the average value of 11 MW/cm^2. Furthermore, the surface damage threshold of sapphire has been shown to depend strongly on absorbing defects or impurities in the surface layer.[16] We believe that the surface absorption could be reduced by improving the polishing techniques and by annealing the polished surface,[16] leading to a considerable increase in damage threshold. Alternatively, the damage threshold could be increased by tapering the fiber to increase the endface area.

The tensile strength of sapphire fibers is ten times that of fluoride or silver halide fibers and is adequate for practical applications.[17–19] A bend radius of 4 mm has been demonstrated in a 150-μm-diam fiber,[20] and 50-μm-diam fibers are easily handled without breakage. For many delivery system applications, highly flexible fibers are necessary. To compare sapphire fibers with fused silica, we note that the force required to bend a long rod into a certain shape is proportional to Ed^4/l^3, where E is the Young's modulus, d is the diameter, and l is the length of the fiber.[21] Because sapphire fibers have a Young's modulus of 4.95×10^{11} Pa along the c axis,[22] seven times larger than fused silica, seven times as much force is necessary to bend a sapphire fiber as is required to bend a glass fiber of the same dimensions. If the same flexibility is required for a sapphire fiber as for a glass fiber, meaning that Ed^4 is kept constant, the diameter of the crystal fiber should be reduced to 62% that of the glass fiber.

To summarize, high quality single-crystal sapphire fibers of lengths over 2 m were grown and evaluated. Measured scatter losses were less than 0.2 dB/m. The loss was dominated by absorption, with a broad absorption band centered at 400 nm. Laser light at 2936 nm was guided with a total loss of 1 dB/m, and a damage threshold of 1.2 kJ/cm^2 for a 110-μs-long pulse. Ablation of post-mortem arterial tissue was demonstrated with incident fluences at the fiber surface well below the damage threshold. Power handling might be improved by reducing impurities in the fiber and improved end polishing techniques or by tapering the fiber. The sapphire fibers are well suited for medical applications due to their nontoxicity, chemical inertness, and mechanical strength.

The authors wish to thank Greg Magel for helpful discussions. The assistance of Janet Brooks and Michel Digonnet with the Er:YAG measurements is appreciated. This work was funded by the Air Force Office of Scientific Research, contract AFOSR-88-0354 and by the National Science Foundation, contract DMR 87-21735-A1 through the Center for Materials Research at Stanford University.

[1] R. R. Dils, J. Appl. Phys. **54**, 1198 (1982).
[2] L. Esterowitz, C. A. Hoffman, and D. C. Tran, SPIE Proc. **605**, 32 (1986).
[3] M. M. Fejer, J. L. Nightingale, G. A. Magel, and R. L. Byer, Rev. Sci. Instrum. **55**, 1791 (1984).
[4] The source rods were manufactured from HEM-sapphire supplied by Crystal Systems Inc., 27 Congress St., Salem, MA 01970.
[5] M. M. Fejer, G. A. Magel, and R. L. Byer, Appl. Opt. **24**, 2362 (1985).
[6] D. Gloge, Bell Syst. Tech. J. **51**, 1767 (1972).
[7] M. M. Fejer, Ph.D. dissertation, Stanford University, Stanford, CA, 1986, pp. 163–173.
[8] D. H. Jundt, M. M. Fejer, and R. L. Byer, SPIE Proc. **1084**, 39 (1989).
[9] Dietrich Marcuse, *Principles of Optical Fiber Measurements* (Academic, New York, 1981), pp. 205–212.
[10] H. Engstrom, J. B. Bates, J. C. Wang, and M. M. Abraham, Phys. Rev. B **21**, 1520 (1980).
[11] R. A. Hunt and R. H. Schuler, Phys. Rev. **89**, 664 (1953).
[12] P. W. Levy, Phys. Rev. **123**, 1226 (1961).
[13] T. J. Turner and J. H. Crawford, Jr., Solid State Commun. **17**, 167 (1975).
[14] K. H. Lee, G. E. Holmberg, and J. H. Crawford, Jr., Solid State Commun. **20**, 183 (1976).
[15] C. F. Bauer and D. H. Witmore, J. Solid State Chem. **11**, 38 (1974).
[16] Yu. K. Danileiko, A. A. Manekov, and V. S. Nechitailo, *Laser Induced Damage In Optical Materials: 1980*, edited by H. E. Bennett, A. J. Glass, A. H. Guenther, and B. E. Newnam (NBS, Boulder, 1981), p. 369.
[17] H. Liu, K.-S. Lim, W. Jia, E. Strauss, W. M. Yen, A. M. Buoncristiani, and C. E. Byvik, Opt. Lett. **13**, 931 (1988).
[18] J. A. Wysocki, C. G. Pantano, and J. J. Mecholsky, SPIE Proc. **843**, 21 (1987).
[19] A. Sa'ar, N. Barkay, F. Moser, I. Schnitzer, A. Levite, and A. Katzir, SPIE Proc. **843**, 98 (1987).
[20] G. A. Magel, D. H. Jundt, M. M. Fejer, and R. L. Byer, SPIE Proc. **618**, 89 (1986).
[21] S. Timoshenko and J. N. Goodier, *Theory of Elasticity*, 2nd Ed. (McGraw-Hill, New York, 1951), pp. 35–39.
[22] Landolt-Börnstein, *Zahlenwerte und Funktionen aus Naturwissenschaften und Technik, Neue Serie*, edited by K.-H. Hellwege and A. M. Hellwege (Springer, Berlin, 1975), p. 50.

TWO-PHOTON-INDUCED BIREFRINGENCE IN POLYSILANES

F.M. SCHELLENBERG, R.L. BYER
E.L. Ginzton Laboratory, Stanford University, Stanford, CA 94305, USA

and

R.D. MILLER
IBM Almaden Research Center, 650 Harry Road, San Jose, CA 95120, USA

Received 23 October 1989; in final form 13 December 1989

Chain scission induced by two-photon exposure produces a permanent birefringence in polysilane polymer films, which can be used for the formation of birefringent optical elements. Spectroscopy of the effect for poly(di-*n*-hexylsilane) reveals an unexpected sharp resonance at 580 nm. A comparison of several polysilanes indicates the effect only occurs in polymers with symmetric or near symmetric sidegroups. Models to explain these observations are introduced and discussed.

1. Introduction

The nonlinear optical properties of low-dimensional materials have been a subject of great interest in recent years [1]. These include quantum wells and wires [2], fabricated by epitaxial growth of semiconductors, and their natural analogs in the form of perovskites [3] and polymers [4]. These materials can be prepared with third-order nonlinear optical susceptibilities large enough to allow their consideration for applications to harmonic generation [5] or optical switching [6]. The most commonly studied polymer systems for switching applications are highly conjugated carbon based polymers, such as the polydiacetylenes [7]. These polymers show extensive electron delocalization, allowing large transition dipole moments and therefore large nonlinear optical susceptibilities. Unfortunately, polydiacetylene compounds generally absorb strongly at visible wavelengths, making them useful for optical devices only in the near-infrared. Optical quality films have also proven difficult to fabricate, although some progress has been made in this area [8].

In contrast to the polydiacetylenes, thin films of polysilane polymers are more readily formed, and are transparent throughout the visible spectrum. These polymers have a long catenated σ-bonded silicon backbone with two sidegroups, usually carbon based, attached to each Si atom in the backbone chain [9]. They are soluble in most hydrocarbon solvents and thin films of excellent optical quality can be fabricated with conventional spinning and coating techniques. In spite of the σ-bonded nature of the backbone, the polysilanes show extensive electronic delocalization, resulting in strong transitions for excitations polarized parallel to the backbone. The lowest energy transition is believed to be a σ–σ^* excitation [10], with the σ^* excited state even more delocalized than the ground state [11]. The oscillator strength of the σ–σ^* transition in solution has been measured to be $f \approx 0.1$ (per Si–Si bond) [10], and absorption coefficients as large as $(1\text{–}2)\times 10^5$ cm^{-1} in the solid state are typical. The linewidth of this transition (≈ 350 meV) is believed to be inhomogeneously broadened by a distribution of chain segment lengths and is comparable to the linewidth of the lowest energy exciton transition in polydiacetylenes [4]. Unlike conjugated carbon compounds, however, polysilane absorption maxima occur in the near UV, between 300 and 400 nm, and films are completely transparent at visible wavelengths.

Decay of the σ^* state when excited by UV photons

0009-2614/90/$ 03.50

occurs primarily through fluorescence or photochemical reactions. Decay by polymer backbone scission reduces the polymer molecular weight, changing both the solubility and optical properties. Typical scission quantum yields for polysilanes in the solid state are low (about 1%) [9]. The large UV oscillator strengths and photolability, combined with exceptional stability in an oxygen plasma environment, make these materials useful as photoresists [12], which suggests the possibility of optical waveguide fabrication through lithographic patterning. Photoconductivity [13] and high hole mobilities [14] are also observed during direct excitation in the UV.

The large UV oscillator strengths and electronic delocalization also give rise to large optical nonlinear susceptibilities. Recent publications have described measurements of $\chi^{(3)}$ for polysilanes to be on the order of 10^{-11}–10^{-12} esu for third-harmonic generation [15] and four-wave mixing processes [16]. Two-photon absorption, being a $\chi^{(3)}$ phenomenon, should therefore be strong as well for this class of polymers. We have observed this to be the case, with $\chi^{(3)} \approx 3.2\times10^{-10}$ esu at 560 nm, and the primary excitation decay paths of energy transfer, polymer chain scission, and UV fluorescence very similar to those observed with single-photon exposure [17].

However, we observe a remarkable difference between single-photon excitation in the UV and multiphoton excitation at visible wavelengths: a strong, permanent birefringence is induced in thick polymer films by nonlinear photoexposure. Even though similar processes of chain scission (reducing the UV absorption strength at the original maximum) and energy transfer to longer chain segments (resulting in fluorescence depolarization) occur for both linear and nonlinear exposure [17], the relative rate of scission for chain segments excited by energy transfer (e.g. those aligned perpendicular to the exposing laser polarization) for two-photon excitation is observed to be significantly slower than that observed for UV excitation. As the UV absorption of the parallel chain segments decreases anisotropically through nonlinear photoexposure, the corresponding index of refraction at visible wavelengths is reduced anisotropically as well, inducing in the film a birefringence with an orientation determined by the polarization of the exposing laser.

A comparison of net birefringence induced by both single-photon and two-photon exposure is seen in the log–log plot of fig. 1. The slope of birefringence growth is ≈ 1 in both cases, implying a similar photochemical reaction rate. In both cases, Δn reaches a saturation value, implying completed scission of most of the well aligned chain segments, and subsequently decays as chains of other orientations undergo photochemistry. However, the slope of the birefringence decay is quite different for the two exposure paths, indicating different rates of energy transfer or photochemistry for chain segments not aligned with the exposing laser polarization. Furthermore, the net saturation birefringence that can be induced with two-photon exposure can be as large as $\Delta n \approx 0.03$ in films several microns thick, while the net value of Δn induced by UV exposure for films of similar thickness is considerably less.

This high degree of polarization "memory" pro-

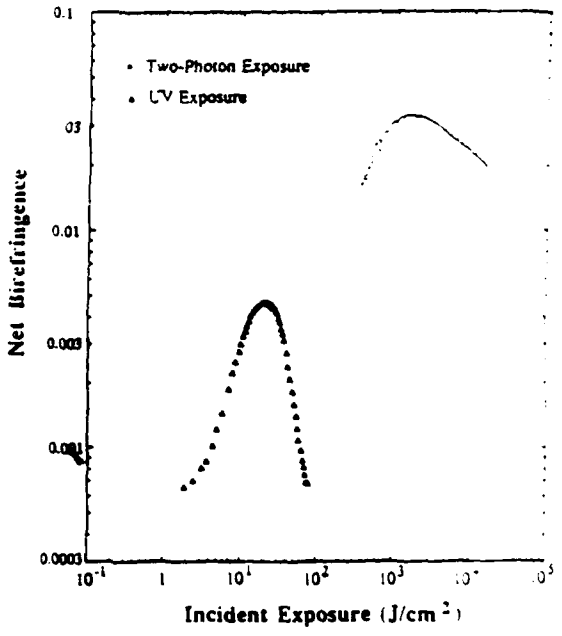

Fig. 1. Birefringence (Δn) versus incident exposure in (J/cm^2) for polarized UV (▲) and polarized pulsed laser (●) exposure. The continuous 325 nm UV power density was 0.2 W/cm^2, while the 575 nm pulsed laser intensity (using 8 ns pulses at 10 Hz) was 1.6 GW/cm^2.

duced by nonlinear photoexposure of isotropic materials is, to our knowledge, unique to the polysilanes, and has the potential for many useful applications. These include the formation of birefringent gratings and variable waveplates through photoexposure [18], as well as the patterning of integrated optical devices.

2. Experimental

An optical ellipsometry measurement was used to characterize the birefringence growth and decay. Films of high molecular weight ($M_w \approx 2.3 \times 10^6$ by gel permeation chromatography) poly(di-*n*-hexylsilane) were prepared from solutions in isooctane (5% by weight). The solutions were passed through a 1 μm filter, and spun onto quartz wafers using spin speeds of 3000 rpm. This procedure produced films that were approximately 1 μm thick, although the exact thickness depended on spinning acceleration and solution viscosity. After spinning, the films were baked at 100°C for 10 min, and cooled to 10°C for at least a day to allow substantial sidechain crystallization. Film thickness was measured with a Tencor alpha-step 2000 stylus profilometer at the minimum force setting.

The experimental configuration is schematically represented in fig. 2. A polarized, pulsed dye laser beam (pulse width ≈8 ns; spot radius ≈275 μm) was focused onto the polymer film to produce power densities (0.2–2.5 GW/cm²) which were large enough to induce significant two-photon absorption.

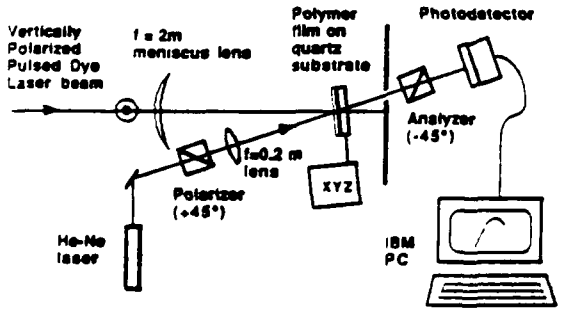

Fig. 2. Schematic diagram of the ellipsometry setup for measuring the growth of birefringence induced by two-photon absorption.

Ten different laser dyes were used to span the wavelength range 545–723 nm. A He–Ne probe at 632.8 nm (spot radius ≈25 μm) with polarization oriented +45° to the dye laser polarization was overlapped with the dye laser at the polymer film. The He–Ne beam subsequently passed through an analyzer oriented at −45° to the exposing laser, and the transmitted power was measured using a calibrated photodetector. Data were acquired from the photodetector with an IBM PC, and the net birefringence calculated using the approximation

$$\Delta n = \frac{\lambda \sqrt{P_{sig}}}{\pi d \sqrt{P_{max}}}, \qquad (1)$$

where d and λ are the total film thickness and wavelength in microns, and P_{max} is the maximum transmitted power with the analyzer oriented at −45°. This relation is correct within 1% as long as $\Delta n \pi d / \lambda < 0.15$.

The growth of the birefringence was monitored at various wavelengths and laser powers. Because exposure induces irreversible birefringence in the polymer, a new location on the film was used for each exposure. Care was taken so that the spot size and power, and hence the intensity, remained constant for all the exposures in each set of measurements. For comparison, an exposure using the same ellipsometry arrangement was made using an unfocused polarized continuous wave He–Cd laser (spot radius ≈388 μm) at 325 nm in place of the dye laser beam.

Typical data from a UV and two-photon exposure are shown in fig. 1. As mentioned above, the birefringence grows from an isotropic background until a saturation value is reached. For two-photon exposures at yellow wavelengths (≈580 nm), Δn is initially proportional to exposure (slope ≈ 1 on a log–log plot), but saturates quickly at ≈0.03 and begins to decay slowly with continued photoexposure. This corresponds to rapid photodegradation for chain segments aligned with the laser polarization, followed by slower degradation for chains of other orientations excited either directly or by energy transfer. Similar behavior is observed with polarized UV exposure, but the net birefringence saturates at a much lower value ($\Delta n \approx 0.005$). This is principally because UV-induced photochemistry occurs only in a small skin depth of a few hundred nanometers, and

not over the entire thickness d of the film, due to strong polymer absorption.

At low values of birefringence, the scission of non-aligned chain segments excited by energy transfer is negligible, and Δn is proportional to the number of aligned polymer backbone segments undergoing scission p_{sc} per unit area in time t. This in turn is related to multi-photon absorption by

$$\Delta n \propto p_{sc} \propto q p_{abs} \propto q[1-e^{-\beta(\lambda)lz}]It \approx q\beta(\lambda)Iz It, \quad (2)$$

where q is the scission quantum yield (generally ≈ 0.01 in the solid state), p_{abs} is the number of photons absorbed per unit area, I is the laser intensity in W cm^{-2}, β is the two-photon absorption coefficient in cm/W, t is the exposure time in s, and z is the film thickness in cm.

The exposure time (t) needed to induce a fixed birefringence (i.e. fixed p_{abs}) for a given $\beta(\lambda)$ is inversely proportional to the square of the exposure intensity for a two-photon process. This is the case for our measurements, as can be seen from the plot of t versus I for a fixed wavelength shown in fig. 3. The data are well fit on a log–log scale by a straight line of slope -2, agreeing well with the proportionality expected from a two-photon process, until saturation occurs for intensities $I > 1.5$ GW/cm^2. Similarly, for fixed p_{abs} and intensity, the exposure dose is inversely proportional to $\beta(\lambda)$, the nonlinear absorption coefficient. Relative values of β calculated from the exposure needed to induce a fixed birefringence can therefore be normalized by comparing the absolute change in UV absorption (also proportional to the number of bonds broken) for both UV and two-photon exposure to infer the number of excitations. This treatment assumes similar scission quantum yields for both two-photon and UV excitation.

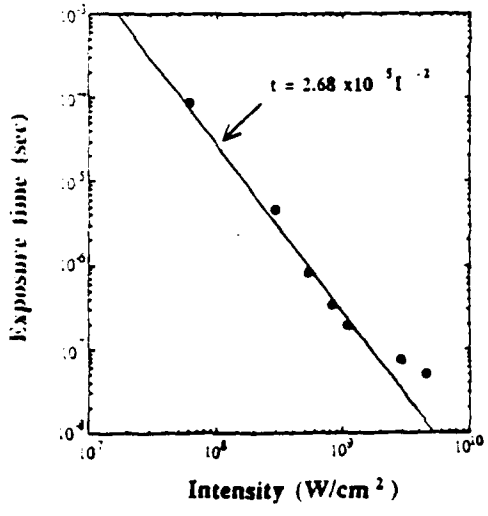

Fig. 3. Log–log plot of exposure time t needed to produce a fixed birefringence of $\Delta n = 0.01$ as a function of intensity. For intensities below 1 GW/cm^2, the solid line of slope -2 fits the data well, confirming the two-photon nature of the transition. At higher intensities, some deviation is observed, indicating saturation of the process.

A spectrum of β for poly(di-*n*-hexylsilane) calculated by the method outlined above is shown on a logarithmic scale as a function of two-photon excitation energy in fig. 4. The squares are data, normalized to the previously measured value of $\chi^{(3)} = 3.2 \times 10^{-10}$ esu (corresponding to $\beta = 0.45$ cm/MW) at 560 nm [17]. The spectrum shows a sharp peak at 579 nm (corresponding to a two-photon energy of 4.3 eV), on top of a broad background centered at 570 nm. The solid line is a least-squares fit of the sum of two Gaussians to the data, with the linewidths of 33 and 410 meV for the sharp and broad features, respectively. The width of the broad band is comparable to that observed for single photon absorption, shown as the dotted line in fig. 4. The sharp spike, however, seems to bear little resemblance to any feature observed in the single-photon absorption case. Although it is not unusual for two-photon absorption spectra to show transitions normally forbidden for linear absorptions, the narrow linewidth of the multi-photon transition inducing the birefringence suggests a more localized or site-selective excitation, without inhomogeneous broadening by the distribution of chain segment lengths.

The induced birefringence is not unique to poly(di-*n*-hexylsilane). Thin films of polysilanes with a variety of substituent groups were prepared and exposed at 573 nm using the ellipsometry arrangement described above. The results are presented in table 1. Detectable birefringence was not induced in compounds with grossly unsymmetrical sidechains, such as poly(methylphenylsilane).

We have also measured fluorescence produced by two-photon excitation for solid films of poly(di-*n*-hexylsilane). For this experiment, the laser was a Spectra Physics sub-picosecond dye laser system, fo-

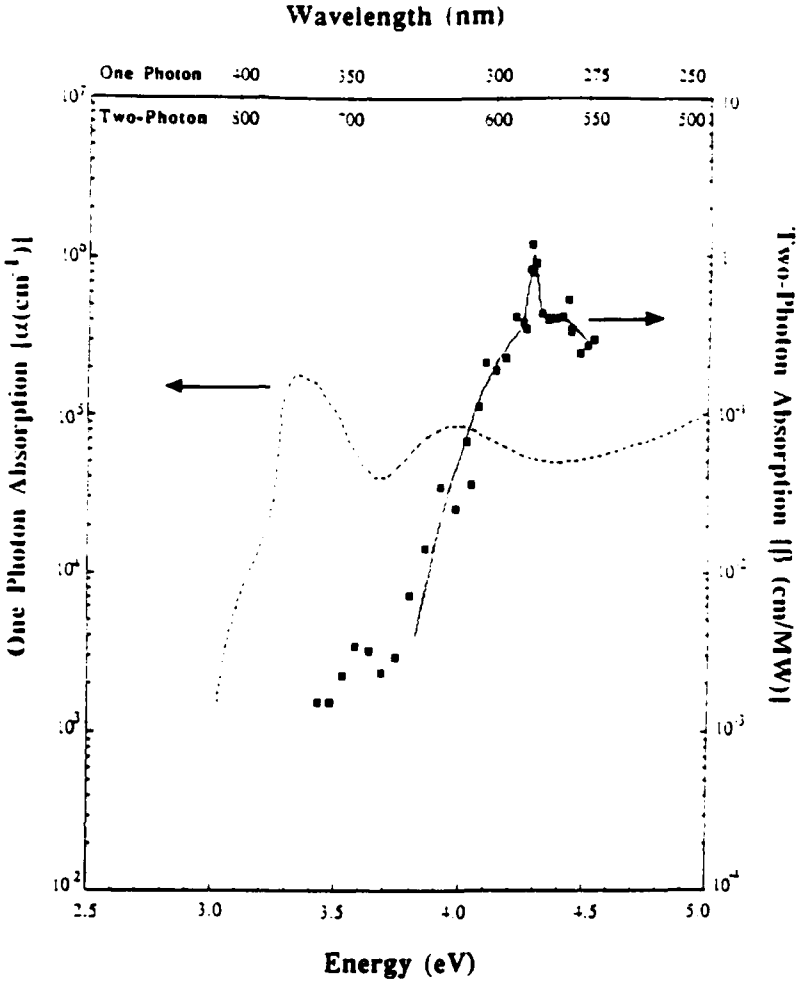

Fig. 4. Spectrum of the two-photon absorption coefficient β in cm/MW for poly(di-*n*-hexylsilane), calculated from birefringence growth curves, as a function of two-photon energy (■), compared with the single-photon absorption spectrum (---). Solid line is a least-squares fit to β using the sum of two Gaussians, one broad ($\approx$412 meV), the other narrow ($\approx$33 meV).

cused onto the polymer films to produce intensities of $\approx$440 MW/cm^2. Emission was collected by an $f=1$ lens, and focused into a 0.5 m spectrometer with an OMA detector. Spectra from the OMA were collected and analyzed using an IBM PC. The two-photon induced emission is broadband ($\Delta\lambda_{fwhm} \approx 10$ nm at room temperature), with line center at $\approx$380 nm. The emission spectrum is identical to that observed with UV excitation, and the average degree of fluorescence anisotropy ($\approx$0.2) produced at the two-photon resonance (579 nm) is quite similar to that observed for on-resonance UV excitations in polysilanes [19, 20].

The spectrum of $\beta(\lambda)$ (plotted on a linear scale in fig. 5a) is complemented by the excitation spectra of the integrated fluorescence (plotted in fig. 5b). At 77 K, the fluorescence excitation spectrum mimics identically the sharp peak and broad background seen in induced birefringence at room temperature, with the respective linewidths of $\approx$25 and $\approx$235 meV. At room temperature, however, only a broad spectrum of width $\approx$295 meV is observed, and the integrated

Table 1
Estimates of β for various polysilanes [a]

Polymer	Backbone structure	λ_{max} (nm)	Effective β (cm/MW)
poly(di-*n*-butylsilane)	7/3 helix	313	0.011
poly(di-*n*-pentylsilane)	7/3 helix	313	0.013
poly(di-*n*-hexylsilane)	planar zigzag	374	0.42
poly(di-*n*-octylsilane)	planar zigzag	374	0.31
poly(di-isohexylsilane)	amorphous	313	0.011
poly(di-tetradecylsilane)	TGTG'	345	0.0011
poly(methylhexylsilane)	amorphous	306	<0.0006
poly(ethylhexylsilane)	amorphous	306	<0.0013
poly(pentylhexylsilane)	amorphous	316	0.018
poly(methylphenylsilane)	amorphous	345	<0.0005
poly(di-*p*-*n*-butylphenylsilane)	planar zigzag	400	0.0012

[a] All measured at 1.6 GW/cm² and $\lambda = 573$ nm. The values of β are calculated from birefringence growth curves, and represent only excitations which lead to chain scission. Different scission yields for the various polymers may lead to different measurements for the overall two-photon absorption.

emission intensity when exciting at 579 nm is reduced by a factor of ≈15 from the spectrum at 77 K. While no decay in fluorescence intensity was observed for exposures at 77 K, fluorescence was observed to decay within seconds for exposures at room temperature. This decrease in fluorescence correlates well with the birefringence growth curves, and is therefore probably caused by a reduction of the population of the fluorescing species through photochemical reactions. The temperature dependence also suggests thermal assistance for the two-photon chain scission process.

These fluorescence measurements are essentially in qualitative agreement with measurements of two-photon induced fluorescence in solid films of poly(di-*n*-hexylsilane) recently published by Thorne et al. [21]. However, the published spectra apparently do not have sufficient resolution to determine if the sharp resonance we observe for relatively thick films occurs in the thin films (100 nm) used in their measurements. Further measurements are needed to resolve this question.

3. Discussion

Although the highest occupied molecular orbital of polysilane polymers has been conclusively determined to involve the delocalized σ-bonded conjugated backbone [9,10], there is some debate in the literature on the nature and energy levels of the excited states. Mintmire [22] and others [23] have extensively modeled these polymers as one-dimensional semiconductors. In this model, the lowest energy σ–σ^* optical absorption at ≈3–4 eV corresponds to the direct band gap of these materials. These band structure calculations also predict the existence of a delocalized π^* band approximately 1 eV above the σ–σ^* transition, coincident with the energy difference we observe in two-photon absorption. Although a direct σ–π^* transition is normally symmetry forbidden, it might be allowed for two-photon absorption and could be a possible explanation for the spectrum we observe. Even though these ab initio calculations underestimate the energy of the lowest transition by about 40% [22], the calculated energy shifts for various regular backbone conformations correlate well with those actually measured for a number of polysilanes of known structure, giving some credibility to the model and the methods used.

Photoconductivity studies of various polysilanes have suggested, however, that the lowest energy absorption is due to the formation of a highly mobile "exciton-like system" [13]. If true, the electronic structure would be similar to that observed in the polydiacetylenes, for which the lowest energy absorption has been unambiguously assigned to exciton formation [24]. Resonant two-photon absorption with a linewidth comparable to the single-photon

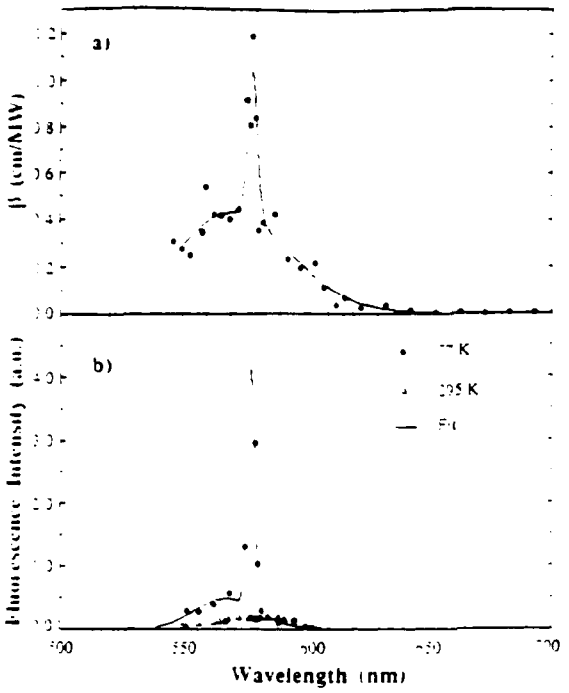

Fig. 5. (a) Plot of β calculated from birefringence growth curves (●) on a linear scale as a function of exposing wavelength. The solid line is the double Gaussian of fig. 4. (b) Linear plot of fluorescence versus exposing wavelength for both 77 K (●) and room temperature (Δ). The solid line is a least-squares fit of the sum of two Gaussians to the low-temperature data, adding one broad feature (≈234 meV) and one narrow (≈25 meV).

exciton linewidth has also been observed for the polydiacetylenes, and has been attributed to the formation of an exciton. In some polydiacetylenes, the two-photon resonance is observed 0.2–0.3 eV below the strong single-photon exciton transition, while one paper [25] reports two-photon absorption 0.5 eV above the single-photon exciton transition. If an exciton model is assumed for the UV transition in polysilanes, it is possible that the two-photon absorption we observe is also due to the formation of an exciton.

As seen in fig. 1, the birefringence growth process is indeed quite similar for both single-photon and two-photon excitation. Furthermore, both excited states decay through similar processes of energy transfer, backbone scission, and UV fluorescence, as would be expected if both excited states were similar exciton-like states. However, the rates of energy transfer, as seen from the rate of birefringence decay in fig. 1, are quite different, indicating some additional mechanism must be considered to fully explain the excitation dynamics of the system. Furthermore, although the linewidth of the broad component of the two-photon absorption (410 meV) is comparable to the linewidth of the UV absorption (350 meV), the presence of the sharp resonance at room temperature in the two-photon spectrum is unlike any observed by single-photon absorption.

The width of the UV absorption features for polysilanes has generally been attributed to an inhomogeneous distribution of chain-segment lengths [10]. In this case, the narrow linewidth of the two-photon absorption feature at 379 nm suggests some kind of highly site specific or localized excitation. This could involve site specific photochemistry, as is found in photochemical hole burning [26], or the creation of some site specific excitonic complex. For example, a bi-exciton, consisting of a bound pair of excitons, can give rise to highly resonant "giant two-photon absorptions" in quantum confined semiconductors [27]. In the polysilanes, a bi-exciton may take the form of two electron–hole pairs on the same chain or nearby chains. The broad spectrum we observe in this case might arise from a distribution of chain-segment mismatches, with two identical long chains being energetically favorable [28], causing the sharp resonance for those specific configurations. For two interacting dipoles on neighboring chains, bi-exciton properties would be highly dependent on the lattice structure and substituent group, as we observe for two-photon absorption. Excitation transfer would also be expected to be weak, as both chains would need to have identical patterns of conformational defects for transfer of both excitations as a bound pair.

At this time, there are insufficient data to conclude which of the above models are the most probable explanation of the unusual two-photon absorption we observe. Each model has elements which agree with our data, but each raises questions that, as yet, are unanswerable. Only more thorough characterization of photoconductivity and spectroscopic properties of a variety of di-alkyl substituted polysilanes will allow the determination of whether the band-to-band model or the exciton model is more

appropriate for the polysilane polymers.

4. Conclusions

In conclusion, we have observed that the chain scission produced by two-photon exposure produces a remarkable permanent birefringence in polysilane films, which is most pronounced for polymers with symmetric or near-symmetric substituent groups. Spectroscopic studies of this effect for poly(di-*n*-hexylsilane) reveal an unexpected, sharp resonance at 579 nm on top of a broad background. Two-photon excitation induces localized scission, causing birefringence, or decays into conventional excitations, which subsequently decay by processes identical to that found in UV excitation. Both band-to-band and exciton models have some features which agree with the spectra we observe, while each leave some questions unanswered. Further detailed spectroscopic studies of the polymers are needed before an unambiguous assignment can be made.

Acknowledgement

We would like to thank Dr. M. Fejer of Stanford University, Dr. J. Mintmire of the Naval Research Laboratory, and Professor E. Hanamura of Tokyo University for helpful discussions. We would also like to thank Professor Hochstrasser of the University of Pennsylvania, Dr. P. Trommsdorff of the CNRS, Université de Grenoble, France, and Dr. G. Kepler of Sandia Labs for sharing unpublished data on recent measurements in polysilanes. In addition, we would like to express special gratitude to Professor Shiraki of the University of Tokyo for providing the laboratory used for the two-photon fluorescence measurements, and Dr. Takahashi and Dr. Kano of the IBM Tokyo Research Laboratory for their assistance in preparing the fluorescence experiment, as well as for helpful discussions. This work was partially supported by the Office of Naval Research, and also supported in part by Air Force Office of Scientific Research contract No. 88-0354.

References

[1] T. Kobayashi, ed., Nonlinear optics of organics and semiconductors (Springer, Berlin, 1989).
[2] D.S. Chemla, D.A.B. Miller and S. Schmitt-Rank, in: Optical nonlinearities and instabilities in semiconductors, ed. H. Haug (Academic Press, New York, 1988).
[3] T. Ishihara and T. Goto, J. Phys. Soc. Japan 57 (1988) 2191.
[4] D. Chemla and J. Zyss, eds., Nonlinear optical properties of organic molecules and crystals (Academic Press, New York, 1987).
[5] M.M. Fejer, S.J.B. Yoo, R.L. Byer, A. Harwit and J.S. Harris Jr., Phys. Rev. Letters 62 (1989) 1041.
[6] H. Haug and L. Banyai, eds., Optical switching in low dimensional systems (Plenum Press, New York, 1989).
[7] D. Bloor and R.R. Chance, eds., Polydiacetylenes (Nijhoff, The Hague, 1985).
[8] T. Kanetake, K. Ishikawa, T. Koda, Y. Tokura and K. Takeda, Appl. Phys. Letters 51 (1987) 1957.
[9] R.D. Miller and J. Michl, Chem. Rev. 89 (1989) 1359.
[10] J. Michl, J.W. Downing, T. Karatsu, K.A. Klingensmith, G.M. Wallraff and R.D. Miller, in: Inorganic and organic polymers, ACS Symp. Ser. Vol. 360, eds. M. Zeldin, K.J. Wynne and H.R. Allcock (Am. Chem. Soc., Washington, 1988) ch. 5.
[11] K.A. Klingensmith, J.W. Downing, R.D. Miller and J. Michl, J. Am. Chem. Soc. 108 (1986) 7438;
[12] R.D. Miller, D. Hofer, G.N. Fickes, C.G. Willson, E. Marinero, P. Trefonas and R. West, Polym. Eng. Sci. 26 (1986) 1129.
[13] R.G. Kepler, J.M. Zeigler, L.A. Harrah and S.R. Kurz, Phys. Rev. *B 35 (1987) 2818.*
[14] M. Stolka, H.J. Yuh, K. McGrane and D.M. Pai, J. Polym. Sci. Polym. Chem. 25 (1987) 823;
L.M. Samuel, P.N. Sanda, R.D. Miller, Chem. Phys. Letters 159 (1989) 227.
[15] F. Kajzar, J. Messier and C. Rosilio, J. Appl. Phys. 60 (1986) 3040;
J.C. Baumert, G.C. Bjorklund, D.H. Jundt, M.C. Jurich, H. Looser, R.D. Miller, J. Rabolt, R. Sooriyakamaran, J.D. Swalen and R.J. Twieg, Appl. Phys. Letters 53 (1988) 1147.
[16] L. Yang, Q.Z. Wang, P.P. Ho, R. Dorsinville, R.R. Alfano, W.K. Zou and N.L. Yang, Appl. Phys. Letters 53 (1988) 1245;
D.J. McGraw, A.E. Siegman, G.M. Wallraff and R.D. Miller, Appl. Phys. Letters 54 (1989) 1713.
[17] F.M. Schellenberg, R.L. Byer, J. Zavislan and R.D. Miller, in: Nonlinear optics of organics and semiconductors, ed. T. Kobayashi (Springer, Berlin, 1989) pp. 192–196;
F.M. Schellenberg, R.L. Byer, R.D. Miller and R. Sooriyakumaran, XVI International Conference on Quantum Electronics Technical Digest (Japan Soc. Appl. Phys., Tokyo, 1988) pp. 702–703.
[18] F.M. Schellenberg, patents pending;
F.M. Schellenberg, R.L. Byer and R.D. Miller, Opt. Letters, in press.

[19] G.E. Johnson and K.M. McGrane, in: Photophysics of polymers, ACS Symp. Ser. Vol. 358, eds. C.E. Hoyle and J.M. Torkelson (Am. Chem. Soc., Washington, 1987) pp. 499 ff.
[20] H.P. Trommsdorff, J.M. Zeigler and R.M. Hochstrasser, Chem. Phys. Letters 154 (1989) 463;
Y.R. Kim, M. Lee, J.R.G. Thorne and R.M. Hochstrasser, Chem. Phys. Letters 145 (1988) 75.
[21] J.R.G. Thorne, Y. Ohsako, J.M. Zeigler and R.M. Hochstrasser, Chem. Phys. Letters 162 (1989) 455.
[22] J.W. Mintmire, Phys. Rev. B 39 (1989) 13350.
[23] K. Takeda and K. Shiraishi, Phys. Rev. B 39 (1989) 11028, and references therein.
[24] F. Kajzar and J. Messier, in: Nonlinear optical properties of organic molecules and crystals, eds. D. Chemla and J. Zyss (Academic Press, New York, 1987) pp. 51–83.
[25] R.R. Chance, M.L. Shand, C. Hogg and R. Silbey, Phys. Rev. B 22 (1980) 3540.
[26] H.P. Trommsdorff, J.M. Zeigler and R.M. Hochstrasser, J. Chem. Phys. 89 (1988) 4440.
[27] M. Ueta, H. Kanzaki, K. Kobayashi, Y. Toyozawa and E. Hanamura, Excitonic processes in solids (Springer, Berlin, 1986) ch. 3.
[28] V. Czikklely, H.D. Forsterling and H. Kuhn, Chem. Phys. Letters 6 (1970) 207.

Fabrication of birefringent gratings using nonlinear polysilane thin films

F. M. Schellenberg and R. L. Byer

Edward L. Ginzton Laboratory, Stanford University, Stanford, California 94305

R. D. Miller

IBM Almaden Research Center, 650 Harry Road, San Jose, California 95120

Received July 21, 1989; accepted December 12, 1989

Birefringence is shown to be induced in polysilane thin films by the process of chain scission induced by nonlinear absorption at visible wavelengths. This writable birefringence is easy to control and can be used for the fabrication of birefringent gratings and other optical devices.

Birefringent optical materials have been used in many devices to control the propagation of light. Such devices generally use materials with natural birefringence, such as quartz or lithium niobate, in their construction. Elements with intricate patterns, such as birefringent gratings, are generally difficult to fabricate. Although such gratings have been the subject of much speculation,[1] and some progress has been made toward their construction with liquid crystals,[2] there is a need for a solid material that is easy to manipulate and has polarization properties that are easily controlled for the fabrication of such devices.

We have discovered that birefringence can be easily controlled in a class of polysilane polymers. We have observed that by exposure of these materials to optical radiation they can retain the memory of the polarization of the light used for exposure, creating a birefringence in thin films of the polymer when exposed to polarized laser light. The birefringence can be as large as $\Delta n \approx 0.03$, which is useful for diffraction gratings and for patterning of integrated-optical devices.

Unlike most polymers, linear polysilane polymers have a long catenated silicon backbone, with two side groups, usually carbon based, attached to each silicon atom in the backbone chain.[3] Polysilanes are generally soluble in most hydrocarbon solvents, such as hexane, making possible the fabrication of thin films of excellent optical quality by conventional spinning or coating techniques. Electronic and structural properties can vary significantly with the side group.[4,5] Common to all polysilanes, however, is a degree of electron delocalization along the σ-bonded backbone. This delocalization results in large oscillator strengths for excitations polarized parallel to the backbone. Absorptions as large as $1\text{–}2 \times 10^5$ cm^{-1} for the long-wavelength transition (centered at 300 to 400 nm, depending on the side group and backbone conformation) are typical. Figure 1 shows a representative absorption spectrum of a thin film of poly(di-*n*-hexylsilane).

Absorption of UV photons causes scission of the polymer backbone, reducing the molecular weight and changing both the solubility and optical properties.[6] The large UV oscillator strengths and photolability, combined with the ease of fabricating thin films, make these materials useful as photoresists.[7] Polarized emission studies suggest that each chain is composed of various chromophoric segments, each with characteristic segment-length-dependent electronic properties, and that these segments interact by rapid energy transfer.[8] Energy transfer from any excitation to the longest (low-energy) chain segments therefore occurs quickly, giving these a higher probability of scission or decay by emission.

The σ conjugation also gives rise to large optical nonlinearities. Recent studies have described measurements of $\chi^{(3)}$ for various polysilanes and found the

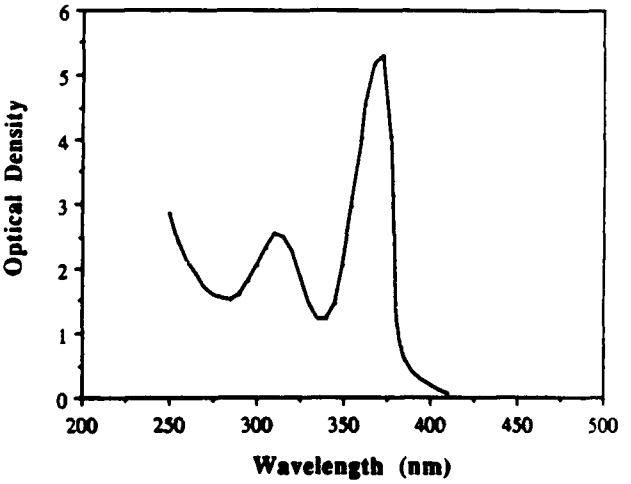

Fig. 1. Linear absorption spectrum of a 700-nm-thick film of poly(di-*n*-hexylsilane). The absorption peak at 374 nm corresponds to the backbone conformation of a crystalline phase, while the weaker peak at 313 nm corresponds to an amorphous phase.

0146-9592/90/040242-03$2.00/0

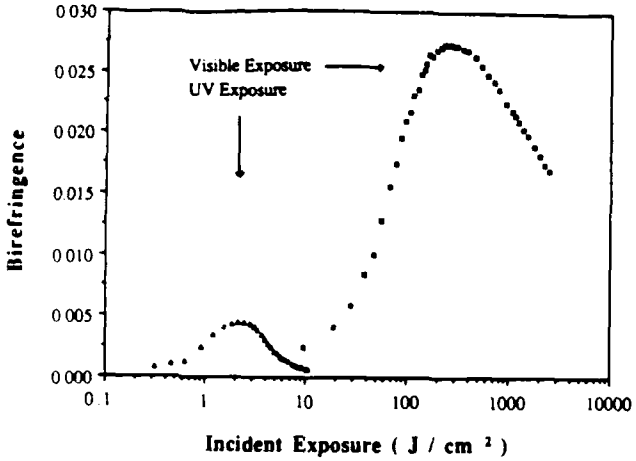

Fig. 2. Birefringence induced in a 700-nm-thick film of poly(di-*n*-hexylsilane) using 8-nsec polarized laser pulses at 570 nm, with a peak power of 150 MW/cm^2 and a 10-Hz repetition rate. Also shown is the weak birefringence induced by polarized UV exposure, with a continuous power density of 50 mW/cm^2.

nonlinearities to be of the order of 10^{-11}–10^{-12} esu for third-harmonic generation[9] and four-wave mixing[10] processes. This suggests that two-photon absorption, being a $\chi^{(3)}$ phenomenon, should be large as well. We have found this to be the case. Using pulsed dye lasers we have observed strong nonlinear absorptions at visible wavelengths, with $\chi^{(3)} \approx 3 \times 10^{-10}$ esu for the process when exposed at 560 nm.[11] The decay paths for the visible excitations appear similar to those seen with UV excitation: the two-photon excitation results in photodegradation and UV fluorescence. The UV emission spectrum in this case is identical to that observed from single-photon excitation.

We have observed, however, one remarkable difference between single-photon and multiphoton excitation: a permanent birefringence is induced in the polymer film by nonlinear photoexposure. This birefringence seems to be caused by preferential scission of chains or chain segments aligned parallel to the exposing laser polarization. As the molecular weight and UV absorption are reduced by photodestruction, the corresponding index of refraction at visible wavelengths is reduced anisotropically as well.

The growth of birefringence in a 700-nm-thick film of the polymer poly(di-*n*-hexylsilane) as a function of exposure to 570-nm pulsed laser light is shown in Fig. 2. This was measured by ellipsometry of the film using a He–Ne laser concurrently with the pulsed dye laser exposure. The birefringence eventually saturates near a maximum value of $\Delta n \approx 0.03$. Subsequent exposure causes the induced birefringence to decrease, as chain segments of other orientations eventually decay as well.

Closer examination shows that birefringence is also induced by exposure to polarized UV light. For the curve marked UV in Fig. 2, birefringence was measured with the same ellipsometry apparatus during exposure to a polarized He–Cd laser light at 325 nm. The growth and decay behavior are different from those observed with nonlinear, pulsed laser exposure: energy transfer to chain segments of other orientations seems to be significantly enhanced. The net birefringence that can be attained is therefore significantly smaller.

The ability to write a controlled birefringent pattern in thin films immediately makes several applications realizable. As an example of one of these applications, we have investigated the possibility of fabricating birefringent gratings. A grating with index modulation of 0.03 in a film a few micrometers thick can have diffraction efficiencies as large as 75%. If this modulation occurs only for one polarization, only that particular polarization will be strongly diffracted. Exposure to an interference pattern at power levels large enough to cause nonlinear chain scission should therefore generate birefringent holograms. To demonstrate this, the experimental arrangement shown in Fig. 3(a) was constructed to write an interference pattern in a thin film of poly(di-*n*-hexylsilane) supported by a quartz substrate. A Quanta-Ray pulsed dye laser, operating with Rhodamine 590 dye, was used to generate a number of polarization gratings under a variety of conditions. The best diffraction was obtained with exposures of the order of 150 MW/cm^2 for 10 sec at 10-Hz repetition rate.

Figure 3(b) is a photograph of a grating produced in this experiment observed between crossed polarizers. The dependence of the diffraction of a polarized He–Ne laser caused by such a grating is shown in Fig. 4. We did not observe ideal diffraction from these gratings, probably owing to the short coherence length of the laser and the absence of ideal vibration-isolation conditions for grating formation. The diffraction observed, however, is fit well by a sinusoidal (solid) curve, which indicates the birefringent nature of the grating: light polarized parallel to the exposing laser polarization is efficiently diffracted, while diffraction for orthogonally polarized light is significantly reduced. The residual light diffracted at the polarization orthogonal to the exposing laser polarization is

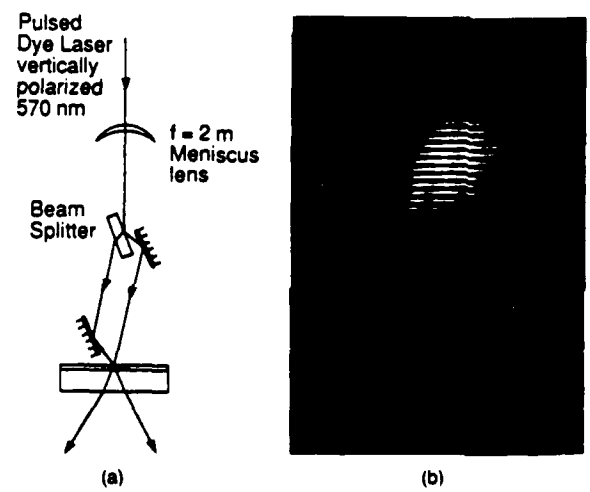

Fig. 3. (a) Holographic arrangement for the fabrication of birefringent gratings and (b) photomicrograph of a region of polysilane exposed in this arrangement. The photograph was taken after exposure, with the sample between crossed polarizers oriented at ±45° to the exposing laser polarization, which was oriented parallel to the interference fringes.

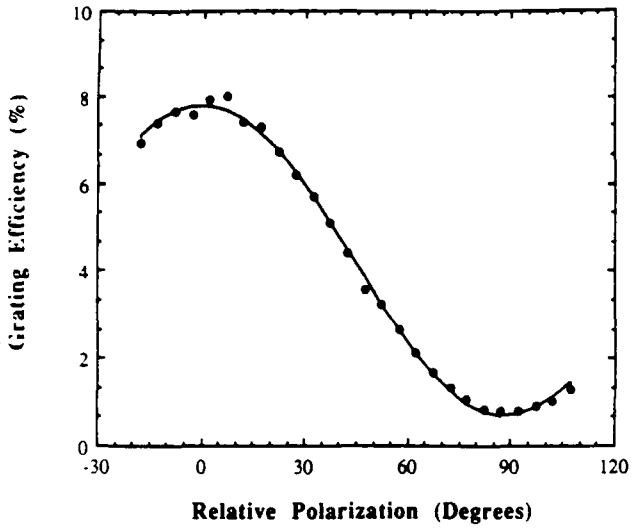

Fig. 4. Diffraction of a polarized He–Ne laser by a birefringent grating. The He–Ne polarization was rotated relative to the polarization of the laser used to write the hologram. The grating efficiency is normalized, with 100% corresponding to the maximum diffraction possible with the film thickness and exposure used in this experiment.

due to a weak surface relief grating that is formed during photoexposure.

This surface relief grating is indicative of volatilization of photoproducts, and we have observed it to some degree in all experiments using poly(di-*n*-hexylsilane). This tends to increase the surface roughness of the exposed areas and would be a severe drawback to use of this compound in the fabrication of optical devices. Fortunately, we have also observed this writable birefringence effect in other somewhat less sensitive polysilanes, such as poly(di-*n*-pentylsilane), with no evidence of surface damage.

In conclusion, we have observed the phenomenon of writable birefringence caused by multiphoton photoexposure in the class of polysilane polymers and have shown that useful optical devices, such as birefringent gratings, can be easily fabricated with the effect. These results can be easily extended to more intricate patterns, such as gradient birefringence for thin-film Babinet–Soleil compensators, or to superimposed gratings to form thin-film polarization separators. These patterns need not be written with expensive pulsed lasers: the necessary exposure levels can be achieved using tightly focused cw lasers, with patterns written under vector scan control. Problems of surface quality and material sensitivity can probably be overcome by drawing on the diversity of compounds found in this class of polymers. The structural variety within this class of polymers, coupled with the ease of material synthesis and film fabrication, suggests that many applications not yet conceived will be found for this research.

This research was supported by U.S. Air Force Office of Scientific Research contract 88-0354. F. M. Schellenberg thanks M. Fejer and E. Gustafson for helpful discussions.

References

1. R. V. Johnson and A. R. Tanguay, Jr., Opt. Eng. **25**, 235 (1986).
2. A. R. Tanguay, Jr., P. Chavel, T. C. Strand, C. S. Wu, and B. H. Soffer, Opt. Lett. **9**, 174 (1984).
3. R. D. Miller and J. Michl, Chem. Rev. **89**, 1359 (1989).
4. R. D. Miller, J. F. Rabolt, R. Sooriyakumaran, W. Fleming, G. N. Fickes, B. L. Farmer, and H. Kuzmany, in *Inorganic and Organometallic Polymers*, M. Zeldin, K. Wynne, and H. R. Allcock, eds., ACS Symp. Ser. 360 (American Chemical Society, Washington, D.C., 1988), Chap. 4.
5. R. D. Miller, B. L. Farmer, W. Fleming, R. Sooriyakumaran, and J. Rabolt, J. Am. Chem. Soc. **109**, 2509 (1987).
6. P. Trefonas, R. West, R. D. Miller, and D. Hofer, J. Polym. Sci. Polym. Lett. Ed. **21**, 823 (1983).
7. R. D. Miller, D. Hofer, G. N. Fickes, C. G. Willson, and E. Marinero, Polym. Eng. Sci. **26**, 1129 (1986).
8. K. A. Klingensmith, J. W. Downing, R. D. Miller, and J. Michl, J. Am. Chem. Soc. **108**, 7438 (1986); J. Michl, J. W. Downing, T. Karatsu, K. A. Klingensmith, G. M. Wallraff, and R. D. Miller, in *Inorganic and Organometallic Polymers*, M. Zeldin, K. Wynne, and H. R. Allcock, eds., ACS Symp. Ser. 360 (American Chemical Society, Washington, D.C., 1988), Chap. 5; Y. R. Kim, M. Lee, J. R. G. Thorne, R. M. Hochstrasser, and J. M. Zeigler, Chem. Phys. Lett. **145**, 75 (1988).
9. F. Kajzar, J. Messier, and C. Rosilio, J. Appl. Phys. **60**, 3040 (1986); J. C. Baumert, G. C. Bjorklund, D. H. Jundt, M. C. Jurich, H. Looser, R. D. Miller, J. Rabolt, R. Sooriyakumaran, J. D. Swalen, and R. J. Twieg, Appl. Phys. Lett. **53**, 1147 (1988).
10. L. Yang, Q. Z. Wang, P. P. Ho, R. Dorsinville, R. R. Alfano, W. K. Zou, and N. L. Yang, Appl. Phys. Lett. **53**, 1245 (1988); D. J. McGraw, A. E. Siegman, G. M. Wallraff, and R. D. Miller, Appl. Phys. Lett. **54**, 1713 (1989).
11. F. M. Schellenberg, R. L. Byer, R. D. Miller, and R. Sooriyakumaran, in *Digest of XVI International Quantum Electronics Conference* (Japan Society of Applied Physics, Tokyo, Japan, 1988), p. 702; F. M. Schellenberg, R. L. Byer, J. Zavislan, and R. D. Miller, in *Nonlinear Optics of Organics and Semiconductors*, T. Kobayashi, ed. (Springer-Verlag, New York, 1989), pp. 192–196.

Optical Properties of Lithium-Rich Lithium Niobate Fabricated by Vapor Transport Equilibration

Dieter H. Jundt
Martin M. Fejer
Robert L. Byer

Reprinted from
IEEE JOURNAL OF QUANTUM ELECTRONICS
Vol. 26, No. 1, January 1990

Optical Properties of Lithium-Rich Lithium Niobate Fabricated by Vapor Transport Equilibration

DIETER H. JUNDT, MARTIN M. FEJER, AND ROBERT L. BYER, FELLOW, IEEE

Abstract—**Lithium-rich lithium niobate of excellent optical homogeneity can be fabricated by a vapor transport equilibration (VTE) technique. The high optical quality, uniformly birefringent crystals noncritically phase match for second harmonic generation of 1064 nm Nd:YAG radiation to 532 nm at 238°C. The refractive indexes and their temperature dependence have been measured to derive temperature-dependent Sellmeier equations which predict noncritical phase matching for wavelengths as short as 976 nm to generate blue at 488 nm at room temperature. The Sellmeier equations accurately predict experimental phase-matching temperatures over a wide temperature range.**

LITHIUM niobate exists over a solid-solution range of 44–50 mole percent Li_2O. However, only crystals grown from melts of the congruent composition have good optical quality and uniform birefringence [1], [2]. Unfortunately, crystals of this composition suffer from photorefractive damage when used in nonlinear optical applications involving visible radiation, e.g., second-harmonic generation (SHG) of the 1064 nm output of a Nd:YAG laser [3]. While lithium-rich compositions have greater birefringence and hence higher phase-matching temperatures, they cannot be grown from the melt without birefringence variations that preclude application of such crystals to optical devices. Crystals grown from melts doped with several percent MgO have been used in such applications, as they are less susceptible to the photorefractive effect [4]. However, the useful length of MgO doped crystals is limited by birefringence variations caused by variations in the MgO concentrations [5]. Thus, there is a need for crystals that are optically homogeneous and that phase match above the annealing temperature for the photorefractive effect.

It has recently been shown that lithium niobate of compositions close to stoichiometric with excellent optical quality can be produced by a vapor phase transport equilibration (VTE) technique [6], [7]. The full-width at half-maximum intensity for SHG of 1064 nm in a 20 mm sample was shown to be 0.4 K, comparable to the width expected for a perfectly homogeneous crystal [7]. Phase matching for this interaction was observed at a temperature of 238°C, well above the 110°C annealing temperature [8] for the photorefractive effect. A conversion efficiency of 42 percent for SHG of 1064 nm was achieved *in an 8 mm long sample using a Q-switched laser* with pulse energies around 1 mJ [9].

In order to assess potential device applications of this material, it is necessary to obtain Sellmeier equations with temperature dependent parameters adequate for the prediction of phase-matching temperatures. In this paper we present the two sets of parameters required to completely characterize the temperature dependence of the indexes n_o and n_e. The Sellmeier equation used is of the form

$$n^2 = A_1 + \frac{A_2 + B_1 F}{\lambda^2 - (A_3 + B_2 F)^2} + B_3 F - A_4 \lambda^2. \quad (1)$$

The parameters A_1 through A_4 and B_1 through B_3 are constants depending on the material, λ is the vacuum wavelength in nm, n stands for either n_o or n_e, and the temperature dependence enters through the parameter F where $F = (T - T_0)(T + T_0 + 546)$. T_0 is a reference temperature, in our case 24.5°C. All temperatures are measured in degrees centigrade. Sellmeier equations of this form have been given previously for lithium niobate crystals grown from stoichiometric melts (solid composition approximately 48.7 mole percent Li_2O [10]) and congruently grown crystals (approximately 48.4 percent Li_2O [10]) [11]–[13]. Note that literature values for the Li_2O content of these compositions vary by several tenths of a percent [1], [10]. Values given in this paper, taken from [10], are representative of current results.

The samples used in the present work were fabricated by heating to 1100°C in a closed crucible partially filled with a powdered mixture of $LiNbO_3$ and Li_3NbO_4. There is a net transfer of lithium from the powder into the crystal through a series path of vapor transport and solid-state diffusion that continues until the crystal composition reaches that of the phase boundary, approximately 49.9 mole percent Li_2O [10]. Material processed to this lithium-rich phase boundary is highly birefringent, exhibiting a phase-matching temperature of 238°C for second-harmonic generation (SHG) of 1064 nm radiation, compared to −8°C for the congruent composition [7], [2].

Index of refraction measurements were obtained by the minimum deviation prism technique, using a lithium-rich crystal fabricated into a prism of apex angle 36.6° with 1 × 10 mm optical faces. The optic axis was aligned with

Manuscript received May 22, 1989; revised July 18, 1989. This work was supported in part by the U.S. Army Research Office under Contract DAAL 03-88K-0113, by the Joint Services Electronics Program under Contract N00014-84-K-0327, and by the Air Force Office of Scientific Research under Contract AFOSR-88-0354.

The authors are with the Applied Physics Department, Stanford University, Stanford, CA 94305

IEEE Log Number 8931626.

the axis of the prism to better than 0.5°. The uncertainties in the index of refraction measurements are dominated by the errors in aligning the axis of the thin prism to the rotation axis of the goniometer. Table I shows the measured ordinary and extraordinary indexes of refraction for lithium-rich lithium niobate at room temperature.

The temperature dependence of the indexes was measured using the same prism by recording the change in the deflection angle for temperatures up to 300°C. Fig. 1 shows the measured changes in refractive index for two wavelengths, 325 and 1064 nm, together with a parabolic least square fit of the form

$$n(25°\mathrm{C} + \Delta T) - n(25°\mathrm{C}) = X\Delta T + 0.5Y(\Delta T)^2 \quad (2)$$

where n is the refractive index, ΔT is the temperature above 25°C, and X and Y are the resulting parameters of the fit. Taking the derivative of (2) with respect to the temperature, the temperature derivative of the index of refraction is

$$\frac{dn}{dT}(25°\mathrm{C} + \Delta T) = X + Y\Delta T. \quad (3)$$

The parameters X and Y for the four wavelengths for which the temperature dependence was measured are shown in Table II.

A nonlinear least-squares routine (Levenberg-Marquardt method [14]) was used that simultaneously optimized the 14 parameters for the Sellmeier equations for n_o and n_e. The input consisted of the refractive index data from Table I, and dn/dT values evaluated at 50, 150, and 250°C using the coefficients from Table II. To improve the accuracy of the infrared indexes and the birefringence, two additional data points were included in the fit: the phase-matching angle for SHG of 1064 nm radiation at 22°C, 22.55°, and the signal wavelength, 575.5 nm, for parametric fluorescence with a 476.5 nm pump at 444°C. Table III shows the parameters for the temperature dependent Sellmeier equations for n_o and n_e for lithium-rich lithium niobate.

To test the validity of the predictions based on the parameters given in Table III, several phase-matching temperatures were experimentally determined. In addition, the temperature dependence of the signal wavelength for optical parametric fluorescence was determined for pump wavelengths 514.5, 488.0, and 476.5 nm [15]. The agreement of the prediction with the experimental data for the parametric fluorescence, shown in Fig. 2, is better than 6 K for all points and 3.6 K on average. The temperatures measured for SHG with the pump-wavelengths 954, 1064, and 1318 nm were −62.5, 238, and 520°C, respectively, as shown in Fig. 3. While the SHG for 1064 nm is in very good agreement, the predicted phase-matching temperatures for 954 and 1318 nm are off by −23 and −11 K, respectively, suggesting that the form assumed for the temperature dependence of the indexes is inadequate for temperatures much below 0°C or higher than 400°C. The experimental data presented here for SHG with a pump wavelength of 1064 nm agrees well with previously pub-

TABLE I
MEASURED INDEXES OF REFRACTION FOR VAPOR TRANSPORT EQUILIBRATED LITHIUM NIOBATE AT ROOM TEMPERATURE

Wavelength (nm)	n_e	n_o
1064	2.1440 ± 0.0005	2.2339 ± 0.0005
632.8	2.1890 ± 0.0004	2.2878 ± 0.0005
514.5	2.2270 ± 0.0004	2.3334 ± 0.0004
501.7	2.2329 ± 0.0004	2.3405 ± 0.0004
496.5	2.2352 ± 0.0005	2.3437 ± 0.0004
488.0	2.2398 ± 0.0004	2.3495 ± 0.0004
476.5	2.2465 ± 0.0004	2.3573 ± 0.0005
472.7	2.2489 ± 0.0005	2.3604 ± 0.0005
465.8	2.2530 ± 0.0004	2.3658 ± 0.0004
457.9	2.2584 ± 0.0004	2.3719 ± 0.0004
454.5	2.2608 ± 0.0004	2.3751 ± 0.0005
325.0	2.467 ± 0.0005	2.636 ± 0.002

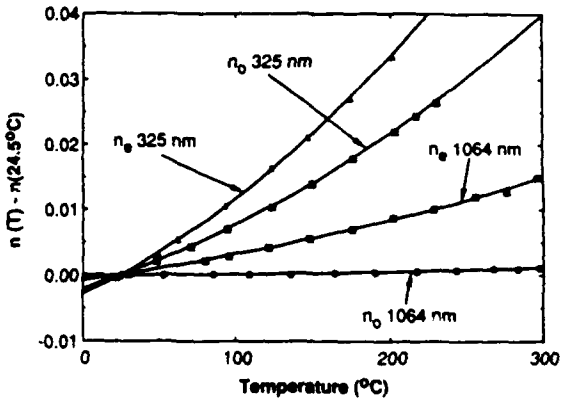

Fig. 1. *Change of refractive index with temperature for two wavelengths. The reference temperature is 25°C. The solid line represents the result from a parabolic approximation.*

TABLE II
PARAMETERS FOR THE REFRACTIVE INDEX CHANGE WITH TEMPERATURE OBTAINED BY TAKING THE DERIVATIVE OF THE PARABOLIC APPROXIMATION OF FIG. 1

Wavelength (nm)	X n_e (10^{-6} K^{-1})	Y n_e (10^{-8} K^{-2})	X n_o (10^{-6} K^{-1})	Y n_o (10^{-8} K^{-2})
1064	38.5	11.5	1.41	2.14
632.8	43.1	20.2	5.22	4.74
454.5	62.2	22.2	19.3	6.64
325.0	129	71.3	87.1	41.9
$\frac{dn}{dT}(25°\mathrm{C} + \Delta T) = X + Y\Delta T$				

TABLE III
PARAMETERS FOR THE TEMPERATURE-DEPENDENT SELLMEIER EQUATION

Parameter	n_e	n_o
A_1	4.546 ± 0.007	4.913 ± 0.006
A_2	(9.17 ± 0.16) × 10^4	(1.163 ± 0.013) × 10^5
A_3	(2.148 ± 0.025) × 10^2	(2.201 ± 0.015) × 10^2
A_4	(3.03 ± 0.59) × 10^{-8}	(2.73 ± 0.44) × 10^{-8}
B_1	(1.93 ± 0.55) × 10^{-2}	(9.4 ± 2.9) × 10^{-3}
B_2	(5.3 ± 0.77) × 10^{-5}	(3.98 ± 0.30) × 10^{-5}
B_3	(2.72 ± 0.15) × 10^{-7}	(1.6 ± 0.72) × 10^{-8}
$n^2 = A_1 + \frac{A_2 + B_1 F}{\lambda^2 - (A_3 + B_2 F)^2} + B_3 F - A_4 \lambda^2$		λ given in nm F = (T-24.5) (T+570.5) T given in °C

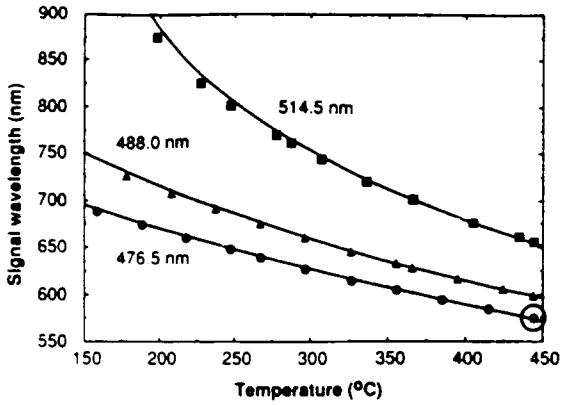

Fig. 2 Signal wavelength of optical parametric fluorescence for three different pump wavelengths. The solid lines are calculated using the Sellmeier parameters of Table III. The encircled data point at 444°C was used to improve the accuracy of the parameters, as described in the text.

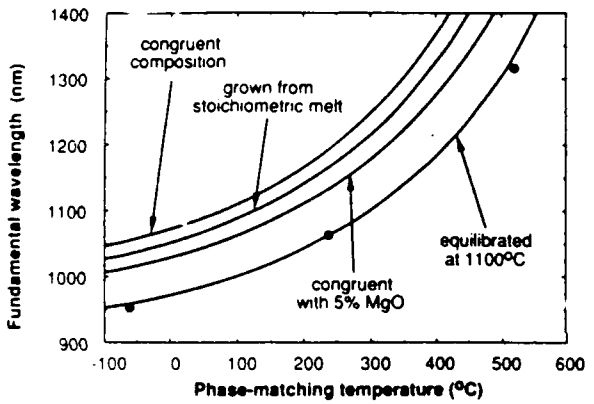

Fig. 3 Comparison of predicted phase-matching conditions for different crystal compositions. Circles depict experimental data points for equilibrated $LiNbO_3$.

lished data [7]. However, the phase-matching temperature we observed for SHG of 954 nm was 25.5 K lower than reported in [7]. The reason for the discrepancy is not clear, but may be due to the use of material from different boules, or differences in processing conditions.

Fig. 3 compares the range of wavelengths that phase-match noncritically for SHG for different types of lithium niobate crystals. The curves for the crystals grown from stoichiometric and congruent melts were calculated using the parameters from [11] and [13]. For the material doped with 5 percent magnesium oxide, we used the parameters from [16]. The graph clearly shows that much shorter wavelengths can be phase matched with the vapor transport equilibrated material than with the other compositions. For example, SHG of 976 nm to generate blue radiation at 488 nm phase matches at room temperature for lithium-rich lithium niobate.

The lithium-rich phase boundary at high temperatures is not vertical, but moves toward lower Li_2O concentrations with increasing temperature [10]. For device fabrication, it is important to know the change in phase-matching temperature for small variations in the processing temperature. It is shown in [10], that for temperatures between 1060 and 1150°C, the molar percentage of Li_2O depends linearly on the processing temperature, with a slope of -1.7×10^{-3} mole percent/K. A change in the processing temperature thus leads to a slightly different Li_2O concentration which shifts the phase-matching temperatures for nonlinear interactions. To estimate the sensitivity of the phase-matching temperature to processing conditions, we assume that the coefficients of the Sellmeier equation may be linearly interpolated between those for congruent material [12] and those from Table III for the lithium-rich material. Fig. 4 shows the sensitivity of the temperature for noncritical phase matching to a change in processing temperature, calculated under this assumption. For example, an increase in processing temperature by 10 K leads to a decrease of the phase-matching temperature for SHG of 1064 nm by 2.3 K.

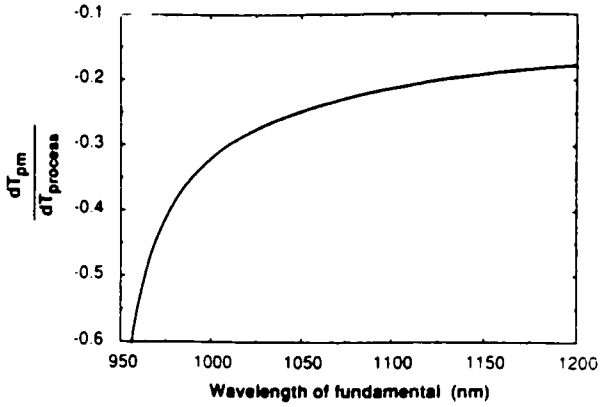

Fig. 4 Sensitivity of the phase-matching temperature T_{pm} to changes in the vapor transport equilibration temperature $T_{process}$.

To summarize, we measured the temperature dependence of the refractive indexes of vapor transport equilibrated lithium-rich lithium niobate and calculated the coefficients for temperature-dependent Sellmeier equations for the ordinary and extraordinary indexes of refraction. The phase-matching temperatures for a wide range of interactions can be predicted to within a few kelvins in the temperature range 0 to 400°C. The equilibrated samples have excellent optical homogeneity and allow for noncritical phase matching for wavelengths as short as 488 nm at room temperature. Interpolation between the Sellmeier coefficients for lithium-rich and congruent lithium niobate allows estimation of the phase-matching temperatures for other compositions of lithium niobate that can be produced by the VTE technique. We are currently studying phase-matching temperatures of samples with different Li_2O concentrations in order to produce crystals useful for other interactions, and to develop composition dependent Sellmeier parameters.

ACKNOWLEDGMENT

The authors would like to thank Y.-S. Luh for help with the vapor equilibration technique, P. Bordui for helpful discussions, and U. Keller for providing a source at 1318 nm.

REFERENCES

[1] J. R. Carruthers, G. E. Peterson, M. Grasso, and P. M. Bridenbaugh, "Nonstoichiometry and crystal growth of lithium niobate," *J. Appl. Phys.*, vol. 42, pp. 1846-1851, 1971.

[2] R. L. Byer, J. F. Young, and R. S. Feigelson, "Growth of high-quality $LiNbO_3$ crystals from the congruent melt," *J. Appl. Phys.*, vol. 41, pp. 2320-2325, 1970.

[3] A. Ashkin, G. D. Boyd, J. M. Dziedzic, R. G. Smith, A. A. Ballman, J. J. Levinstein, and K. Nassau, "Optically-induced refractive index inhomogeneities in $LiNbO_3$ and $LiTaO_3$," *Appl. Phys. Lett.*, vol. 9, pp. 72-74, 1966.

[4] D. A. Bryan, R. Gerson, and H. E. Tomaschke, "Increased optical damage resistance in lithium niobate," *Appl. Phys. Lett.*, vol. 44, pp. 847-849, 1984.

[5] J. L. Nightingale, W. J. Silva, G. E. Reade, A. Rybicki, W. J. Kozlovsky, and R. L. Byer, "Fifty percent conversion efficiency second harmonic generation in magnesium oxide doped lithium niobate," *Proc. SPIE*, vol. 681, pp. 20-24, 1986.

[6] R. L. Holman, "Novel uses of gravimetry on the processing of crystalline ceramics," in *Processing of Crystalline Ceramics (Mat. Sci. Res.*, vol. 11) H. Palmour and R. F. Davis, Eds. New York: Plenum, 1978, p. 343.

[7] Y. S. Luh, M. M. Fejer, R. L. Byer, and R. S. Feigelson, "Stoichiometric $LiNbO_3$ single-crystal fibers for nonlinear optical applications," *J. Cryst. Growth*, vol. 85, pp. 264-269, 1987.

[8] R. L. Byer, Y. K. Park, R. S. Feigelson, and W. L. Kway, "Efficient second-harmonic generation of Nd:YAG laser radiation using warm phase-matching $LiNbO_3$," *Appl. Phys. Lett.*, vol. 39, pp. 17-19, 1981.

[9] Y. S. Luh, private communication.

[10] H. M. O'Bryan, P. K. Gallagher, and C. D. Brandle, "Congruent composition and Li-rich phase boundary of $LiNbO_3$," *J. Amer. Ceram. Soc.*, vol. 68, pp. 493-496, 1985.

[11] M. V. Hobden and J. Warner, "The temperature dependence of the refractive indices of pure lithium niobate," *Phys. Lett.*, vol. 22, pp. 243-244, 1966.

[12] D. S. Smith, H. D. Riccius, and R. P. Edwin, "Refractive indices of lithium niobate," *Opt. Commun.*, vol. 17, pp. 332-335, 1976.

[13] G. J. Edwards and M. Lawrence, "A temperature-dependent dispersion equation for congruently grown lithium niobate," *Optic. Quantum Electron.*, vol. 16, pp. 373-375, 1984.

[14] W. H. Press, B. P. Flannery, S. A. Teukolsky, and W. T. Vetterling, *Numerical Recipes in C*. Cambridge, England: Cambridge Univ., 1988, pp. 542-547.

[15] Y. R. Shen, *Nonlinear Optics*. New York: Wiley, 1984, pp. 134-138.

[16] W. J. Kozlovsky, C. D. Nabors, R. C. Eckardt, and R. L. Byer, "Monolithic MgO:$LiNbO_3$ doubly resonant optical parametric oscillator pumped by a frequency-doubled diode-laser-pumped Nd:YAG laser," *Opt. Lett.*, vol. 14, pp. 66-68, 1989.

Dieter H. Jundt, photograph and biography not available at the time of publication.

Martin M. Fejer, photograph and biography not available at the time of publication.

Robert L. Byer (M'75-SM'83-F'87), for a photograph and biography, see this issue, p. 157.